Chaotic Modeling and Simulation (CMSIM) 2: 247–255, 2013

Dichotomy and boundary value problems on the whole line

Alexander A. Boichuk[1] and Oleksander A. Pokutnyi[2]

[1] Institute of mathematics of NAS of Ukraine, , 01601 Kiev, Ukraine
(E-mail: boichuk@imath.kiev.ua)
[2] Institute of mathematics of NAS of Ukraine, , 01601 Kiev, Ukraine
(E-mail: lenasas@gmail.com)

Abstract. Necessary and sufficient conditions for normal solvability are obtained for linear differential equations in Banach space. Constructed examples demonstrate that even in the linear case (but certainly not correct) you can select a family of bounded solutions, which tend to an equilibrium positions, so-called homoclinic and heteroclinic trajectories.

Keywords: exponential dichotomy, normally-resolvable operator, pseudoinverse operator.

A lot of papers are devoted to development of constructive methods for the analysis of different classes of boundary value problems. They traditionally occupy one of the central places in the qualitative theory of differential equations. This is due to practical significance of the theory of boundary-value problems for various applications - theory of nonlinear oscillations, theory of stability of motion, control theory and numerous problems in radioengineering, mechanics, biology etc.

Correct and incorrect boundary value problems are studied. Ususally correctness is understood as uniqueness of the solution for arbitrary right-hand side of the equation. Correct boundary value problems for ordinary differential equations, impulsive systems, Noether operator equations became popular relatively recently, they were studied in detail [5]. Analysis of a large class of incorrect boundary value problems was associated with the properties of the generalized inverse operator (which exists for any linear operator in a finite dimensional space).

Efforts aimed to solving problem of the existence of bounded solutions of linear differential equations are mainly devoted to the correct case. Additional boundary conditions can be full filled only in a trivial situations for such problems. After Palmer's work [2] it became clear that in the general case, even a finite set of differential equations can not have one bounded solution, and it

Received: 5 April 2012 / Accepted: 12 October 2012

ISSN 2241-0503

makes sense to study the boundary value problem in the incorrect case. Using the pseudoinverse operators approach one can obtain the conditions under which a family of bounded solutions satisfying the supplementary boundary conditions can be identified.

1 Statement of the Problem

In a Banach space $\mathbf{X}$ we consider a boundary value problem

$$\frac{dx}{dt} = A(t)x(t) + f(t) \ , \tag{1}$$

$$lx(\cdot) = \alpha \ , \tag{2}$$

where the vector - function $f(t)$ acts from R into the Banach space $\mathbf{X}$,

$$f(t) \in BC(R, \mathbf{X}) := \{f(\cdot) : R \to \mathbf{X}, f(\cdot) \in C(R, \mathbf{X}), |||f||| = \sup_{t \in R} \|f(t)\| < \infty\},$$

$BC(R, \mathbf{X})$ is the Banach space of functions continuous and bounded on R; the operator-valued function $A(t)$ is strongly continuous with the norm $|||A||| = \sup_{t\in R} ||A(t)|| < +\infty$; $BC^1(R, \mathbf{X}) := \{x(\cdot) : R \to \mathbf{X},\ x(\cdot) \in C^1(R, \mathbf{X}), |||x||| = \sup\limits_{t\in R}\{\|x(t)\|, \|x^1(t)\|\} < \infty\}$, - the space of functions continuously differentiable on R and bounded together with their derivatives; l - linear and bounded operator acts from the space of $BC^1(R, \mathbf{X})$ into the Banach space $\mathbf{Y}$. We determine the conditions of the existence of solutions $x(\cdot) \in BC^1(R, \mathbf{B})$ of boundary value problem (1), (2) under the assumption that the corresponding homogeneous equation

$$\frac{dx}{dt} = A(t)x(t) \tag{3}$$

admits an exponential dichotomy [1–3] on the semi-axes R_+ and R_- with projectors P and Q, respectively, i.e., there exist projectors $P(P^2 = P)$ and $Q(Q^2 = Q)$ and constants $k_{1,2} \geq 1$ and $\alpha_{1,2} > 0$ such that the estimates

$$\begin{cases} \left\|U(t)PU^{-1}(s)\right\| \leq k_1 e^{-\alpha_1(t-s)}, \quad t \geq s, \\ \left\|U(t)(E-P)U^{-1}(s)\right\| \leq k_1 e^{\alpha_1(t-s)}, \quad s \geq t, \quad \text{for all} \quad t, s \in R_+, \end{cases}$$

and

$$\begin{cases} \left\|U(t)QU^{-1}(s)\right\| \leq k_2 e^{-\alpha_2(t-s)}, \quad t \geq s, \\ \left\|U(t)(E-Q)U^{-1}(s)\right\| \leq k_2 e^{\alpha_2(t-s)}, \quad s \geq t, \quad \text{for all} \ \ t, s \in R_- \end{cases}$$

hold, where $U(t) = U(t, 0)$ is the evolution operator of Eq. (3) such that

$$\frac{dU(t)}{dt} = A(t)U(t), \quad U(0) = E \text{ is the identity operator [1, p.145]} \ .$$

2 Preliminaries

Now we formulate the following result, which is proved in [4] for the nonhomogeneous equation (1).

Theorem 1. *Suppose that the homogeneous equation (3) admits an exponential dichotomy on the semi-axes R_+ and R_- with projectors P and Q, respectively. If the operator*

$$D = P - (E - Q) : \mathbf{X} \to \mathbf{X} \tag{4}$$

acting from the Banach space $\mathbf{X}$ onto itself is invertible in the generalized sense [5, p.26], then

(i) in order that solutions of Eq. (1) bounded on the entire real axis exist, it is necessary and sufficient that the function $f(t) \in BC(R, \mathbf{X})$ satisfies the condition

$$\int\limits_{-\infty}^{+\infty} H(t)\, f(t)\, dt = 0; \tag{5}$$

where

$$H(t) = \mathcal{P}_{N(D^*)} Q U^{-1}(t) = \mathcal{P}_{N(D^*)} (E - P) U^{-1}(t),$$

(ii) under condition (5), solutions bounded on the entire axis of Eq. (1) have the form

$$x(t, c) = U(t) P \mathcal{P}_{N(D)} c + (G[f])(t), \qquad \forall \;\; c \in \mathbf{X}, \tag{6}$$

where

$$(G[f])(t) = U(t) \begin{cases} \int\limits_0^t PU^{-1}(s) f(s)\, ds - \int\limits_t^\infty (E-P) U^{-1}(s) f(s)\, ds + \\ +PD^- \left[\int\limits_0^\infty (E-P)U^{-1}(s) f(s)\, ds + \int\limits_{-\infty}^0 QU^{-1}(s) f(s) ds \right], \quad t \geq 0, \\ \int\limits_{-\infty}^t QU^{-1}(s) f(s)\, ds - \int\limits_t^0 (E-Q) U^{-1}(s) f(s)\, ds + \\ +(E-Q)D^- \left[\int\limits_0^\infty (E-P)U^{-1}(s) f(s)\, ds + \int\limits_{-\infty}^0 QU^{-1}(s) f(s)\, ds \right], \; t \leq 0 \end{cases} \tag{7}$$

is the generalized Green operator of the problem for solutions bounded on the entire axis, D^- - is the generalized inverse of D , mathcal$P_{N(D)} = E - D^- D$ and $\mathcal{P}_{N(D^*)} = E - DD^-$, c is an arbitrary constant element of the Banach space $\mathbf{X}$.

3 Main result

We now show that under condition from the theorem 1, the boundary value problem can be solved using the operator $B_0 = lU(\cdot) P \mathcal{P}_{N(D)} : \mathbf{X} \to \mathbf{Y}$.

Theorem 2. *Let's conditions from the theorem 1 are satisfied. If the operator*

$$B_0 : \mathbf{X} \longrightarrow \mathbf{Y}$$

acting from the Banach space $\mathbf{X}$ *into the Banach space* $\mathbf{Y}$ *is invertible in the generalized sense, then*

(i) in order that solutions of boundary value problem (1), (2) exist, it is necessary and sufficient that

$$\mathcal{P}_{N(B_0^*)}(\alpha - l((G[f])(\cdot))) = 0 \; ; \tag{8}$$

(ii) under condition (8) solutions of boundary value problem (1), (2) have the form

$$x(t,\overline{c}) = U(t)P\mathcal{P}_{N(D)}\mathcal{P}_{N(B_0)}\overline{c} + U(t)P\mathcal{P}_{N(D)}B_0^-(\alpha - l(G[f])(\cdot)) + (G[f])(t), \forall \overline{c} \in \mathbf{X},$$

where $(G[f])(\cdot)$ *- is generalized Green operator defined below;* B_0^- *- is generalized inverse of* B_0*,* $\mathcal{P}_{N(B_0^*)}$ *- projector, which project* $\mathbf{X}$ *onto the kernel of adjoint operator* B_0^**.*

Proof. *From the theorem 1, we have that the family of bounded solutions of the equation (1) has the form* $x(t,c) = U(t)P\mathcal{P}_{N(D)}c + (G[f])(t)$*. We substitute this solutions to the equation (2):*

$$l(U(\cdot)P\mathcal{P}_{N(D)}c + (G[f])(\cdot)) = \alpha.$$

Since the operator l *is linear we have :*

$$l(U(\cdot)P\mathcal{P}_{N(D)})c + l((G[f])(\cdot)) = \alpha,$$

and we have finally the operator equation :

$$B_0 c = \alpha - l((G[f])(\cdot)).$$

Since operator B_0 *is invertible in the generalized sence , then in order that solutions of the boundary value problem (1),(2) exist it is necessary and sufficient [5] that*

$$\mathcal{P}_{N(B_0^*)}(\alpha - l((G[f])(\cdot))) = 0.$$

If this condition is satisfied, then

$$c = \mathcal{P}_{N(B_0)}\overline{c} + B_0^-(\alpha - l((G[f])(\cdot))), \quad \forall \overline{c} \in \mathbf{X}.$$

Then the family of bounded solutions of the boundary value problem (1), (2) has the form:

$$x(t,\overline{c}) = U(t)P\mathcal{P}_{N(D)}\mathcal{P}_{N(B_0)}\overline{c} + U(t)P\mathcal{P}_{N(D)}B_0^-(\alpha - l((G[f])(\cdot))) + (G[f])(t)$$

Remark. *If* $\mathbf{Y} = \mathbf{X}\times\mathbf{X}$*,* $lx = (x(+\infty), x(-\infty)) = (\alpha,\alpha) \in \mathbf{X}\times\mathbf{X}$*, where* α *- equilibrium point of (1), then all bounded solutions of boundary value problem (1), (2) are homoclinic paths [6].*

4 Examples

1. We now illustrate the assertions proved above. Consider the next boundary value problem

$$\frac{dx}{dt} = A(t)x(t) + f(t), \tag{9}$$

$$lx(\cdot) = x(b) - x(a) = \alpha, \tag{10}$$

where $A(t)$ - is operator in the form of a countably-dimensional matrix that, for every real value t, acts on the Banach space $\mathbf{B} = l_p,\ p \in [1; +\infty)$ and

$$x(t) = col\{x_1(t), x_2(t), \dots x_k(t), \dots\} \ \in \ BC^1(R, l_p),$$

$$f(t) = col\{f_1(t), f_2(t), \dots, f_k(t), \dots\} \ \in \ BC(R, l_p)$$

- are countable vector - columns; $a, b \in R, b > 0, a < 0$;

$$\alpha = col\{\alpha_1, \alpha_2, \dots, \alpha_k, \dots\} \in l_p$$

- constant vector ($\alpha_i \in R, i \in N$).

Consider boundary value problem (9), (10) with the operator

$$A(t) = \begin{pmatrix} \multicolumn{3}{c}{\overbrace{\hspace{8em}}^{k}} & & \\ th\ t & 0 & 0 & \dots & \dots \\ 0 & th\ t & 0 & \dots & \dots \\ \dots & \dots & \dots & \dots & \dots \\ 0 & 0 & th\ t & \dots & \dots \\ 0 & 0 & 0 & -th\ t & \dots \\ \dots & \dots & \dots & \dots & \dots \end{pmatrix} : l_p \to l_p. \tag{11}$$

The evolution operator of system (9), (11) has the form:

$$U(t) = \begin{pmatrix} \multicolumn{3}{c}{\overbrace{\hspace{18em}}^{k}} & & \\ (e^t + e^{-t})/2 & 0 & 0 & \dots & \dots \\ 0 & (e^t + e^{-t})/2 & 0 & \dots & \dots \\ \dots & \dots & \dots & \dots & \dots \\ 0 & 0 & (e^t + e^{-t})/2 & \dots & \dots \\ 0 & 0 & 0 & 2/(e^t + e^{-t}) & \dots \\ \dots & \dots & \dots & \dots & \dots \end{pmatrix};$$

The operator inverse to $U(t)$ has the form

$$U^{-1}(t) = \begin{pmatrix} \multicolumn{3}{c}{\overbrace{\hspace{18em}}^{k}} & & \\ 2/(e^t + e^{-t}) & 0 & 0 & \dots & \dots \\ 0 & 2/(e^t + e^{-t}) & 0 & \dots & \dots \\ \dots & \dots & \dots & \dots & \dots \\ 0 & 0 & 2/(e^t + e^{-t}) & \dots & \dots \\ 0 & 0 & 0 & (e^t + e^{-t})/2 & \dots \\ \dots & \dots & \dots & \dots & \dots \end{pmatrix};$$

and the corresponding homogeneous system is exponentially - dichotmous on both semi-axes R_+ and R_- with the projectors

$$P = \begin{array}{l} \quad\overbrace{\hphantom{0 \qquad 0}}^{k} \\ \begin{pmatrix} 0 & 0 & \dots & \dots \\ \dots & \dots & \dots & \dots \\ 0 & 0 & \dots & \dots \\ 0 & 0 & 1 & \dots \\ 0 & 0 & 0 & \dots \\ \dots & \dots & \dots & \dots \end{pmatrix} \end{array} \quad and \quad Q = \begin{array}{l} \quad\overbrace{\hphantom{1 \qquad 0 \qquad \dots}}^{k} \\ \begin{pmatrix} 1 & 0 & \dots & \dots \\ \dots & \dots & \dots & \dots \\ 0 & \dots & 1 & \dots \\ 0 & 0 & 0 & \dots \\ 0 & 0 & 0 & \dots \\ \dots & \dots & \dots & \dots \end{pmatrix} \end{array}$$

, respectively. Thus, we have

$$D = P - (E - Q) = 0, \qquad \mathcal{P}_{N(D)} = \mathcal{P}_{N(D^*)} = E.$$

Since $dim R[\mathcal{P}_{N(D^*)}Q] = k,$ *then operator* $\mathcal{P}_{N(D^*)}Q$ *is finite-dimensional:*

$$H(t) = [\mathcal{P}_{N(D^*)}Q]U^{-1}(t) = \begin{array}{l} \quad\overbrace{\hphantom{1 \qquad 0 \qquad \dots}}^{k} \\ \begin{pmatrix} 1 & 0 & \dots & \dots \\ \dots & \dots & \dots & \dots \\ 0 & \dots & 1 & \dots \\ 0 & 0 & 0 & \dots \\ 0 & 0 & 0 & \dots \\ \dots & \dots & \dots & \dots \end{pmatrix} \end{array} U^{-1}(t) = diag\{H_k(t), 0\},$$

where

$$H_k(t) = \begin{pmatrix} 2/(e^t + e^{-t}) & \dots & 0 \\ \vdots & \ddots & \vdots \\ 0 & \dots & 2/(e^t + e^{-t}) \end{pmatrix} \text{ is a } k \times k - \text{ dimensional matrix .}$$

According theorem 1, for the existence of solutions of system (9), (11) bounded on the entire axis, it is necessary and sufficient that following conditions be satisfied:

$$\int_{-\infty}^{+\infty} H_k(t)f(t)dt = 0 \quad \Leftrightarrow \quad \begin{cases} \int_{-\infty}^{+\infty} \frac{f_1(t)}{e^t + e^{-t}} dt = 0 \\ \dots \\ \int_{-\infty}^{+\infty} \frac{f_k(t)}{e^t + e^{-t}} dt = 0. \end{cases} \tag{12}$$

Thus, in order that system (3), (11) have solutions bounded on the entire axis, it is necessary and sufficient that exactly k conditions be satisfied; the other functions $f_i(t)$ for all $i \geq k+1$ can be taken arbitrary from the class $BC(R, l_p)$. Moreover, system (3), (11) has countably many linearly independent bounded solutions. For example, as a vector function f from the class $BC(R, l_p)$, one can take an arbitrary vector function whose first k components are odd functions.

For solving boundary value problem we find the matrix B_0 :

$$B_0 = lU(\cdot)P\mathcal{P}_{N(D)} = U(b)P\mathcal{P}_{N(D)} - U(a)P\mathcal{P}_{N(D)},$$

and finally

$$B_0 = \begin{pmatrix} \overbrace{0 \quad\quad 0 \quad\quad \dots}^{k} & \dots & \dots & \dots \\ \dots \quad \dots \quad \dots & \dots & \dots & \dots \\ 0 \quad\quad \dots \quad\quad 0 & \dots & \dots & \dots \\ 0 \quad\quad \dots \quad\quad 0 & \frac{cha-chb}{cha\cdot chb} & \dots & \dots \\ 0 \quad\quad \dots \quad\quad 0 & \dots & \frac{cha-chb}{cha\cdot chb} & \dots \\ \dots \quad \dots \quad \dots & \dots & \dots & \dots \end{pmatrix} : l_p \to l_p.$$

Since $a \neq b$ then operator $\mathcal{P}_{N(B_0^*)}$ have the form :

$$\mathcal{P}_{N(B_0^*)} = \begin{pmatrix} \overbrace{1 \quad\quad 0 \quad\quad \dots}^{k} & \dots\dots\dots \\ \dots \quad \dots \quad \dots & \dots\dots\dots \\ 0 \quad\quad \dots \quad\quad 1 & \dots\dots\dots \\ 0 \quad\quad \dots \quad\quad 0 & 0 \ \dots\dots \\ 0 \quad\quad \dots \quad\quad 0 & \dots \ 0 \ \dots \\ \dots \quad \dots \quad \dots & \dots\dots\dots \end{pmatrix} : l_q \to l_q \ (1/p + 1/q = 1),$$

and

$$G[f](b) - G[f](a) = \begin{pmatrix} -\int_{-\infty}^{a} \frac{2f_1(s)}{e^s+e^{-s}}ds - \int_{b}^{+\infty} \frac{2f_1(s)}{e^s+e^{-s}}ds \\ \dots \\ -\int_{-\infty}^{a} \frac{2f_k(s)}{e^s+e^{-s}}ds - \int_{b}^{+\infty} \frac{2f_k(s)}{e^s+e^{-s}}ds \\ \\ \frac{1}{2}\int_a^b (e^s + e^{-s}) f_{k+1}(s)ds \\ \dots \end{pmatrix}.$$

$$\mathcal{P}_{N(B_0^*)}(\alpha - l(G[f])(\cdot)) = 0 \quad \Leftrightarrow \quad \begin{cases} \int_{-\infty}^{a} \frac{2f_1(s)}{e^s+e^{-s}}ds + \int_{b}^{+\infty} \frac{2f_1(s)}{e^s+e^{-s}}ds = -\alpha_1 \\ \dots \\ \int_{-\infty}^{a} \frac{2f_k(s)}{e^s+e^{-s}}ds + \int_{b}^{+\infty} \frac{2f_k(s)}{e^s+e^{-s}}ds = -\alpha_k. \end{cases} \tag{13}$$

Thus, according to Theorem 2, boundary value problem (9), (10), (11) possesses at least one solution bounded on R if and only if the vector-function f satisfies conditions (12), (13).

2.Consider one-dimensional boundary value problem

$$\frac{dx(t)}{dt} = -tht\ x(t) + f(t),$$

$$lx = (x(+\infty), x(-\infty)) = (\alpha_1, \alpha_2) \in R^2. \tag{14}$$

a) let $f(t) = \frac{2e^{-t}}{e^t+e^{-t}}$ and $(\alpha_1, \alpha_2) = (0, -2)$. The set of bounded solutions which satisfy boundary condition (14) have the form:

$$x(t, c) = \frac{2}{e^t + e^{-t}}\ c - \frac{2e^{-t}}{e^t + e^{-t}} + \frac{2}{e^t + e^{-t}},\ \textit{for all}\ c \in R.$$

Integral curves for different values of the parameter c are shown in Figure 1.

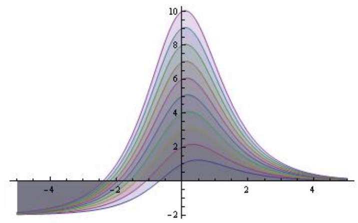

Fig. 1. Integral curves for different values of the parameter c

b) let $f(t) = 2\ tht$ and $(\alpha_1, \alpha_2) = (2, 2)$. In this case equation (1) has equilibrium solution $x_0(t) = 2$ and a set of homoclinic paths have the next form:

$$x(t, c) = \frac{2}{e^t + e^{-t}}\ c + 2 - \frac{4}{e^t + e^{-t}},\ for\ all\ c \in R.$$

Integral curves for different values of the parameter c are shown in Figure 2.

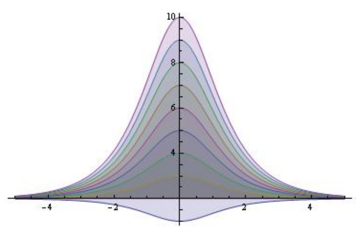

Fig. 2. Integral curves for different values of the parameter c

3. Consider two-dimensional boundary value problem

$$\frac{dx_1(t)}{dt} = -tht\ x_1(t) + f_1(t),$$

$$\frac{dx_2(t)}{dt} = -tht\ x_2(t) + f_2(t),$$

$$l(x_1, x_2) = (x_1(+\infty), x_1(-\infty), x_2(+\infty), x_2(-\infty)) = (\alpha_1, \alpha_2, \alpha_3, \alpha_4) = (0, -2, 2, 2) \in R^4,$$

where $f_1(t) = \frac{2e^{-t}}{e^t+e^{-t}}, f_2(t) = 2\ tht$ (direct product of examples 2a, 2b). This problem has a two-parametric family of bounded solutions

$$\begin{aligned} x_1(t, c_1) &= \tfrac{2}{e^t+e^{-t}}\ c_1 - \tfrac{2e^{-t}}{e^t+e^{-t}} + \tfrac{2}{e^t+e^{-t}}, \\ x_2(t, c_2) &= \tfrac{2}{e^t+e^{-t}}\ c_2 + 2 - \tfrac{4}{e^t+e^{-t}}, \end{aligned} \quad for\ all\ c_1, c_2 \in R.$$

The phase portrait of this system is shown for different parameters in Figure 3 (in plane x_1, x_2).

We see that the portrait resembles a horseshoe.

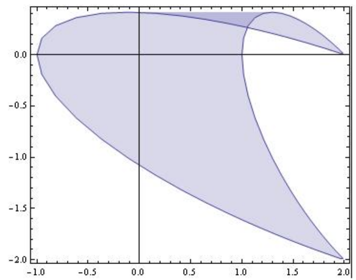

Fig. 3. The phase portrait of system

References

1. *Yu. M. Daletskii and M. G. Krein, Stability of Solutions of Differential Equations in Banach Space. Nauka, Moscow. 1970 (in Russian).*
2. *K. J. Palmer. Exponential dichotomies and transversal homoclinic points. J. Different. Equat.* **55***.-1984. P. 225–256.*
3. *Sacker R.J., Sell G.R. Dichotomies for Linear Evolutionary Equaitons in Banach Spaces. Journal of Differential Equations. 113, 17-67, 1994.*
4. *A. A. Boichuk and A.A. Pokutnij. Bounded solutions of linear differential equations in Banach space. Nonlinear Oscillations,* **9***, no 1. - 2006. - P. 3-14; http://www.springer.com/.*
5. *A. A. Boichuk and A. M. Samoilenko, Generalized Inverse Operators and Fredholm Boundary-Value Problems. VSP, Utrecht - Boston. 2004.*
6. *Guckenheimer J., Holmes Ph. Nonlinear Oscillations, Dynamical Systems, and Bifurcations of Vector Fields. 2002. - 235p.*

Chaotic Modeling and Simulation (CMSIM) 2: 257–264, 2013

Analysis of 1-D Linear Piecewise-smooth Discontinuous Map

Bhooshan Rajpathak[1], Harish Pillai[1], and Santanu Bandyopadhyay[1]

Indian Institute of Technology Bombay, Mumbai, India
(E-mail: bhooshanar@iitb.ac.in)
(E-mail: hp@iitb.ac.in)
(E-mail: santanu@iitb.ac.in)

Abstract. In this paper we analyze the stable periodic orbits existing in the 1-D linear piecewise-smooth discontinuous map with respect to variations in the parameters of the map. We analytically show how to calculate the range of parameter μ such that the orbits of specific periodicity can exist. Moreover, for a given period, the relation between the probability of occurrence of orbits of that period and the corresponding length of range of μ is established. Further, we show that this probability can be maximized by varying the parameter of the map. We prove that there exist a unique value of this parameter such that this probability is maximum. We provide diagrams generated by numerical simulations to illustrate these results and to depict the effects of variations in the parameters of the map on the ranges of existence of orbits.
Keywords: Border collision bifurcation, piecewise-smooth, discontinuous map, periodic orbit.

1 Introduction

Piecewise-smooth dynamical systems are being extensively studied over the last decade because of their applications in various fields like electrical engineering, physics, economics etc. Examples are DC-DC converters in discontinuous mode [1,2], impact oscillators [3], economic models [4] etc. One of the major reasons for interest in piecewise-smooth systems is the existence of a phenomenon, unique to such systems, called *border collision bifurcation*. Though this term was coined by Nusse [5] in 1992, the phenomenon was earlier reported by Feigin [6] in 70's.

The 1-D linear piecewise-smooth discontinuous map is defined as [7]:

$$x_{n+1} = f(x_n, a, b, \mu, l) = \begin{cases} ax_n + \mu & \text{for } x_n \leqslant 0 \\ bx_n + \mu + l & \text{for } x_n > 0 \end{cases} \tag{1}$$

Over the last decade, several authors have published the analytical as well as numerical work which analyzes the 1-D piecewise-smooth discontinuous map in detail [8–11]. Recently in [12] it was shown that exactly $\phi(n)$ stable periodic

Received: 30 March 2012 / Accepted: 15 October 2012

ISSN 2241-0503

orbits exist in the map given by Equation (1) when $a, b \in (0,1)$, $l = -1$ and $\mu \in (0,1)$; where n is the period and ϕ is Euler's number. In this paper we extend this analysis to investigate the effect of variation in parameters a, b and n on the range of existence of periodic orbits.

1.1 Notation

Let $\mathcal{L} := (-\infty, 0]$ (the closed left half plane) and $\mathcal{R} := (0, \infty)$ (the open right half plane). Given a particular sequence of points $\{x_n\}_{n \geqslant 0}$ through which the system evolves, one can convert this sequence into a sequence of $\mathcal{L}s$ and $\mathcal{R}s$ by indicating which of the two sets ($\mathcal{L}$ or $\mathcal{R}$) the corresponding point belongs to. Since a periodic orbit has a string of $\mathcal{L}s$ and $\mathcal{R}$ that keeps repeating, we call this repeating string, a *pattern* and denote it by σ. The length of the string σ is denoted by $|\sigma|$ and gives the number of symbols in the pattern i.e., the period of the orbit. The range of existence of this pattern σ is denoted by $P_\sigma = (p_1, p_02]$ where p_2 and p_1 are the upper and the lower limits respectively. The sum of geometric series $1 + k + k^2 + \cdots + k^n$ is denoted by S_n^k.

1.2 Preliminaries

Definition 1. A pattern σ is termed *admissible* if $P_\sigma \neq \varnothing$.

Definition 2. If a pattern consists of a single chain of consecutive $\mathcal{L}s$ followed by a singleton $\mathcal{R}$ then it called an $\mathcal{L}$-prime pattern. Similarly, if a pattern consists of a single chain of consecutive $\mathcal{R}s$ followed by a singleton $\mathcal{L}$ then it called an $\mathcal{R}$-prime pattern. Together, we call them *prime patterns*.

Example 1. $\mathcal{L}^n\mathcal{R}$ is a $\mathcal{L}$-prime pattern and $\mathcal{L}\mathcal{R}^n$ is a $\mathcal{R}$-prime pattern. $\mathcal{L}\mathcal{R}$ is both $\mathcal{L}$-prime as well as $\mathcal{R}$-prime.

Definition 3. A pattern made up of two or more prime patterns is called a composite pattern.

Example 2. $\mathcal{LLLRLLR}$ is a composite pattern as it is made of two prime patterns namely $\mathcal{LLLR}$ and $\mathcal{LLR}$.

Remark 1. Some authors use the term *maximal* or *principal* to describe prime pattern [13].

Recall that the range of existence of an orbit is denoted by P_σ. We illustrate with an example how to calculate P_σ.

Example 3. Consider a pattern $\mathcal{LLR}$ which means: $x_0, x_1 \leqslant 0, x_1 > 0$ and $x_3 = x_0$. Using Equation (1) these inequalities can be rewritten as:

$$
\begin{aligned}
&x_0 \leqslant 0,\\
&x_1 = ax_0 + \mu \leqslant 0,\\
&x_2 = a^2x_0 + (a+1)\mu > 0,\\
&x_3 = x_0 = a^2bx_0 + (ab+b+1)\mu - 1 \Rightarrow x_0 = \frac{(ab+b+1)\mu - 1}{1 - a^2b}.
\end{aligned}
$$

Substituting the value of x_0 in x_1 and x_2 we get:

$$x_1 = a\Big(\frac{(ab+b+1)\mu - 1}{1-a^2b}\Big) + \mu \leqslant 0,$$
$$x_2 = a^2\Big(\frac{(ab+b+1)\mu - 1}{1-a^2b}\Big) + (a+1)\mu > 0.$$

After simplification we get:

$$\mu > \frac{a^2}{a^2+a+1},$$
$$\mu \leqslant \frac{a}{ab+a+1}.$$

Hence, $\mathcal{P}_{\mathcal{LLR}} = \Big(\frac{a^2}{a^2+a+1}, \frac{a}{ab+a+1}\Big]$.

In a similar way we can find the range of existence (P_σ) for the prime patterns $\mathcal{L}^n\mathcal{R}$ and $\mathcal{LR}^n$ for any $n \geqslant 2$. The method is explained in detail in [12]. We directly use the formulas from [12] here:

$$\mathcal{P}_{\mathcal{L}^n\mathcal{R}} = \left(\frac{a^n}{S_n^a}, \quad \frac{a^{n-1}}{a^{n-1}b + S_{n-1}^a}\right] \tag{2}$$

and

$$\mathcal{P}_{\mathcal{LR}^n} = \left(\frac{ab^{n-1} + S_{n-2}^b}{ab^{n-1} + S_{n-1}^b}, \quad \frac{S_{n-1}^b}{S_n^b}\right]. \tag{3}$$

1.3 Characterization of Patterns

We have seen earlier that the prime patterns are admissible and the range of existence of prime patterns is given by Equations (2) and (3). The immediate question is other than prime patterns, which type of patterns are admissible? It is shown in [12] that only specific type of patterns are admissible. For example, it is shown that admissible patterns can not contain consecutive chain of $\mathcal{L}s$ and $\mathcal{R}s$ simultaneously. Moreover, admissible composite patterns are always made up of exactly two prime patterns of successive lengths. Further, it is shown that these results lead to the final conclusion that exactly $\phi(n)$ number of distinct patterns are admissible for a given n.

For a given n, the algorithm to generate the $\phi(n)$ patterns and to calculate the range of existence of these patterns is discussed in detail in [12]. We now extend this analysis to find out the effects of variations in parameters on the range of existence of patterns.

2 Effects of Variations in Parameters on The Range of Existence of Patterns

In this section we analyze the effects of variations in parameters a, b and n on the range of existence of patterns. Recall that the range of existence of pattern

σ is expressed as $\mathcal{P}_\sigma = (p_1, p_2]$. Let the length occupied on the parameter line μ corresponding to the i^{th} pattern of length n is denoted by Γ_i^n. That is, $\Gamma_i^n = p_2 - p_1$. Let the total length occupied corresponding to all the patterns of length n is denoted by Γ^n. That is, $\Gamma^n = \sum_{i=1}^{\phi(n)} \Gamma_i^n$. We now find out the expression for Γ^n. In this paper we consider the case of $a = b$.

Consider the pattern of length $N = n+1$. We substitute $a = b$ in Equations (2) and (3) to get:

$$P_{\mathcal{L}^n\mathcal{R}} = \left(\frac{a^n}{S_n^a}, \frac{a^{n-1}}{S_n^a}\right] \text{ and } P_{\mathcal{L}\mathcal{R}^n} = \left(\frac{a^n+S_{n-2}^a}{S_n^a}, \frac{S_{n-1}^a}{S_n^a}\right].$$

Note that $\Gamma_{P_{\mathcal{L}^n\mathcal{R}}}^N = \Gamma_{P_{\mathcal{L}\mathcal{R}^n}}^N = \frac{a^{n-1}(1-a)}{S_n^a}$. We denote it by γ^N. Since, for $a = b$ the map becomes symmetric, all the patterns of length N have $\Gamma_i^N = \gamma^N$. This gives $\Gamma^N = \sum_{i=1}^{\phi(N)} \Gamma_i^N = \phi(N)\gamma^N$. Substituting for γ^N and N we get $\Gamma^{n+1} = \phi(n+1)\frac{a^{n-1}(1-a)}{S_n^a} = \phi(n+1)\frac{a^{n-1}(1-a)^2}{1-a^{n+1}}$. For consistency, we use the formula for n which is:

$$\Gamma^n = \phi(n)\gamma^n = \phi(n)\frac{a^{n-2}(1-a)^2}{1-a^n}. \tag{4}$$

From the above equation it is clear that Γ^n depends on the parameters a and n. Recall that Γ^n is the length of range of existence of patterns as defined earlier. Hence, any change in Γ^n due to the variations in a and n can be interpreted as the effect on the range of existence of patterns.

2.1 Probability of Occurrence of a Pattern

We have seen that the total length occupied on the parameter line μ corresponding to all the patterns of length n is expressed by Γ^n. We know $\mu \in (0, 1)$. This leads us to the question: for a randomly selected μ from the set $(0, 1)$, what is the probability that it corresponds to a pattern of length n? Since $\mu \in (0, 1)$, the total length of the parameter line is unity and Γ^n is the total length occupied on parameter line μ corresponding to all the patterns of length n. Hence, the probability of occurrence of a pattern of length n is Γ^n. The Equation (4) gives the formula for this probability in terms of a and n.

2.2 Maximizing the Probability of Occurrence of a Pattern

For $n = 2$, $\Gamma^2 = \frac{1-a}{1+a}$ and $a \in (0, 1)$. Clearly, it is a monotonically decreasing function. Hence, the suprimum is achieved at $a = 0$. For all $n > 2$, Γ_n is not monotonic. With bit more analysis we can show that Γ^n attains maxima for a particular value of $a \in (0, 1)$. This can be calculated by differentiating Γ^n with respect to a.

$$\frac{d}{da}(\Gamma^n) = \frac{d}{da}(\phi(n)\gamma^n) = \phi(n)\left(a^n - \frac{n}{2}a + \frac{n}{2} - 1\right). \tag{5}$$

We check that the expression $a^n - \frac{n}{2}a + \frac{n}{2} - 1$ has only one real root in $(0, 1)$. At that root, $\frac{d^2}{da^2}(\Gamma^n) = a^{n-1} - \frac{1}{2}$ is negative. Hence, for a given n, there is an unique value of a such that Γ_n is maximum.

Example 4. We plot Γ^n versus n for different values of a. In these plots, n is varied from 2 to 14. These graphs (see Figure 1a to Figure 1e) show that as n increases, the position of maxima for Γ_n increases too. This means, higher the value of a, greater is the probability of occurrence of high period orbits. For the same values of a, figures 1b to 1f shows the bifurcation diagrams. We note that above results are validated by the bifurcation diagrams.

The graphs of Γ^n versus a, for different values of n, are plotted in figures from 1g to 1i. In these plots, a is varied from 0.01 to 0.99. From these plots we can see that Γ^2 is indeed a monotonically decreasing function. For vary small values of a, Γ_2 almost completely occupies the parameter line. For example, when $a = 0.1$, $\Gamma^2 = 0.818$. For all $n > 2$ is clear from the graphs that Γ^n is not monotonic and the maxima attained varies as n changes.

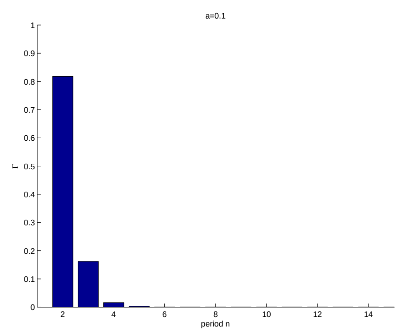

Fig. 1a. Graph showing Γ^n for different values of n. $a = 0.1$

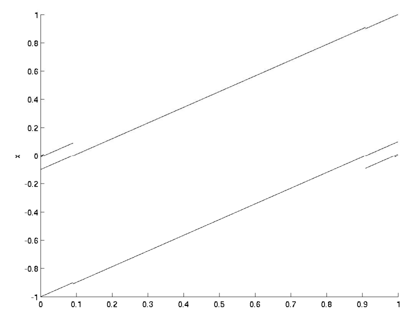

Fig. 1b. Bifurcation Diagram for $a = b = 0.1$

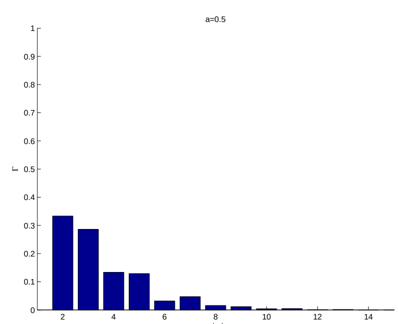

Fig. 1c. Graph showing Γ^n for different values of n. $a = 0.5$

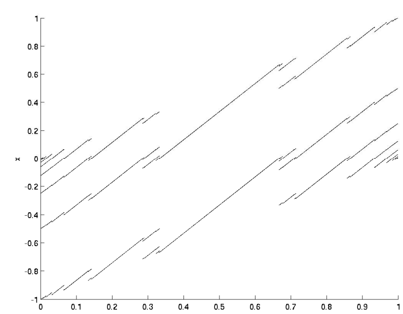

Fig. 1d. Bifurcation Diagram for $a = b = 0.5$

2.3 Patterns Completely Span The Parameter Line μ

We know that Γ^n gives the total length occupied on the parameter line μ corresponding to all the patterns of length n. We have shown that for $a = b$,

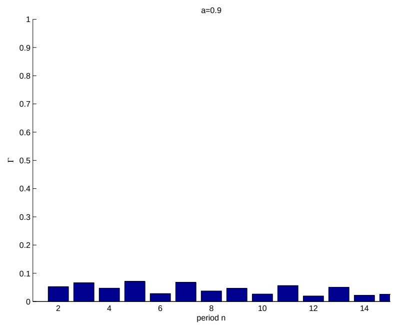

Fig. 1e. Graph showing Γ^n for different values of n. $a = 0.9$

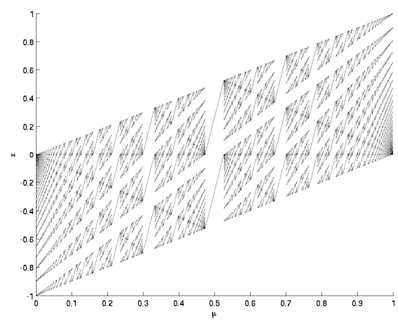

Fig. 1f. Bifurcation Diagram for $a = b = 0.9$

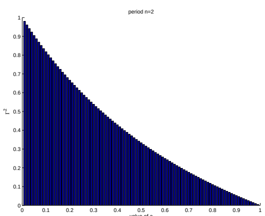

Fig. 1g. Graph showing Γ^n for different values of a. $n = 2$

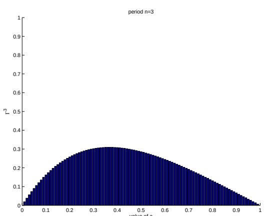

Fig. 1h. Graph showing Γ^n for different values of a. $n = 3$

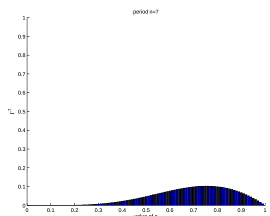

Fig. 1i. Graph showing Γ^n for different values of a. $n = 7$

Γ^n can be maximized by appropriately choosing the value of a. Now let the total length occupied on the parameter line μ corresponding to all the possible patterns be denoted by Γ. That is, $\Gamma = \sum_{n=2}^{\infty} \Gamma^n$. The following lemma proves that $\Gamma = 1$ and it completely spans the parameter line μ.

Lemma 1. *For every $\mu \in (0, 1)$, there exists a pattern.*

Proof. We know that $P_{\mathcal{L}^n\mathcal{R}} = (\sigma_1, \sigma_2] = \left(\frac{a^n}{S_n^a}, \quad \frac{a^{n-1}}{a^{n-1}b + S_{n-1}^a}\right]$ and $P_{\mathcal{L}^{n-1}\mathcal{R}} = (\sigma_1', \sigma_2'] = \left(\frac{a^{n-1}}{S_{n-1}^a}, \quad \frac{a^{n-2}}{a^{n-2}b + S_{n-2}^a}\right]$. Hence, for any arbitrarily given $\mu \in (0, 1)$ we can find an 'n' such that

Step 1: either $\mu \in P_{\mathcal{L}^n\mathcal{R}}$ or $\mu \in P_{\mathcal{L}^{n-1}\mathcal{R}}$ or $\sigma_2 < \mu < \sigma_1'$.

For the first two cases the pattern exists as μ belongs to the range of existence of a pattern. For the last case we proceed further by calculating $\mathcal{P}_{\mathcal{L}^{\mathrm{n}}\mathcal{R}\mathcal{L}^{\mathrm{n}-1}\mathcal{R}} = (\sigma_1'', \sigma_2'']$. Now again we have three cases:

Step 2: either $\mu \in \mathcal{P}_{\mathcal{L}^{\mathrm{n}}\mathcal{R}\mathcal{L}^{\mathrm{n}-1}\mathcal{R}}$ or $\sigma_2 < \mu < \sigma_1''$ or $\sigma_2'' < \mu < \sigma_1'$.

For the first case the pattern exists as μ belongs to the range of existence of a pattern. For the second case we again go to Step 1 but this time with $P_{\mathcal{L}^n\mathcal{R}}$ and $\mathcal{P}_{\mathcal{L}^{\mathrm{n}}\mathcal{R}\mathcal{L}^{\mathrm{n}-1}\mathcal{R}}$. Similarly for the third case we go to Step 1 with $\mathcal{P}_{\mathcal{L}^{\mathrm{n}}\mathcal{R}\mathcal{L}^{\mathrm{n}-1}\mathcal{R}}$ and $P_{\mathcal{L}^{n-1}\mathcal{R}}$. Without the loss of generality we assume the second case to be true i.e. μ always lay in the left side partition or nearer to $P_{\mathcal{L}^n\mathcal{R}}$. Then, before every time we take Step 2, we construct the new pattern of form $(\mathcal{L}^{\mathrm{n}}\mathcal{R})^{\mathrm{k}}\mathcal{L}^{\mathrm{n}-1}\mathcal{R}$

with $k = 2, 3, 4 \ldots$ With the help of generalized map method explained in [12] this pattern can be written as $\mathcal{L}'^{\mathrm{k}}\mathcal{R}'$ where, $\mathcal{L}' = \mathcal{L}^{\mathrm{n}}\mathcal{R}$ and $\mathcal{R}' = \mathcal{L}^{\mathrm{n}-1}\mathcal{R}$.

This process is nothing but constructing a series of intervals $\mathcal{P}_{\mathcal{L}'^{\mathrm{k}}\mathcal{R}'}$. This series of intervals must converge at σ_2. This is because, if it converges at some other point (say $\tilde{\sigma_1}$) then we get a finite length subinterval $(\sigma_2, \tilde{\sigma_1}]$. We arbitrarily select any point from this interval (say $\tilde{\mu}$). Now as we argued for the case of $P_{\mathcal{L}^n\mathcal{R}}$, similar arguments can be made here i.e. we can select a large enough k (since limits of $\mathcal{P}_{\mathcal{L}'^{\mathrm{k}}\mathcal{R}'}$ involve a and b with k in power) such that $\mathcal{P}_{\mathcal{L}'^{\mathrm{k}}\mathcal{R}'}$ lies to the left of $\tilde{\mu}$. This is contradiction to the earlier assumption that series converges to $\tilde{\sigma}$. Hence, the series must converge to σ_2.

3 Conclusions

In this paper we have analyzed the stable periodic orbits of the 1-D linear piecewise-smooth discontinuous map with respect to change in the parameters. We have analytically calculated the range of parameters for which period-n orbits exist. The length of this range is considered as the probability of occurrence of period-n orbit. Further, we have shown that this probability can be maximized by varying the parameter of the map and we prove that there exist an unique value of this parameter such that this probability is maximum.

References

1. J. H. B. Deane and D. C. Hamill, "Instability, subharmonics and chaos in power electronics circuits," in *Power Electronics Specialists Conference*, vol. 1. IEEE, June 1990, pp. 34–42.
2. C. K. Tse, "Flip bifurcation and chaos in three-state boost switching regulators," *IEEE Transactions on Circuits and Systems I: Fundamental Theory and Applications*, vol. 41, no. 1, pp. 16–23, Jan 1994.
3. E. Pavlovskaia, M. Wiercigroch, and C. Grebogi, "Two-dimensional map for impact oscillator with drift," *Physical Review E*, vol. 70, no. 3, pp. 362 011–362 019, September 2004.
4. F. Tramontana, L. Gardini, and F. Westerhoff, "Heterogeneous speculators and asset price dynamics: Further results from a one-dimensional discontinuous piecewise-linear map," *Computational Economics*, vol. 38, no. 3, pp. 329–347, October 2011.
5. H. Nusse and J. Yorke, "Border-collision bifurcations including period two to period three for piecewise smooth systems," *Physica D: Nonlinear Phenomena*, vol. 57, no. 1, pp. 39–57, June 1992.
6. M. Feigin, "Doubling of the oscillation period with c-bifurcations in piecewise-continuous systems," *Journal of Applied Mathematics and Mechanics*, vol. 34, pp. 861–869, 1970.
7. P. Jain and S. Banerjee, "Border collision bifurcation in one-dimensional discontinuous maps," *International Journal of Bifurcation and Chaos*, vol. 13, no. 11, pp. 3341–3351, November 2003.
8. S. Hogan, L. Higham, and T. Griffin, "Dynamics of a piecewise linear map with a gap," *Proceedings of the Royal Society A: Mathematical, Physical and Engineering Sciences*, vol. 463, no. 2077, pp. 49–65, January 2006.

9. V. Avrutin, A. Granados, and M. Schanz, "Sufficient conditions for a period incrementing big bang bifurcation in one-dimensional maps," *Nonlinearity*, vol. 24, no. 9, pp. 22 475–2598, September 2011.
10. V. Avrutin, M. Schanz, and B. Schenke, "Coexistence of the bandcount-adding and bandcount-increment scenario," *Discrete Dynamics in Nature and Society*, vol. 2011, no. 681565, pp. 1–30, January 2011.
11. L. Gardini and F. Tramontana, "Border collision bifurcation curves and their classification in a family of 1d discontinuous maps," *Chaos, Solitons & Fractals*, vol. 44, no. 4-5, pp. 248–259, May 2011.
12. B. Rajpathak, H. Pillai, and S. Bandyopadhyay, "Analysis of stable periodic orbits in the 1-d linear piecewise-smooth discontinuous map," arxiv:1203.5897 [math.DS].
13. V. Avrutin and M. Schanz, "On multi-parametric bifurcation in a scalar piecewise-linear map," *Nonlinearity*, vol. 19, no. 3, pp. 531–552, March 2006.

Chaotic Modeling and Simulation (CMSIM) 2: 265–272, 2013

Observation of Chaotic behaviour in the CCJJ+DC model of Coupled Josephson Junctions

André E Botha[1] and Yu. M. Shukrinov[2]

[1] Department of Physics, University of South Africa, P.O. Box 392, Pretoria 0003, South Africa
(E-mail: bothaae@unisa.ac.za)
[2] Bogoliubov Laboratory of Theoretical Physics, Joint Institute for Nuclear Research, Dubna, Moscow Region, 141980, Russia
(E-mail: shukrinv@theo.jinr.ru)

Abstract. Erratic behaviour in the simulated current-voltage characteristics of coupled intrinsic Josephson junctions, for certain ranges of the parameters, are observed and are shown to be chaotic in origin. In order to demonstrate the chaotic origin of the erratic behaviour, the Lyapunov exponents for the system are calculated. System trajectories and their Poincaré maps are used to confirm the chaotic signature obtained from the Lyapunov spectrum in certain ranges of the bias current, below the break point current.
Keywords: Chaos; Hyperchaos; CCJJ+DC model; Intrinsic Josephson Junctions.

1 Introduction

Systems of coupled intrinsic Josephson junctions (IJJs) are prospective candidates for the development of superconducting electronic devices [1]. Questions about their dynamics are, for a variety of reasons, of great technological importance [2]. For example, systems of junctions can produce much greater power output that a single junction and they also provide a model which may help to elucidate the physics of high temperature superconductors (HTSC) [3,4]. The intrinsic Josephson effect (IJE) [5], i.e. tunneling of Cooper pairs between superconducting layers inside of strongly anisotropic layered HTSC, provides a further motivation for considering HTSC as stacks of coupled Josephson junctions. The IJE also plays an important role in determining the current voltage characteristics (CVC) of tunneling structures based on HTSC and the properties of the vortex structures in these materials.

Although there has been a recent report on the hyperchaotic behaviour of an array of two resistive-capacitive-inductive-shunted Josephson junctions [6], the so-called RCLSJJ model [7], chaotic behaviour does not feature in

Received: 30 March 2012 / Accepted: 12 September 2012

ISSN 2241-0503

the literature on other closely-related phenomenological models; such as, the capacitively-coupled model (CCJJ) [8], the resistive-capacitive shunted model (RCSJJ) [5,9], or the CCJJ plus diffusion current (DC) model [10,11] of the present work. One possible reason for the comparatively late discovery of chaos in these systems may be that the (often subtle) chaotic features may have been masked by numerical instability and added noise in simulations.

This paper is organized as follows. In Section 2 we present the CCJJ+DC model and describe the numerical method used to calculate the Lyapunov exponents. In Section 3 we describe the observation of erratic behaviour in the CVC, which led to the discovery of chaos in the model. In section 4 we demonstrate that the erratic behaviour is chaotic in origin by looking as the Lyapunov exponents, system trajectories and Poincaré maps. In Section 5 we conclude that the erratic behaviour is chaotic in origin and that experimental investigations are required to ascertain whether this feature of the model is observable in real systems that satisfy the assumptions of the CCJJ+DC model. We also suggest that further work could be done on developing methods for controlling the observed chaos (hyperchaos) in this model.

2 Theory and simulation methods

2.1 The CCJJ+DC model

We solve the system of dynamical equations for the gauge-invariant phase differences $\varphi_\ell(\tau) = \theta_{\ell+1}(\tau) - \theta_\ell(\tau) - \frac{2e}{\hbar}\int_\ell^{\ell+1} dz A_z(z,\tau)$ between superconducting layers (S-layers), for stacks consisting of different numbers of IJJs, within the framework of the CCJJ+DC model [12,13]. In this model, θ_ℓ is the phase of the order parameter in the ℓth S-layer and A_z is the vector potential in the insulating barrier. For a system of N junctions the equations are,

$$\frac{d\varphi_\ell}{d\tau} = \sum_{\ell'=1}^{N} A_{\ell\ell'} V_{\ell'} \quad \text{and} \tag{1}$$

$$\frac{dV_\ell}{d\tau} = I - \sin\varphi_\ell - \beta \sum_{\ell'=1}^{N} A_{\ell\ell'} V_{\ell'} \ , \tag{2}$$

where $\ell = 1, 2, \ldots, N$ and the matrix A contains coupling parameters such as α. Note that A differs in form depending on whether periodic or non-periodic boundary conditions (BCs) are used [14]. The dissipation parameter β is related to the McCumber parameter β_c as $\beta = 1/\sqrt{\beta_c}$. For the purpose of numerical simulations we make use of a dimensionless time parameter $\tau = t\omega_p$, where $\omega_p = \sqrt{2eI_c/(\hbar C)}$ is the plasma frequency, I_c is the critical current and C is the capacitance. We measure the DC voltage on each junction V_ℓ in units of the characteristic voltage $V_c = \hbar\omega_p/(2e)$ and the bias current I in units of I_c. The critical currents in these (series) systems can typically range from 1 to $1000\,\mu$A, corresponding to voltages of $RI_c \sim 1\,$mV across individual junctions. Further details concerning this model can be found in Refs. [14,15]

2.2 Calculation of Lyapunov exponents

The Lyapunov exponents of a nonlinear dynamical system provide a quantitative measure of the degree of chaos inherent in the system, i.e. they quantify the sensitivity of the system to changes in initial conditions [16]. Usually one Lyapunov exponent is associated with each independent coordinate in the system. The numerical value of this exponent then characterizes the long term average exponential convergence (negative exponent) or divergence (positive exponent) of that coordinate with respect to some arbitrarily small initial separation.

Although the calculation of the Lyapunov exponents is in principle straight forward, in numerical calculations one has to guard against cumulative round-off errors which occur because of the exponential manner in which the small initial differences in coordinates may be amplified. Since real experimental data sets are typically small and noisy, it has taken a sustained effort to develop efficient algorithms for estimating the Lyapunov exponents associated with chaotic data sets [17–20]. In the preset simulations, since the system of Eqns. (1) and (2) are know in analytical form, we make use of the well-known algorithm by Wolf *et al.* [17]. Unlike some other methods, which only calculate the maximal Lyapunov exponent [21,22], the algorithm by Wolf *et al.* calculates the full spectrum of Lyapunov exponents and thus allows one to distinguish between chaotic attractors, which are characterised by only one positive exponent, and hyperchaotic attractors, which is characterised by more than one positive exponent.

In addition to Eqs. (1) and (2), the algorithm by Wolf *et al.* requires analytical expressions for the action of the system Jacobian $\mathbf{J}$ on an arbitrary column vector $\mathbf{x} = (\varphi_1,\varphi_2,\ldots,\varphi_N,V_1,V_2,\ldots,V_N)^T$ in the (φ, V) coordinate space. For the present system the action of $\mathbf{J}$ on $\mathbf{x}$ is given by

$$\mathbf{Jx} = \begin{pmatrix} A_{11}V_1 + A_{12}V_2 + \ldots + A_{1N}V_N \\ A_{21}V_1 + A_{22}V_2 + \ldots + A_{2N}V_N \\ \vdots \\ A_{N1}V_1 + A_{N2}V_2 + \ldots + A_{NN}V_N \\ -\varphi_1\cos\varphi_1 - \beta A_{11}V_1 - \beta A_{12}V_2 - \ldots - \beta A_{1N}V_N \\ -\varphi_2\cos\varphi_2 - \beta A_{21}V_1 - \beta A_{22}V_2 - \ldots - \beta A_{2N}V_N \\ \vdots \\ -\varphi_N\cos\varphi_N - \beta A_{N1}V_1 - \beta A_{N2}V_2 - \ldots - \beta A_{NN}V_N \end{pmatrix} \tag{3}$$

To calculate the Lyapunov exponents for a particular current I, we typically used 30000 dimensionless time steps, with a step size of $\Delta\tau = 0.2$. In all our calculations the number of steps and step size were chosen so that the magnitude of the zero exponent always converged to a value which was at least two orders of magnitude smaller than the magnitude of the smallest non-zero exponent. A fifth-order Runge-Kutta integration scheme was used.

3 Observation of erratic behaviour in the CVC

Erratic behaviour was first observed in the simulated CVC for certain ranges of parameter values. Figure 1 presents the simulated outermost branches in the

CVC for a stack of nine IJJs. Here V is the sum of the time averaged voltages

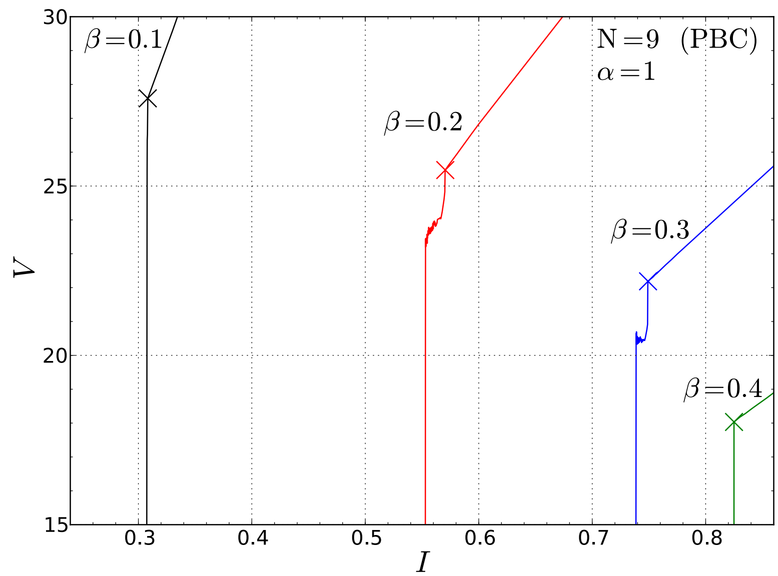

Fig. 1. Simulated outermost branches of the current voltage characteristics of an array with nine IJJ with $\alpha = 1$ and periodic boundary conditions (PBC). The curves for four different values of β are shown. The break point of each curve has been marked by a cross.

across each junction, i.e. $V = \langle V_1 \rangle + \langle V_2 \rangle + \ldots + \langle V_9 \rangle$, and I is bias current through the stack. As explained in Section 2.1, V and I are in units of V_c and I_c respectively. In Fig. 1 one can see the variation of the branch slope and the breakpoint (marked by a cross), for the four different values of dissipation parameter. As expected, the value of the break point current increases with increasing β; however, for $0.1 < \beta < 0.4$ the break point boarders on a so-called break point region (BPR). In Fig. 1 this region can be clearly seen to the left of the break points for the $\beta = 0.2$ and $\beta = 0.3$ curves. For these two values of β, erratic behaviour is observed to the left of each breakpoint. Initially this erratic behaviour was thought to be numerical in origin; however, as we will demonstrate in the next section, it is in fact chaotic.

4 Results and discussion

4.1 Demonstration of chaotic behaviour via Lyapunov exponents

Since we were unable to account for the observed erratic behaviour in terms of numerical instability, we decided to check whether or not the system is chaotic by calculating its Lyapunov exponents according to the method described in

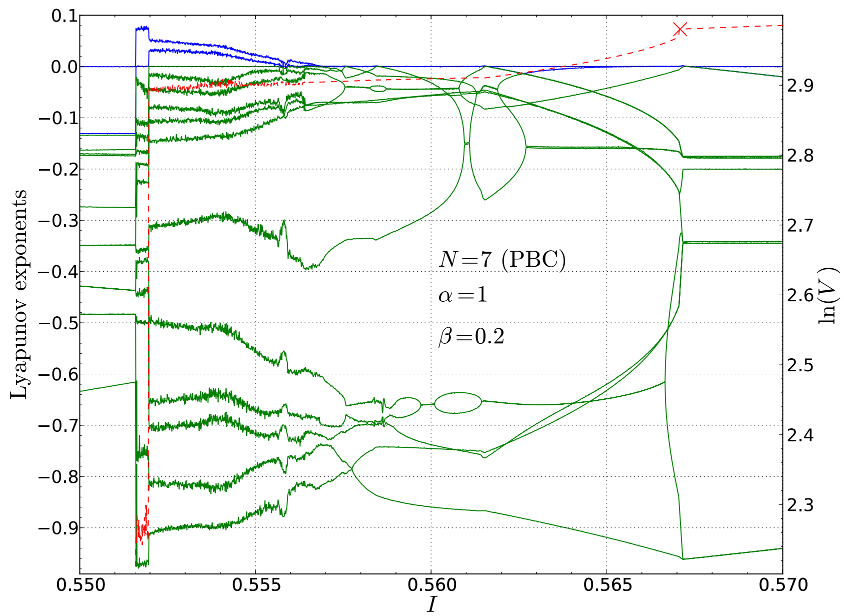

Fig. 2. Lyapunov exponents and CVC for a stack of seven IJJs with periodic boundary conditions.

Section 2.2. Typical results are shown in Fig. 2, for a stack of seven junctions, using the PBC. Here the left vertical axis is for the Lyapunov exponents $(\lambda_1, \ldots, \lambda_{14})$, while the right vertical axis is for $\ln(V)$ (red dashed curve). The largest two Lyapunov exponents, λ_1 and λ_2 (plotted in blue) both become positive exactly over the range of currents for which the erratic behaviour in V was observed, indicating that this system is hyperchaotic within the range $0.5520 < I < 0.5570$. In this range, as the current is decreased, λ_1 and λ_2 steadily increase, reaching their respective maxima of 0.052 and 0.031. At $I \approx 0.5520$ the system makes an abrupt transition to one of the inner branches of the CVC, over the range $0.5515 < I < 0.5520$. For the inner branch there is only one positive Lyapunov exponent ($\lambda_1 = 0.075$), which suggests that this transition may be associated with a change in the dynamics of the system, from hyperchaotic to chaotic. We have also performed other simulations at different parameter values and for N in the range 7-13, using both the PBC and NPBC. In all cases, for which erratic behaviour in the CVC was observed, we found either one or two positive Lyapunov exponent.

4.2 Comparison of system trajectories

To further verify that the observed behaviour is chaotic (hyperchaotic), we also looked at the system trajectory for a variety of different parameter values and initial conditions. Our observations are consistent with the values obtained for the Lyapunov exponents. For example, Fig. 3 shows a projection onto the $\varphi_3 V_5$-plane of two different trajectories corresponding to a nine junction system ($N = 9$) with periodic boundary conditions and the parameters $\alpha = 1$ and $\beta = 0.2$. Both trajectories correspond to the outer branch

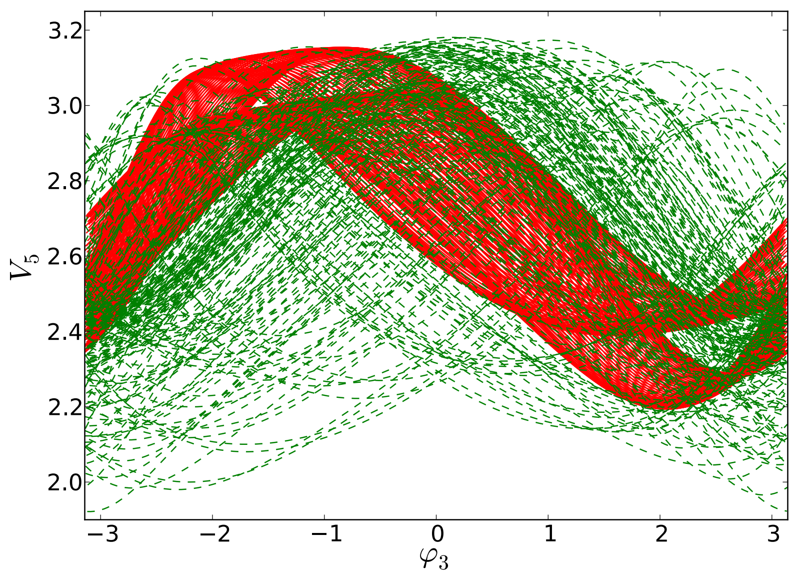

Fig. 3. A projection of two different system trajectories for a stack of nine IJJs with periodic boundary conditions. The solid red curve corresponds to a current above the break point value and is quasi-periodic, while the dashed green curve corresponds to a current below the break point, where the system is hyperchaotic.

of the CVC and have been integrated for 250 dimensionless time units. The solid red trajectory appears to be quasi-periodic, corresponding to $I = 0.5650$ and zero maximal Lyapunov exponent. The dashed green trajectory is hyperchaotic, corresponding to $I = 0.5575$, with the three largest exponents given by $\lambda_1 = 0.035$, $\lambda_2 = 0.022$ and $\lambda_3 = 0.00005$. In this figure the quasi-periodic nature of the non-chaotic trajectory (solid red curve) is clearly discernible from the hyperchaotic trajectory (dashed green curve).

4.3 Poincaré maps

To investigate further the differences between regular and chaotic regimes of the system, several Poincaré maps were constructed. Figure 4 shows a comparison of the maps for the trajectories described in Fig. 3. Here the intersection of the $V_3 V_9$-projection of the trajectory with the plane $V_2 = 2.6$ is shown. Note the intersection is only from one side of the $V_2 = 2.6$ plane, i.e. the map was constructed by plotting the coordinates (V_3, V_9) for each intersection point, defined by a change in V_2 from $V_2 - 2.6 \leq 0$ to $0 \leq V_2 - 2.6$, over one

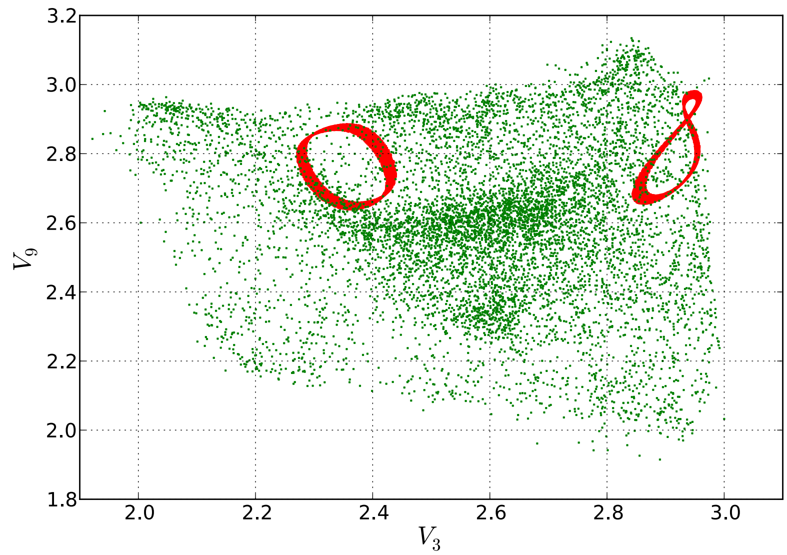

Fig. 4. Poincaré maps for the trajectories shown in Fig. 3. The intersection plane is given by $V_2 = 2.6$. The red pixels are for the intersection of the quasi-periodic trajectory while the green pixels are for the intersection of the hyperchaotic trajectory.

integration step. In order to obtain the large number of intersection points shown (between $8000 - 9000$ in each case) both trajectories were integrated for 20000 dimensionless time units, using a step size of $\Delta\tau = 0.025$. The quasi-periodic (hyperchaotic) behaviour of the red (green) trajectory is clearly visible, in agreement with Fig 3 and the calculated values of the Lyapunov exponents.

5 Conclusions

We have demonstrated that the observed erratic behaviour in our simulations of the CVC of coupled IJJs within the CCJJ+DC model is chaotic in origin. We have also shown that transitions can take place between hyperchaotic and chaotic dynamics, as the system jumps from the outermost CVC branch to inner branches. In this preliminary work we have not addressed many other important physical aspects; such as, the influence of the number of junctions, boundary conditions and charge correlations. A more detailed analysis of the chaos is currently in preparation [23].

In future work it would be interesting to establish whether or not the observed chaotic features in the present simulation are also experimentally observable in systems that satisfy the underlying assumptions of the CCJJ+DC model. Perhaps further work could also be done on controlling and exploiting (for technological use) the observed chaos (hyperchaos) in these systems.

References

1. R. Kleiner and P. Muller, Phys. Rev. B **94**, 1327 (1994).
2. L. Ozyuzer *et al.*, Science **318**, 1291 (2007).
3. K. Y. Tsang, R. E. Mirollo, S. H. Strogatz, and K. Wiesenfeld, Physica D **48**, 102 (1991).
4. S. H. Strogatz and R. E. Mirollo, Phys. Rev E **47**, 220 (1993).
5. W. Buckel and R. Kleiner, *Superconductivity: Fundamentals and Applications* (Wiley-VCH, Darmstadt, 2nd edition, 2004).
6. R. Ilmyong, F. Yu-Ling, Y. Zhi-Hai, and F. Jian, Chin. Phys. B **20**, 120504 (2011).
7. C. B. Whan and C. J. Lobb, Phys. Rev. E **53**, 405 (1996).
8. T. Koyama and M. Tachiki, Phys. Rev. B **54**, 16183 (1996).
9. C. B. Whan, C. J. Lobb, and M. G. Forrester, J. Appl. Phys. **77**, 382 (1995).
10. Y. M. Shukrinov, I. R. Rahmonov, and M. E. Demery, J. Phys.: Conf. Ser. **248**, 012042 (2010).
11. Y. M. Shukrinov and M. Hamdipour, Europhys. Lett. **92**, 37010 (2010).
12. M. Machida, T. Koyama, A. Tanaka, and M. Tachiki, Physica C **330**, 85 (2000).
13. Y. M. Shukrinov, F. Mahfouzi, and P. Seidel, Physica C **449**, 62 (2006).
14. Y. M. Shukrinov, F. Mahfouzi, and N. Pendersen, Phys. Rev. B **75**, 104508 (2007).
15. Y. M. Shukrinov and F. Mahfouzi, Phys. Rev. Lett. **98**, 157001 (2007).
16. J. C. Sprott, *Chaos and Time-Series Analysis* (Oxford University Press, London, 2003).
17. A. Wolf, J. B. Swift, H. L. Swinney, and J. A. Vastano, Physica D **16**, 285 (1985).
18. F. Sattin, Comput. Phy. Commun. **107**, 253 (1997).
19. T. Okushima, Phys. Rev. Lett. **91**, 254101 (2003).
20. Z.-M. Chen, K. Djidjeli, and W. G. Price, Applied Mathematics and Computation **174**, 982 (2006).
21. M. T. Rosenstein, J. J. Collins, and C. J. D. Luca, Physica D **65**, 117 (1993).
22. H. Kantz, Phys. Lett. A **185**, 77 (1994).
23. Y. M. Shukrinov, M. Hamdipour, M. R. Kolahchi, A. E. Botha, and M. Suzuki, Phys. Rev. B, in preparation.

Chaotic Modeling and Simulation (CMSIM) 2: 273–280, 2013

Analysis of FIPS 140-2 Test and Chaos-Based Pseudorandom Number Generator

Lequan Min, Tianyu Chen, and Hongyan Zang

Mathematics and Physics School, University of Science and Technology Beijing, Beijing 100083 China
(E-mails: `minlequan@sina.com, zhy_lixiang@126.com, cty_furmosi@sina.com`)

Abstract. Pseudo random numbers are used for various purposes. Pseudo random number generators (PRNGs) are useful tools to provide pseudo random numbers. The FIPS 140-2 test issued by the American National Institute of Standards and Technologyhas been widely used for the verifications the statistical properties of the randomness of the pseudo random numbers generated by PRNGs.

First this paper analyzes the FIPS 140-2 test. The results show that

- The required interval of the FIPS140-2 Monobit Test corresponds to the confident interval with significant level $\alpha = 0.0001(1 - \alpha)$.
- The required interval of the FIPS140-2 Pork Test corresponds to χ^2 test with significant level $\alpha = 0.0002$(1 - α).
- The required intervals of the FIPS140-2 Run Test correspond to the confident interval with significant level $\alpha = 0.00000016(1 - \alpha)$.

Second this study considers a novel chaotic map (NCM), whose prototype is the Lorenz three-dimensional Lorenz chaotic map. A NCP -based CPRNG is designed. Using the FIPS 140-2 test measures the 1000 keystreams randomly generated by the RC4 algorithm, and the 1000 keystreams generated by the CPRNG with perturbed randomly initial conditions in the range $|\epsilon| \in [10^{-16}, 10^{-4}]$. The results show that the statistical properties of the randomness of the sequences generated via the CPRNG and the RC4 do not have significant differences. The results confirm once again that suitable designed chaos-based PRNGs may generate sound random sequences, in particular for a replacement for the one-time pad system.
Keywords: FIPS 140-2 Test, Analysis in required intervals, Chaos-based pseudorandom number generator, RC4, Randomness comparison..

1 Introduction

Pseudorandom numbers are important in applications such as in simulations of physical systems[1], in cryptography[2], in Entertainment[3], and in protecting computer systems. John von Neumann was the first contributor in computer-based random number generators. Today algorithmic pseudorandom number

Received: 28 June 2012 / Accepted: 10 February 2013

ISSN 2241-0503

generators (PRNGs) have replaced almost random number tables and hardware random number generators in practical uses.

A algorithmic PRNG is an algorithm for generating sequences of numbers that approximate the properties of random numbers. A poor PRNG will lead to weak or guessable its keys, and leak the information which is prevented. There are many designed tests for measuring the randomness quantities of the sequences of numbers generated via PRNGs. The FIPS 140-2 test[4], the SP800-22 test[5], and the Diehard Battery test[6] are popular tests to be used in evaluating the randomness quantities of the sequence numbers deriving from PRNGs.

Since Lorenz's influential article[7] and Li and York's pioneer paper [8], the study of chaos has been rapidly developed. Matthews has first derived a chaotic encryption algorithm and shown that it may be suitable for a replacement for the one-time pad system[9].

Gámez-Guzmán et al. have considered a modified Chua's circuit generator of 5-scroll chaotic attractor and shown that it may have a potential application to transmit encrypted audio and image information[11]. Stojanovski and Kocarev [10] have analyzed the application of a chaos-based PRNG. Li et al.[12] have reported that using only 120 consecutive known plain-byres can broken the whole secret key of a multiple one-dimensional chaotic map -based PRNG. Yu et al[13] have introduced and analyzed a quadric polynomial chaotic map based PRNG by the FIPS PUB 140-2 test.

This paper analyzes the standards of the randomness criteria of the FIPS 140-2 test, introduces a novel chaotic map (NCM), designs a NCM-based PRNG. Using the FIPS 140-2 test measures and compares the randomness performances of the NCM-based PRNG and the RC4 algorithm – a famous algorithm PRNG used in computer prevent.

The rest of this paper is organized as follows. Section 2 discusses the standards of the randomness criteria of the FIPS 140-2 test. Section 3 introduces the NCM, stimulates numerically its dynamic orbits, designed the NCM-based PRNG. Section 4 compares the randomness quantities of the NCM-based PRNG and the RC4 PRNG. Section 5 gives concluding remarks.

2 Analysis of FIPS 140-2 Test

The FIPS 140-2 Test issued by the National Institute of Standard and Technology consists of four tests: Monobit test, Pork test, Run test and Long Run test. Each test needs a single stream of 20,000 one and zero bits from keystream generation. Any failure in the test means the sequence of stream must be rejected. The four test are listed as for follows:

(1) Monobit test: Count the numbers N of "0" and "1" in the 20,000 bitstream, respectively. The test is passed if the N is fallen into the required interval given in the second column in Table 1.
(2) Poker test: Divide a sequence of 20,000 into 5,000 consecutive 4-bit segments. Denote $f(i)$ to be the number of each 4-bit valve i where $0 < i < 15$.

Then calculate the following:

$$N = \frac{16}{5000}\sum_{i=1}^{16} f(i)^2 - 5000. \tag{1}$$

The test is passed if the N is fallen into the required interval given in the second column in Table 1.

(3) Run test: Run is defined as maximal sequence of consecutive bits of either all $'1'$ or all $'0'$ that is the part of a 20,000 bitstream. Count and store the run bits with ≥ 1. The test is passed if the length of each run is fallen into the required interval listed in the second column in Table 1.

(4) Long Run test: The test is passed if there are no runs of length 26 or more.

Table 1. The required intervals of the FIPS 140-2 Monobit Test Pork Tests and Run Test, and the calculated confident intervals of random sequences with different significant level $\alpha's$. Here MT, PT, and RT represent the Monobit Test, the Pork Test and the Run Test; k represents the length of the run of a tested sequence.

	FIPS 140-2 Standard	$\alpha = 10^{-4}$	Golomb's
	Required Interval	Confident Interval	Postulates
MT	9,725∼10,275	9,725∼10,275	10000
		$\alpha = 2 \times 10^{-4}$	
PT	2.16∼46.17	2.41∼44.26	16.01
RT	FIPS 140-2 Standard	$\alpha = 1.6 \times 10^{-7}$	Golomb's
k	Required Interval	Confident Interval	Postulates
1	2,315∼2,685	2,315∼2,685	2,500
2	1,114∼1,386	1,119∼1,381	1,250
3	527∼723	532∼718	625
4	240∼384	247∼378	313
5	103∼209	110∼203	156
6+	103∼209	110∼203	156

Golomb has proposed three postulates on the randomness that pseudorandom sequences should satisfy [14]:

1. **Balance Property**. In one period of a pseudorandom sequence, If the period p is even, then the number of ones is equal to the number of zeros, otherwise they differ only by one.
2. **Run Distribution Property**. In one period of a pseudorandom sequence, the frequency of runs of length k is $\frac{1}{2^k}$. The numbers of the same length one run and zero run are the same.
3. **Ideal Autocorrelation Property**. The autocorrelation function $AC(k)$ has two values for a period. Explicitly:

$$AC(k) = \frac{1}{p}\sum_{i=1}^{p} s_i s_{i+k} = \begin{cases} 1 & for\ k = np \\ \frac{-1}{p} & otherwise \end{cases}$$

where 0's of the sequence are replace by 1's and 1's by -1's, $s_i s_j$ denote the multiplication of two bits s_i and s_j.

According to Golomb's postulates (1) and (2), the ideal values of the N's of the Monobit test and the Run test should be those listed in the 4th column in Table 1.

1. **Monobit test analysis**: Let $\epsilon = \epsilon_1 \epsilon_2 \cdots \epsilon_n$ be an one and zero bit sequence where n is the length of the bit string. Denote $X_i = 2\epsilon_i - 1$, then $S_n = X_1 + X_2 + \cdots X_n = 2(\epsilon_1 + \epsilon_2 + \cdots + \epsilon_n) - n$. If ϵ is a sequence of independent identically distributed Bernoulli random variables, then[5]
$$\frac{S_n}{\sqrt{n}} \sim N(0,1)$$
where $N(0,1)$ is a standard normal distribution.
The confident interval of $S'_n = \epsilon_1 + \epsilon_2 + \cdots \epsilon_n$ with significant level α is given by
$$\frac{n}{2} - \frac{\sqrt{n}}{2} Z_{\frac{\alpha}{2}} \leq S'_n \leq \frac{n}{2} + \frac{\sqrt{n}}{2} Z_{\frac{\alpha}{2}}$$
where $Z_{\frac{\alpha}{2}}$ (Matlab command *norminv*$(1-\alpha/2)$) is the inverse of the normal cumulative distribution function. In the case $n = 20,000$ and $\alpha = 0.0001$, the calculated result is given in the second column in Table 1 which is the same as the required interval given by the FIPS 140-2 test.
2. **Run test analysis**. Pick up the runs of length k from an one and zero bitstream and construct a new bit stream. Replace each one run of length k by 1, and zero run of length k by 0. Then we obtain an one and zero bit sequence $\epsilon' = \epsilon'_1 \epsilon'_2 \cdots \epsilon'_{n'}$ where n' is the length of the new bit string. Assume ϵ' is a sequence of independent identically distributed Bernoulli random variables, then similar to the analysis in the case of the Monobit test, we obtain
$$\frac{S_{n'}}{\sqrt{n'}} \sim N(0,1)$$
The confident interval of $S'_{n'} = \epsilon'_1 + \epsilon'_2 + \cdots \epsilon'_{n'}$ with significant level α is given by
$$\frac{n'}{2} - \frac{\sqrt{n'}}{2} Z_{\frac{\alpha}{2}} \leq S'_{n'} \leq \frac{n'}{2} + \frac{\sqrt{n'}}{2} Z_{\frac{\alpha}{2}}$$
For an ideal 20,000 one and zero bit pseudorandom stream, the length n' of a bit sequence ϵ' generated via the runs of length k should equal to $10000/2^k$. Let $\alpha = 1.6 \times 10^{-7}$, the calculated confident intervals are listed in the second column in Table 1 which are almost the same as the required intervals given by the FIPS 140-2 test.

3. **Poker test analysis**. Assume the the 4-bit segments are distributed independently and identically. Then the statistic quality

$$N = \frac{16}{5000}\sum_{i=1}^{16} f(i)^2 - 5000$$
$$= \sum_{i=1}^{16} \frac{5000}{1/16}(\frac{f(i)}{5000} - \frac{1}{16})^2$$

obeys χ^2 distribution. Hence the confident interval of the statistic quality of N with significant level α is given by

$$\chi^2_{1-\frac{\alpha}{2}}(15) \le N \le \chi^2_{\frac{\alpha}{2}}(15),$$

where $\chi^2_\alpha(15)$ (Matlab command chi2inv(α,15)) is the inverse of the χ^2 cumulative distribution function with free degree 15.

Let $\alpha = 0.0002$. The calculated confirmation interval is given in Table 1 which is similar to the one given by the FIPS 140-2 test.

3 New Chaotic Map and Pseudorandom Number Generator

we consider a novel chaotic map (NCM), whose prototype is the three-dimensional Lorenz chaotic map [15].

$$\begin{cases} X(n+1) = k_1X(n)Y(n) - k_2Z(n) - k_3X(n) \\ Y(n+1) = k_4X(n) - k_5Y(n) \\ Z(n+1) = k_6Y(n) - k_7Z(n) \end{cases}$$

where

$$k_1 = 1 - 10^{-6}, k_2 = 1 + 10^{-6}, k_3 = 2 \times 10^{-6},$$
$$k_4 = 1 + 10^{-6}, k_5 = 3 \times 10^{-6}, k_6 = 1 - 10^{-6}, k_7 = 10^{-6}.$$

The Lyapunov exponents of the NCM are $[\lambda_1, \lambda_2, \lambda_3] = [+0.0824, 0, -0.0824]$. If select an initial condition $[X_0, Y_0, Z_0] = [0.5\ 0.5\ \text{-}1]$, the numerical simulations of the orbits of the NCM display are given in Fig. 1. Observe that the dynamic patterns are similar to those of the 3D Lorenz map[15].

Let

$$K_n = \sqrt{3}X(n) + \sqrt{5}Y(n) + \sqrt{2}Z(n), n = 1, 2, \cdots, N;$$
$$Min(K) = \min_{1\le n\le N} K_n, Max(K) = \max_{1\le n\le N} K_n.$$

Define a transformation T by

$$T(K_n) = mod\left(round\left(\frac{255\sqrt{2}\times 10^5(K_n - Min(K))}{Max(K) - Min(K)}\right), 256\right), n = 1, 2, \cdots, N.$$

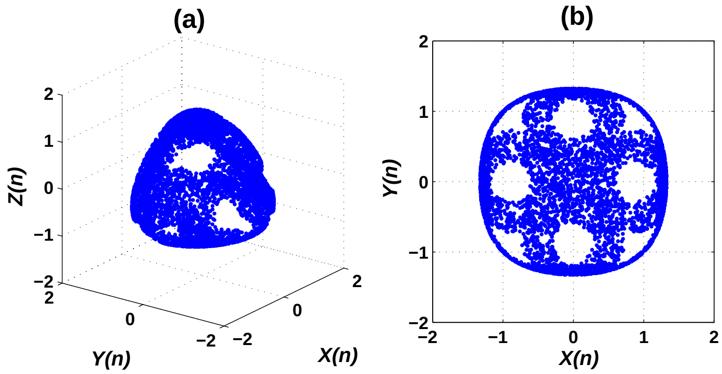

Fig. 1. Orbits of the first 5000 iterations: (a) $X(n), Y(n), Z(n)$, and (b) $X(n)$ and $Y(n)$.

Transferring $T(K_n)$ into binary codes, we obtain a binary sequence

$$s(k) = binary(T(K_n)), n = 1, 2, \cdots, N. \tag{2}$$

Hence, we construct a chaos-based pseudorandom number generator (CPNG).

4 FIPS 140-2 test

The RC4 was designed by Ron Rivest of RSA Security in 1987, and widely used in popular protocols such as Secure Sockets. Now we use the FIPS 140-2 test to test the 1000 keystreams randomly generated by the RC4, and the 1000 keystreams generated by the CPNG with an initial condition $[X(0), Y(0), Z(0)]$ = [0.5, 0.5, -1] perturbed randomly in the range $|\epsilon| \in [10^{-16}, 10^{-4}]$. The results are shown in Table 2. It follows that the statistical properties of the randomness of the sequences generated via the CPNG and the RC4 do not have significant differences.

Matlab commands for implement the RC4 algorithms are listed as follows.

```
L=8; K=randint(1,2^L,[0 2^L-1]);S=[0:2^L-1]; j=0;
for i=1:2^L
j=mod(j+S(i)+K(i),2^L);
Sk=S(j+1); S(j+1)=S(i); S(i)=Sk;
end
l=1; C=zeros(1,20000/8+10); j=0;i=0; k=1;
```

```
for l=1:20000/8+10; i=mod(i+1,2^L); j=mod(j+S(i+1),2^L);
Sk=S(j+1); S(j+1)=S(i+1); S(i+1)=Sk;
C(k)=S(mod(S(j+1)+S(i+1),2^L)+1);
k=k+1;
end
```

Table 2. The confident intervals of the FIPS 140-2 tested values of 1000 key streams generated by the RC4 and the CPNG respectively. The significant level. $\alpha = 0.00001$

Test item	bits $\{0,1\}$	Golomb's Postulates	RC4 Confident Interval	CPNG Confident Interval
MT	0	10000	9992.2 $\sim$ 10012	9990.1 $\sim$ 10010
	1	10000	9988 $\sim$ 10008	9989.6 $\sim$ 10009
PT	–	16.01	14.408 $\sim$ 15.899	13.373 $\sim$ 13.914
LT	0	< 26	13.443 $\sim$ 13.971	13.405 $\sim$ 13.913
	1	< 26	13.340$\sim$13.872	13.328$\sim$ 13.823
LR	Run Test			
1	0	2500	2493.6 $\sim$ 2506.9	2492.0 $\sim$ 2504.9
	1	2500	2493.7 $\sim$ 2506.6	2489.9 $\sim$ 2503.3
2	0	1250	1244.9 $\sim$ 1253.8	1244.7$\sim$ 1253.9
	1	1250	1242.6 $\sim$ 1251.3	1243.6$\sim$ 1252.2
3	0	625	621.46 $\sim$ 628	622.10 $\sim$ 628.60
	1	625	622.44 $\sim$ 629.25	622.96 $\sim$ 629.31
4	0	313	310.09 $\sim$ 314.68	309.92$\sim$ 314.56
	1	313	311.27 $\sim$ 315.74	310.29$\sim$ 314.83
5	0	156	154.8 $\sim$ 158.21	154.18$\sim$157.44
	1	156	154.79 $\sim$ 158.2	154.66$\sim$ 158.14
6^+	0	156	154.29 $\sim$ 157.64	155.32$\sim$ 158.56
	1	156	154.54 $\sim$ 157.93	155.28 $\sim$158.67

5 Concluding Remarks

Based on Golomb's postulates for the randomness of pure pseudorandom sequences, this paper analyzes the required intervals of the statistic quantities of three tests given in the FIPS 140-2. The results show that the required intervals for different tests do not have the same significant levels.

This study introduces a perturbed 3D Lorenze discrete map. The Lyapunov exponents and the dynamic orbits of the map are both similar to those of the 3D Lorenz map.

This paper constructs a chaos-based PRNG which has 7 key parameters. This feature of the PRNG may make it have large key space. Comparing the results of the FIPS 140-2 test for the RC4 PRNG and the chaos-based PRNG shows that statistical properties of the randomness of the sequences generated via the PRNG and the RC4 PRNG do not have significant differences.

The results confirm once again that suitable designed chaos-based PRNGs may generate sound random sequences, in particular for a replacement for the one-time pad system[9]. Further research along this line is promising.

Acknowledgements

L. Min would like to thank Professor Leon O. Chua at the UB Berkeley for directing him to study the fascinating chaos field. This work is jointly supported by the NNSF of China (Nos. 61074192, 61170037).

References

1.K. Binder, and D. W. Heermann, *Monte Carlo Simulation in Statistical Physics: An Introduction* (4th edition). 2002. Springer.
2.N. Ferguson, B. Schneier, and T. Kohno, *Cryptography Engineering: Design Principles and Practical Applications*, 2010. Wiley Publishing.
3.Wegenkittl S. Gambling tests for pseudorandom number generator, *Mathematics and Computers in Simulation*, 55: 281-288, 2001.
4.NIST. *FIPS PUB 140-2, security requirements for cryptographic modules*. 2001.
5.R. Rukhin, J. Soto, J. Nechvatal et al., *A statistical test suite for random and pseudorandom number generator for cryptographic applications*, NIST Special Publication, 2001.
6.G. Marsaglia, http://www.stat.fsu.edu/pub/diehard/, 1996 [2012-03-30].
7.E. N. Lorenz, Deterministic nonperiodic flow, *J. of Atmospheric Sciences*, 20(2): 2130–148, 1963.
8.T. Y. Li and J. A. York, Period three implies chaos,*American Mathematical Monthly*, 82(10): 481–485, 1975.
9.R. A. J. Maatthews, On the derivation of a chaotic encryption algorithm, *Cryptologia*, XIII(1): 29–42, 1989.
10.T. Stojanovski and L. Kocarev01, Choas-based random number generators-part I: analysis, *IEEE Transaction on Circuitts and Systems-I: Fundamental Theory and Applications*, 48(3): 281–288, 2001.
11.L. Gámez-Guzmán, C. Cruz-Hernández, R.M. Lérrez, and E.E. Garacía-Guerrero, Synchronization of Chuas circuits with multi-scroll attractors Application to communication, *Commum Nonlinear Sci Numer Simulat*, 14: 2765–2775, 2009.
12.C. Li, S. Li, G. Alvarez et al., Cryptanalysis of a chaotic block cipher with external key and its improved version, *Chaos Solitons & Fractals*, 37: 299–307, 2008.
13.X. Yu, L. Min, and T. Chen. Chaos criterion on some quadric polynomial maps and design for chaotic pseudorandom number generator.*In Proc. of the 2011 Sewventh Int. Conf. on Nutural Computation*(26-28 July 2011, Shaghai, China), Vol.3: 1399–1402, 2011.
14.S. W. Golomb. *Shift Register Sequences*. Revised edition, CA: Aegean Park, 1982. Laguna Hills.
15.J. C. Sprott, *Chaos and Time-Sries Analysis*, page 427, Oxford. 2003. Oxford University Press.

Chaotic Modeling and Simulation (CMSIM) 2: 281–288, 2013

Chaotic behavior of the closed loop thermosyphon model with memory effects

Justine Yasappan, Ángela Jiménez-Casas[1], and Mario Castro[2]

[1] Grupo de Dinámica No Lineal (DNL), Escuela Técnica Superior de Ingeniería (ICAI), Universidad Pontificia Comillas, Madrid E-28015, Spain
(E-mails: `justemmasj@gmail.com`, `ajimenez@dmc.icai.upcomillas.es`)

[2] ICAI, Grupo Interdisciplinar de Sistemas Complejos (GISC) and DNL, Universidad Pontificia Comillas, Madrid E-28015, Spain
(E-mail: `marioc@upcomillas.es`)

Abstract. This paper presents the motion of a viscoelastic fluid in the interior of a closed loop thermosyphon. A viscoelastic fluid described by the Maxwell constitutive equation is considered for the study. This kind of fluids present elastic-like behaviors and memory effects. Numerical experiments are performed in order to describe the chaotic behavior of the solution for different ranges of the relevant parameters by using the inertial manifold for this system proved in [1]. This work comes to verify the complex nature of the behavior of viscoelastic fluids extending the result in [2] when we consider a given heat flux instead of Newton's linear cooling law.

Keywords: Thermosyphon, Viscoelastic fluid, Asymptotic behavior, Numerical analysis.

1 Introduction

Chaos in fluids subject to temperature gradients has been the subject of intense work for its applications in the field of engineering or atmospheric sciences. A thermosyphon is a device composed of a closed loop *pipe* containing a fluid whose motion is driven by the effect of several actions such as gravity and natural convection [3–5]. The flow inside the loop is driven by an energetic balance between thermal energy and mechanical energy. The interest on this system comes both from engineering and as a *toy* model of natural convection (for instance, to understand the origin of chaos in atmospheric systems). The theoretical results of the behavior of viscoelastic fluids of this model has been proved in [1] but in this work we explore it numerically.

As viscoelasticity is, in general, strongly dependent on the material composition and working regime, here we will approach this problem by studying the most essential feature of viscoelastic fluids: memory effects. To this aim we restrict ourselves to the study of the so-called Maxwell model [6]. In this

Received: 4 April 2012 / Accepted: 14 October 2012

ISSN 2241-0503

model, both Newton's law of viscosity and Hooke's law of elasticity are generalized and complemented through an evolution equation for the stress tensor, σ. The stress tensor comes into play in the equation for the conservation of momentum:

$$\rho\left(\frac{\partial \mathbf{v}}{\partial t}+\mathbf{v}\cdot\nabla\mathbf{v}\right)=-\nabla p+\nabla\cdot\sigma \tag{1}$$

For a Maxwellian fluid, the stress tensor takes the form:

$$\frac{\mu}{E}\frac{\partial\sigma}{\partial t}+\sigma=\mu\dot{\gamma} \tag{2}$$

where μ is the fluid viscosity, E the Young's modulus and $\dot{\gamma}$ the shear strain rate (or rate at which the fluid deforms). Under stationary flow, the equation (2) reduces to Newton's law, and consequently, the equation (1) reduces to the celebrated Navier-Stokes equation. On the contrary, for short times, when *impulsive* behavior from rest can be expected, equation (2) reduces to Hooke's law of elasticity.

The derivation of the thermosyphon equations of motion is similar to that in [3–5]. The simplest way to incorporate equation (2) into equation (1) is by differentiating equation (1) with respect to time and replacing the resulting time derivative of σ with equation (2). This way to incorporate the constitutive equation allows to reduce the number of unknowns (we remove σ from the system of equations) at the cost of increasing the order of the time derivatives to second order. The resulting second order equation is then averaged along the loop section (as in Ref.[3]). Finally, after adimensionalizing the variables (to reduce the number of free parameters) we arrive at the main system of equations

$$\begin{cases}\varepsilon\dfrac{d^2v}{dt^2}+\dfrac{dv}{dt}+G(v)v=\oint Tf, & v(0)=v_0,\, \frac{dv}{dt}(0)=w_0\\[2mm] \dfrac{\partial T}{\partial t}+v\dfrac{\partial T}{\partial x} = h(x)+\nu\frac{\partial^2 T}{\partial x^2}, & T(0,x)=T_0(x)\end{cases} \tag{3}$$

where $v(t)$ is the velocity, $T(t,x)$ is the distribution of the temperature of the viscoelastic fluid in the loop, ν is the temperature diffusion coefficient, $G(v)$ is the friction law at the inner wall of the loop, the function f is the geometry of the loop and the distribution of gravitational forces, $h(x)$ is the general heat flux and ε is the viscoelastic parameter, which is the dimensionless version of the viscoelastic time, $t_V=\mu/E$. Roughly speaking, it gives the time scale in which the transition from elastic to fluid-like occurs in the fluid. We consider G and h are given continuous functions, such that $G(v)\geq G_0>0$, and $h(v)\geq h_0>0$, for G_0 and h_0 positive constants. Finally, for physical consistency, it is important to note that all functions considered must be 1-periodic with respect to the spatial variable.

2 Inertial manifold: Finite dimensional asymptotic behavior

In this section we summarize the main results related to the finite dimensional asymptotic behavior of the system of equations (3) as proved in [1]. The existence and uniqueness of the solutions of (3) was proved in [1] following the techniques used in [2]. The main idea in [2] is that we rewrite our main equations (3) in terms of the Fourier expansions of each function and observing the dynamics of each Fourier mode, where $h, f \in \dot{L}^2_{per}(0,1)$ are given by the following Fourier expansions:

$$h(x) = \sum_{k \in D} b_k e^{2\pi kix}, f(x) = \sum_{k \in D} c_k e^{2\pi kix}$$

with $D = D - \{0\}$ while $T_0 \in \dot{H}^1_{per}(0,1)$ is given by

$$T_0(x) = \sum_{k \in D} a_{k0} e^{2\pi kix}$$

and $T(t,x) \in \dot{H}^1_{per}(0,1)$ is given by

$$T(t,x) = \sum_{k \in D} a_k(t) e^{2\pi kix}$$

where

$$\dot{L}^2_{per}(0,1) = \{u \in L^2_{loc}(I\!R), u(x+1) = u(x) a.e., \oint u = 0\}, \dot{H}^m_{per}(0,1) = H^m_{loc}(I\!R) \cap \dot{L}^2_{per}(0,1). \quad (4)$$

The coefficients $a_k(t)$ verify the equation:

$$\dot{a_k}(t) + (2\pi kvi + 4\nu\pi^2 k^2) a_k(t) = b_k, \quad a_k(0) = a_{k0}, \quad k \in D.$$

Here, we assume that $h \in \dot{H}^m_{per}$ with

$$h(x) = \sum_{k \in K} b_k e^{2\pi kix}$$

where $b_k \neq 0$, for every $k \in K \subset D$ with $0 \notin K$, since $\oint h = 0$. We denote by V_m the closure of the subspace of $\dot{H}^m_{per}$ generated by $\{e^{2\pi kix}, k \in K\}$. If $b_k = 0$ then the kth mode for the temperature is dumped out exponentially and therefore the space V_m attracts the dynamics for the temperature. Moreover if K is a finite set, the dimension of $\mathcal{M}$ is $|K| + 2$, where $|K|$ is the number of elements in K.

Under the above hypotheses we assume that

$$f(x) = \sum_{k \in J} c_k e^{2\pi kix}$$

with $c_k \neq 0$ for every $k \in J \subset D$. Then on the inertial manifold we have:

$$\oint (T \cdot f) = \sum_{k \in K} a_k(t) \bar{c_k} = \sum_{k \in K \cap J} a_k(t) \bar{c_k}.$$

Therefore the evolution of velocity v, and acceleration w depends only on the coefficients of T which belong to the set $K \cap J$. From [1], using similar techniques as in [7,8] we will reduce the asymptotic behavior of the initial system (3) to the dynamics of the reduced explicit nonlinear system of ODE's (5) where we consider the relevant modes of temperature $a_k, k \in K \cap J$.

$$\begin{cases} \dfrac{dw}{dt} + \dfrac{1}{\varepsilon} w + \dfrac{1}{\varepsilon} G(v)v & = \dfrac{1}{\varepsilon} \displaystyle\sum_{k \in K \cap J} a_k(t) \bar{c_k} \;\; w(0) = w_0 \\ \frac{dv}{dt} & = w, \qquad\qquad v(0) = v_0 \\ \dot{a_k}(t) + (2\pi k v i + 4\nu\pi^2 k^2) a_k(t) & = b_k, \qquad\qquad a_k(0) = a_{k0}, \quad k \in K \cap J. \end{cases} \tag{5}$$

Note that the set $K \cap J$ can be much smaller than the set K and therefore the reduced subsystem may possess far fewer degrees of freedom than the system on the inertial manifold. Also note that it may be the case that K and J are infinite sets, but their intersection is finite. For instance, for a circular circuit we have $f(x) \sim a\sin(x) + b\cos(x)$, i.e., $J = \{\pm 1\}$ and then $K \cap J$ is either $\{\pm 1\}$ or the empty set.

3 Numerical experiments

3.1 Preliminary mathematical approximation

In this section, we integrate the system of ODEs (5), where we consider only the coefficients of temperature $a_k(t)$ with $k \in K \cap J$ (relevant modes). Thus,

$$\begin{cases} \frac{dw}{dt} + \frac{w}{\varepsilon} + \frac{G(v)v(t)}{\varepsilon} = \frac{2}{\varepsilon} Real \left(\sum_{k \in K \cap J} a_k(t) \bar{c_k} \right) \; w(0) = w_0 \\ \frac{dv}{dt} = w, \qquad v(0) = v_0 \\ \dot{a}_k(t) + a_k(t)(2\pi k i v + \nu 4\pi^2 k^2) = b_k, \qquad a_k(0) = a_{k0}. \end{cases}$$

We impose that all the physical observable as real functions, then $a_{-k} = \bar{a}_k$, $b_{-k} = \bar{b}_k$ and $c_{-k} = \bar{c}_k$. In particular, we consider a thermosyphon with a circular geometry, so $J = \{\pm 1\}$ and $K \cap J = \{\pm 1\}$. Consequently, we can take $k = 1$ and omit the equation for $k = -1$ (is conjugated of the equation for $k = 1$). Also in order to reduce the number of free parameters we make the following change of variables $a_1 c_{-1} \to a_1$.

$$\begin{cases} \frac{dw}{dt} = \frac{2a_1}{\varepsilon} - \frac{w}{\varepsilon} - \frac{G(v)v(t)}{\varepsilon}, \qquad w(0) = w_0 \\ \frac{dv}{dt} = w, \qquad v(0) = v_0 \\ \dot{a}_1(t) + a_1(t)(2\pi i v + \nu 4\pi^2) = b_1, \; a_1(0) = a_{10}. \end{cases}$$

We denote the real and imaginary parts of the $a_1(t)$ (the Fourier mode of the temperature) in the following way:

$$a_1(t) = a^1(t) + i a^2(t), \tag{6}$$

$$b_1 = A + iB \tag{7}$$

with $A \in I\!R, B \in I\!R$. Thus we obtain the corresponding nonlinear system of equations where we need to make explicit choice of the constitutive laws for both the fluid-mechanical and thermal properties for this model:

$$\begin{cases} \frac{dw}{dt} = \frac{2a^1}{\varepsilon} - \frac{w}{\varepsilon} - \frac{G(v)v(t)}{\varepsilon}, \;\; w(0) = 0 \\ \dot{v} = w, \qquad v(0) = 0 \\ \dot{a}^1 = A - \nu 4\pi^2 a^1 + v 2\pi a^2, \; a^1(0) = 1 \\ \dot{a}^2 = B - \nu 4\pi^2 a^2 - v 2\pi a^1 \;\; a^2(0) = 1. \end{cases} \tag{8}$$

Hereafter, we present the numerical experiments of equations (5) that are carried out for the resolution of the nonlinear system of ODEs using the fourth-order explicit Runge-Kutta method. The summary of our results is presented in the figures of section 3.2. In particular, we present the plots for velocity, acceleration and (the fourier transform of the) temperature of this system. All the variables and equations that we deal with are adimensional. As the system is multidimensional, we present the results in temporal graphs (variables vs time) and phase-space graphs (two physical variables plot against each other).

In all cases, we take the same mathematical form for the friction law, $G(v) = (|v|+10^{-4})$, as used in the previous works (see, for instance, [2,7,8]), for a similar model of thermosyphon with a non-viscoelastic fluid with one component. The rationale behind this equation is that it interpolates between a constant (low Reynolds number laminar flow) and a linear (highly turbulent flow) function of the velocity. Likewise, A and B, which refer to the position-dependant (x) heat flux inside the loop will be used as tuning parameters. We will assume $A = 0$ in order to simplify, as different values of A only changes the *phase* the periodic function $h(x)$. We will also fix $B = 50$ the heat flux parameter, $\nu = 0.002$ the diffusion coefficient and observe the evolution of the variables. The initial conditions are fixed to $w(0) = 0, v(0) = 0, a^1(0) = 1, a^2(0) = 1$. Finally, we have also studied the behavior of the system of equations by keeping ε as a tuning parameter ranging from 1 to 10, to observe the response of the system under the effects of viscoelasticity.

3.2 The chaotic behavior of the model

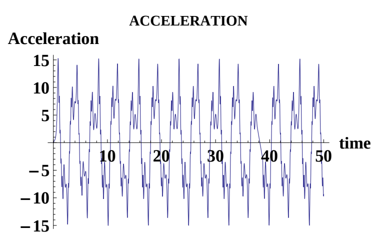

Fig. 1. The time evolution of the acceleration, $w(t)$, with $\varepsilon = 1$, $A = 0$, $B = 50$, $\nu = 0.002$ and $G(v) = (|v| + 10^{-4})$

The impact of ε on the system has been keenly observed for various parameters. In general (see below), as the viscoelastic component ε increases, the chaotic behavior of the system also increases. In Fig. 1 we show the time evolution of the acceleration, $w(t)$, for the viscoelastic parameter $\varepsilon = 1$. The acceleration $w(t)$ ranges from -15 to 15. The plot is chaotic but, although this is more apparent in the acceleration plot than in the velocity one. This is reasonable as the velocity is the time integral of the acceleration, namely, the velocity curve looks smoother than that of acceleration (therefore the chaotic behavior is not so apparent).

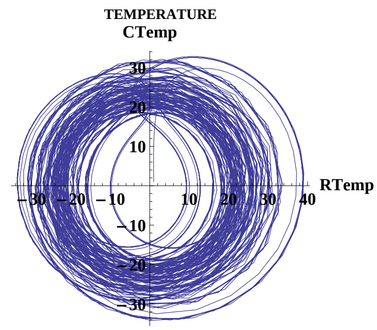

Fig. 2. Phase-plane of the real and imaginary parts of Fourier transform of the temperature for $\varepsilon = 1$, $A = 0$, $B = 50$, $\nu = 0.002$ and $G(v) = (|v| + 10^{-4})$.

In Fig. 2 we show the phase-diagram for the real $a^1(t)$ and imaginary $a^2(t)$ parts of the Fourier transform of the temperature. As expected, the trajectory in this phase-plane moves inwards and outwards. This plot illustrates the underlying complex dynamics of the attractor as a two dimensional projection.

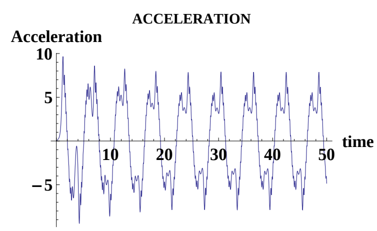

Fig. 3. The time evolution of the acceleration, $w(t)$, with $\varepsilon = 3$, $A = 0$, $B = 50$, $\nu = 0.002$ and $G(v) = (|v| + 10^{-4})$

In the second set of numerical experiments we increase the value of viscoelastic component to $\varepsilon = 3$. As the value of viscoelastic component ε is relatively higher than the previous experiment i.e., $(\varepsilon = 3)$ the system tends to be more chaotic than the previous experiment. The acceleration $w(t)$ ranges from -10 to 10. The deviation in the progress of acceleration is maintained till the end of the progress. Apparently, the behavior is also chaotic but this chaos seems to be embedded in larger timescale oscillations. Interestingly, the number of oscillations is reduced from 15 to 9, Fig. 3 showing less number of peaks than the first case. This is a reflection of the memory effects associated to the viscoelastic of the fluid. Thus, as ε plays the role of a time scale, the larger this value the longer are the memory effects (in our case exposed through the period of the underlying oscillations).

For $\varepsilon = 10$ (Fig. 4), the system still exhibits a chaotic progression, with the acceleration ranging from -4 to 4 and with even an underlying longer-period oscillations compared to the previous experiments.

Finally, in Fig. 5 we show the phase-diagram for $a^1(t)$ and $a^2(t)$. Again, as expected, the trajectory in this phase-plane moves inwards and outwards.

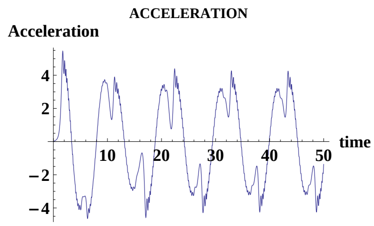

Fig. 4. The time evolution of the acceleration, $w(t)$, with $\varepsilon = 10$, $A = 0$, $B = 50$, $\nu = 0.002$ and $G(v) = (|v| + 10^{-4})$

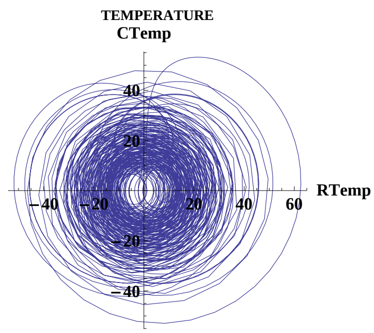

Fig. 5. Phase-plane of the real and imaginary parts of Fourier transform of the temperature for $\varepsilon = 10$, $A = 0$, $B = 50$, $\nu = 0.002$ and $G(v) = (|v| + 10^{-4})$.

This plot illustrates the underlying complex dynamics of the attractor of a two dimensional projection.

In summary, larger values of the viscoelastic parameters ε, results in sustained chaotic behaviors overlapped with an (almost) periodic behavior whose period scales with the numerical value of ε. The dynamics becomes more complex and is characterized in all cases by periods of chaos and of violent oscillations, giving an idea of the complexity of the solutions of the system under these variables due to memory effects.

4 Conclusion

The physical and mathematical implications of the resulting system of ODEs which describe the dynamics at the inertial manifold is analyzed numerically. The role of the parameter ε which contains the viscoelastic information of the fluid was treated with special attention. We studied the asymptotic behavior of the system for different values of ε the coefficient of viscoelasticity. We can conclude that for larger values of ε the system behaves more chaotic. Physically, this induction of chaotic behaviors is related to the memory effects inherent to viscoelastic fluids. Thus, in the same way as delayed equations are known to produce chaos, even in the simplest situations, viscoelasticity produces the same kind of transition.

Acknowledgements

This work has been partially supported by Projects MTM2009-07540, GR58/08 Grupo 920894 BSCH-UCM, Grupo de Investigación CADEDIF and FIS2009-12964-C05-03, SPAIN.

References

1. A. Jiménez-Casas, Mario Castro, and Justine Yasappan. Finite-dimensional behavior in a thermosyphon with a viscoelastic fluid. submitted, 2012.
2. Justine Yasappan, A. Jiménez-Casas, and Mario Castro. Asymptotic behavior of a viscoelastic fluid in a closed loop thermosyphon: physical derivation, asymptotic analysis and numerical experiments. submitted, 2011.
3. J.B. Keller. Periodic oscillations in a model of thermal convection. *J. Fluid Mech.*, 26:599–606, 1966.
4. P. Welander. On the oscillatory instability of a differentially heated fluid loop. *J. Fluid Mech.*, 29:17–30, 1967.
5. J.J.L. Velázquez. On the dynamics of a closed thermosyphon. *SIAM J. Appl. Math.*, 54:1561–1593, 1994.
6. F. Morrison. Understanding rheology. *Oxford University Press, USA*, 2001.
7. A. Jiménez-Casas, and A.M-L. Ovejero. Numerical analysis of a closed-loop thermosyphon including the Soret effect. *Appl. Math. Comput.*, 124:289-318, 2001.
8. A. Rodríguez-Bernal, and E.S. Van Vleck. Diffusion Induced Chaos in a Closed Loop Thermosyphon. *SIAM J. Appl Math.*, 58:1072-1093, 1998.

Analysis of the bifurcating orbits on the route to chaos in confined thermal convection

Diego Angeli[1], Arturo Pagano[2],
Mauro A. Corticelli[1], Alberto Fichera[2], and Giovanni S. Barozzi[1]

[1] University of Modena and Reggio Emilia, Department of Mechanical and Civil Engineering, Via Vignolese, 905, I-41125 Modena, Italy
(E-mail: diego.angeli@unimore.it)
[2] University of Catania, Department of Industrial and Mechanical Engineering Viale Andrea Doria, 6, I-95125 Catania, Italy
(E-mail: apagano@diim.unict.it)

Abstract. Bifurcating thermal convection flows arising from a horizontal cylinder centred in a square-sectioned enclosure are studied numerically, with the aim of achieving a more detailed description of the sequence of transitions leading to the onset of chaos, and obtaining a more precise estimate of the critical values of the main system parameter, the Rayleigh number Ra. Only a value of the geometric aspect ratio A of the system is considered, namely $A = 2.5$, for which a period-doubling cascade was previously observed. Results give evidence of new and interesting features in the route to chaos, such as a window of quasiperiodic flow and the detection of high-order period orbits.
Keywords: Thermal convection, period-doubling cascade, quasi-periodicity, deterministic chaos.

1 Introduction

Buoyancy-induced flows in enclosures represents one of the most complete multi-scale coupled non-linear fluid flow problems. Their primary importance in the field of the study of bifurcations and chaos is due to the fact that they represent passive systems on which bifurcative dynamics easily show up, and, eventually, lead to relevant observations on the relationship between the onset of chaos and the transition from laminar to turbulent flow.

Many works have been carried out on the non-linear dynamics of thermal convection in basic enclosure configurations, such as the rectangular enclosures heated from below (the Rayleigh-Bénard problem) and from the side [1,2] (the "vertical enclosure" case), and, more recently, the horizontal annulus between two coaxial cylinders [3]. Fewer works dealt with more complex geometrical and thermal configurations [4–6]. Nevertheless, from a theoretical and practical standpoint, the interest in this topic is growing continuously.

Received: 17 April 2012 / Accepted: 25 September 2012

ISSN 2241-0503

The physical system considered in the present study is the cavity formed by an infinite square parallelepiped with a centrally placed cylindrical heating source. The system is approximated to its 2D transversal square section containing a circular heat source, as sketched in Fig. 1. The temperature of both enclosure and cylinder is assumed as uniform, the cylindrical surface being hotter than the cavity walls. Thus, the leading parameter of the problem is the Rayleigh number Ra, based on the gap width H, expressing the temperature difference in dimensionless terms. Another fundamental parameter is the Prandtl number, fixed for this study at a value $Pr = 0.7$, representative of air at environmental conditions.

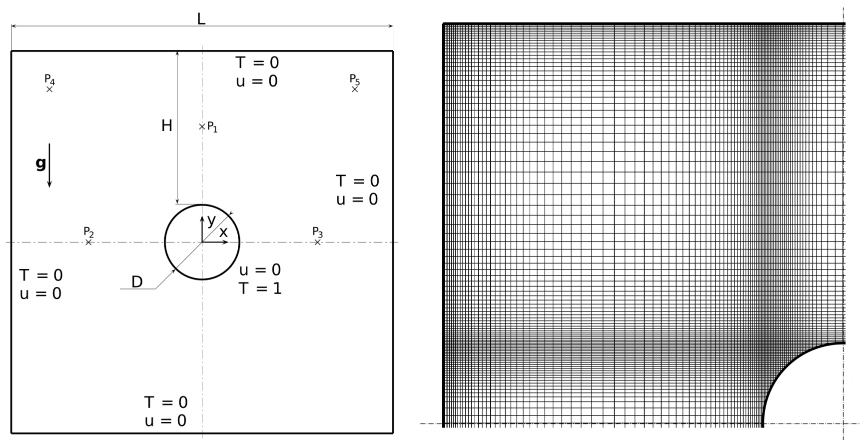

Fig. 1. Left: schematic of the system under consideration; (×) symbols indicate locations of the sampling points. Right: quadrant of the computational grid.

From the standpoint of thermofluids, the convective system in Fig. 1 is particularly interesting, since, due to the curvature of the cylindrical differentially heated surfaces, its phenomenology encompasses the features of both the Rayleigh-Bénard and the vertical enclosure cases. As soon as a temperature difference is imposed between the cylinder and the enclosure, fluid motion ensues immediately in the vicinity of the horizontal midplane, where the cylindrical walls are substantially vertical. On the other hand, the fluid in the top part of the enclosure is subject to an unstable vertical gradient, as in the Rayleigh-Bénard problem, while vertical boundary layers are invariably forming at the enclosure sidewalls. The combination of these situations in a single problem produces a variety of flow configurations and transition phenomena.

Previous studies [5,6] already unfolded different scenarios on the route to chaos of the system considered here, depending on its aspect ratio $A = L/H$. Accurate numerical investigations carried out for two A-values, $A = 2.5$ and $A = 5$, revealed the existence of a period-doubling scenario following a Hopf bifurcation for $A = 2.5$, and a transition to chaos via a symmetry-breaking pattern followed by a blue-sky bifurcation for $A = 5$ [6].

The aim of the present work is to achieve a deeper insight into the series of bifurcations for the case $A = 2.5$, in virtue of a wider set of numerical simulations performed by refining the step of the bifurcation parameter Ra. Particular attention has been devoted to the analysis of the stretching and folding attitudes of specific regions of the system attractor in proximity of the Ra-values corresponding to the period doubling bifurcation points, and in the chaotic range.

Numerical predictions are carried out by means of a specifically developed finite-volume code. Successive bifurcations of the low-Ra fixed point solution are followed for increasing Ra. To this aim, time series of the state variables (velocity components and temperature), are extracted in 5 locations represented in Fig. 1 by points P1 to P5. Nonlinear dynamical features are described by means of phase-space representations, power spectra of the computed time series, and of Poincaré maps.

2 Problem statement and methods

The problem is stated in terms of the incompressible Navier-Stokes formulation, under the Boussinesq approximation. The governing equations (continuity, momentum and energy) are tackled in their non-dimensional form:

$$\nabla \cdot \mathbf{u} = \mathbf{0} \tag{1}$$

$$\frac{\partial \mathbf{u}}{\partial t} + \mathbf{u} \cdot \nabla \mathbf{u} = -\nabla p + \frac{Pr^{1/2}}{Ra^{1/2}} \nabla^2 \mathbf{u} + T\hat{\mathbf{g}} \tag{2}$$

$$\frac{\partial T}{\partial t} + \mathbf{u} \cdot \nabla T = \frac{1}{(RaPr)^{1/2}} \nabla^2 T \tag{3}$$

where t, $\mathbf{u}$, p and T represent the dimensionless time, velocity vector, pressure and temperature, respectively, and $\hat{\mathbf{g}}$ is the gravity unit vector. A value $Pr = 0.7$ is assumed for air. Boundary conditions for T and $\mathbf{u}$ are reported in Fig. 1.

Detailed descriptions of the adopted numerical techniques and of discretization choices are found in previous works [5,7]. A detail of the computational grid is shown in Fig. 1. In order to analyze the system dynamics in the vicinity of bifurcation points, Ra was increased monotonically with suitable steps, each simulation starting from the final frame of the preceeding one. All the simulations were protracted until a fixed dimensionless time span was covered, large enough for an asymptotic flow to be attained.

3 Results and discussion

In previous studies [5,6] a preliminary analysis of the system with $A = 2.5$ reported the birth of chaotic behaviours for Ra greater than $Ra = 2.0 \cdot 10^5$. In particular, power spectral density distributions, attractor representations and

Poincaré maps were used to give a clear evidence of a basic period doubling route to chaos. In particular, it was shown that the flow is characterised by two fundamental harmonics at $Ra = 1.7 \cdot 10^5$, four harmonics at $Ra = 1.8 \cdot 10^5$ and eight at $Ra = 1.9 \cdot 10^5$, whereas chaos was observed at $Ra = 2.0 \cdot 10^5$.

Given the great theoretical and practical importance of an accurate determination of the bifurcating behaviour of the flow, deeper analyses have been performed by refining the step of numerical simulation of the range of interest of the Rayleigh number. As described in the following, two main results have been obtained: (i) the identification of a window of quasiperiodic flow; (ii) the identification of three further period doublings preluding appearance of chaos.

3.1 Window of quasiperiodic flow

Several simulations performed in the range $Ra = 1.7 \div 1.9 \cdot 10^5$ have been found to be characterised by a well defined quasiperiodic behaviour. Again, the observation of this result has been performed both in the frequency domain and in the state space.

Fig. 2 reports the PSDs of the variables simulated at point P1 for the case at $Ra = 176875$, in (a) for the horizontal velocity component u, in (b) for the vertical velocity component v and in (c) for the temperature T.

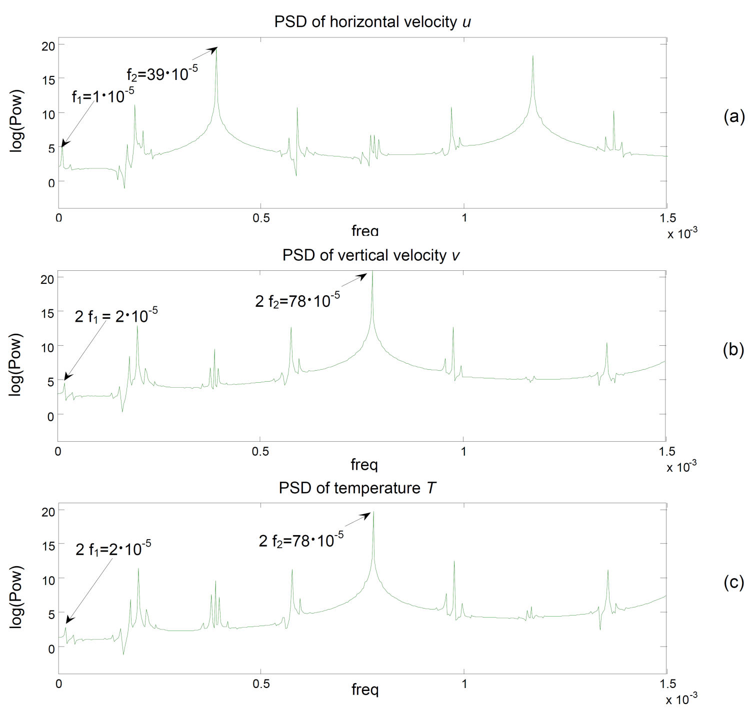

Fig. 2. PSDs of the simulated state variables at point P1 for the quasiperiodic case at $Ra = 176875$: (a) horizontal velocity u; (b) vertical velocity v; (c) temperature T.

The following interesting observations can be drawn from the analysis of the three plots of Fig. 2:

- the PSDs of v and T are mainly the same, as a consequence of the vertical character of the buoyancy-driven flow that determines the dynamics of the thermal and velocity field;
- the quasiperiodic behaviour finds a clear expression in the excitation of two independent frequencies, reported in the figures, and of bands formed by their linear harmonic combinations;
- the two dominant frequencies of v and T, exactly double those of the horizontal velocity u, as a direct consequence of the vertical symmetry of the domain.

Fig. 3 reports the phase plots for the simulation at point P1 for the case at $Ra = 176875$, i.e. for the same quasiperiodic dynamic discussed in Fig. 2. Plot (a) reports the whole toroidal attractor, whereas plot (b) allows for a deeper observation of the narrow toroidal structure of the attractor itself. Finally, plots (c), (d) and (e) reports the Poincaré map obtained by sectioning the attractor with the planes orthogonal to each of the axis in correspondence of the mean value of respective variable in the considered observation window. From the analysis of the plots in Fig. 3 it is possible to draw a further clear proof of the existence of the quasiperiodic behaviour, manifested in the state space by the torus and in the Poincaré maps by the elliptical traces. Notice that in plot (c) two partly superimposed elliptical traces appears as a consequence of the intersection of the two branches of the torus in the chosen Poincaré plane.

It is worthy to mention that further analyses, omitted here for brevity, revealed that the quasiperiodic torus appears $Ra = 1.740 \cdot 10^5$, bifurcating from the stable limit cycle which represents the solution at $Ra = 1.735 \cdot 10^5$, while it disappears, for $Ra = 1.795 \cdot 10^5$, giving rise to the period-doubling route described in the following. Such observations contribute to shed light on the proper bifurcation path in the range $Ra = 1.740 \div 1.795 \cdot 10^5$, which therefore redefines the simple period doubling assumed in [6].

3.2 High order period doublings

A further refinement of the Ra steps of the simulation in the range $Ra = 1.9 \div 2.0 \cdot 10^5$ allowed for the determination the critical values of Ra at which higher order period doublings occur. In particular, the progressive increase from $Ra = 1.8 \cdot 10^5$, for which a period 8 limit cycle exists, it has been possible to determine the birth of the limit cycles characterised by 16, 32, 64 and even 128 periods, which anticipate the appearance of chaos.

From the analysis of the extensive simulations performed for very narrow step of Ra in the range $Ra = 1.9 \div 2.0 \cdot 10^5$, completed with the observation of the window of quasiperiodic behaviour, it has been possible to summarise the complete bifurcation path from period-2 limit cycle to chaos according to the limits reported in Tab. 3.2. There, the notation introduced in [3] is used to identify the different flow regimes.

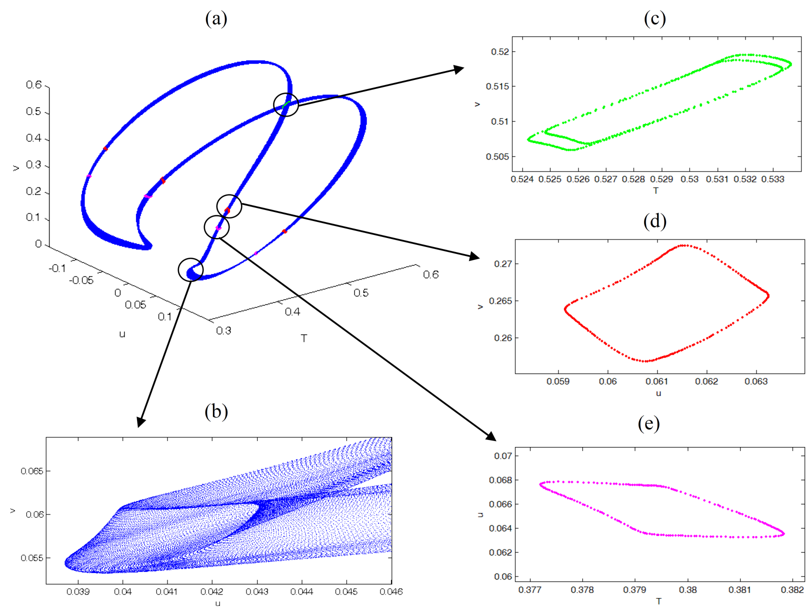

Fig. 3. Phase plots of the quasiperiodic dynamical behaviour at point P1 for $Ra = 176875$: (a) attractor in the state space T-u-v; (b) particular evidencing the structure of the narrow torus; (c), (d), (e) Poincaré maps.

	P_1	QP_2	P_2	P_4	P_8
$Ra \cdot 10^{-5}$	≤ 1.735	$1.74 \div 1.79$	$1.795 \div 1.8975$	$1.898 \div 1.9367$	$1.93675 \div 1.94730$

	P_{16}	P_{32}	P_{64}	N
$Ra \cdot 10^{-5}$	$1.94735 \div 1.9495$	$1.94955 \div 1.94985$	1.9499	> 1.95

Table 1. Sequence of flow regimes encountered and correspondent ranges of Ra.

Fig. 4 reports the Poincaré maps for some characteristic values of the Rayleigh number falling within the ranges of limit cycles of high-order period (from P_4 to P_{64}) as well as for one value in the chaotic range, $Ra = 1.9625 \cdot 10^5$. In each map it is possible to observe the existence of four clusters of points, each of which can be considered generated by the four intersections of the original P_1 limit cycle existing for $Ra \leq 1.735 \cdot 10^5$. In order to achieve a deeper detail on the phenomenon, the encircled clusters in Fig. 4 are reported in Fig. Fig. 5, where the series of doubling of each point can be better observed. As a final remark, it is possible to observe that the period doubling bifurcation path is responsible for the birth of bands in the chaotic attractor, characterised by a marked attitude to stretching and folding typical of fractal sets, as it can be deduced by the ordered distribution of the intersections in the Poincaré maps.

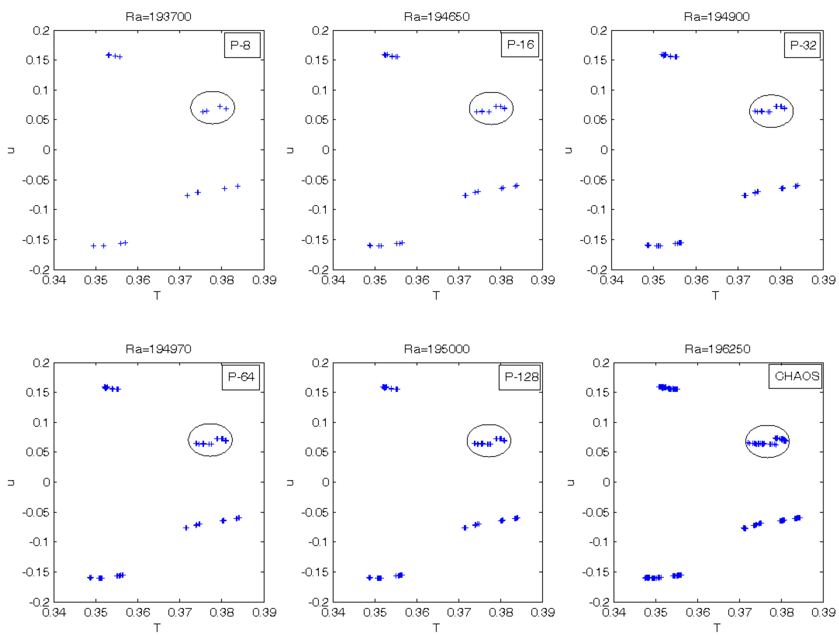

Fig. 4. Poincaré maps for characteristic Ra-values, for limit cycles of high-order period (from P_4 to P_{64}) and chaos.

4 Concluding remarks

The sequence of bifurcations leading to deterministic chaos in natural convection from a horizontal cylindrical source, centred in a square enclosure of aspect ratio $A = 2.5$, was analysed in detail by numerical means.

The set of long term simulations revealed further remarkable aspects of the route to chaos of the system, for increasing the main parameter Ra. In first instance, a window of quasiperiodic behaviour was observed over a wide range of Ra-values, originating from the first limit cycle and giving rise to the subsequent the period-doubling cascade.

Furthermore, the refinement of the parameter range allowed for the detection of additional stages in the sequence of period doublings of the system, up to the observation of a P_{64} orbit, before the final appearance of chaos.

References

1. K. T. Yang. Transitions and bifurcations in laminar buoyant flows in confined enclosures. ASME *Journal of Heat Transfer*, 110:1191–1204, 1988.
2. P. Le Quéré. Onset of unsteadiness, routes to chaos and simulations of chaotic flows in cavities heated from the side: a review of present status. In G. F. Hewitt, editor, *Proceedings of the Tenth International Heat Transfer Conference*, volume 1, pages 281–296, Brighton, UK, 1994. Hemisphere Publishing Corporation.

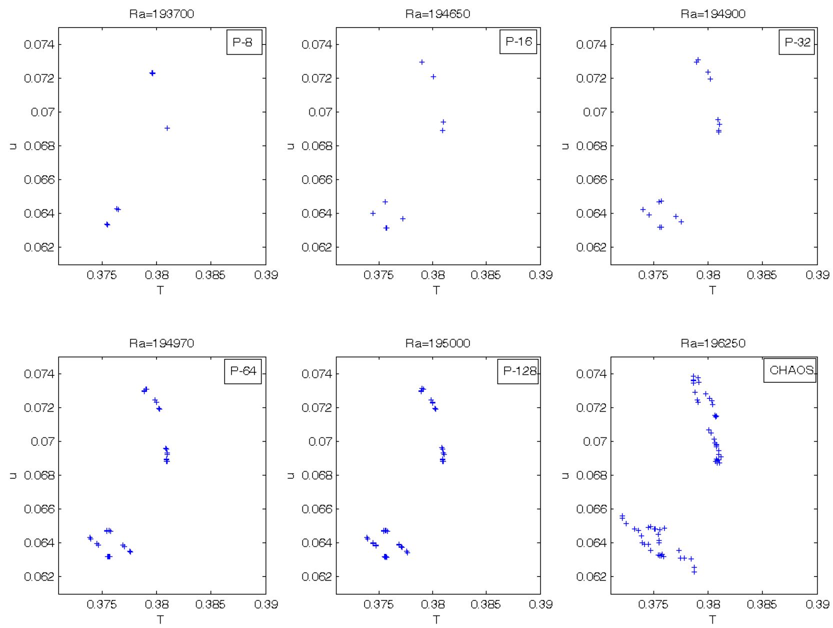

Fig. 5. Details of the encircled clusters of points in the Poincaré maps of Fig. 4.

3.D. Angeli, G. S. Barozzi, M. W. Collins, and O. M. Kamiyo. A critical review of buoyancy-induced flow transitions in horizontal annuli. *International Journal of Thermal Sciences*, 49:2231–2492, 2010.

4.G. Desrayaud and G. Lauriat. Unsteady confined buoyant plumes. *Journal of Fluid Mechanics*, 252:617–646, 1998.

5.D. Angeli, A. Pagano, M. A. Corticelli, A. Fichera, and G. S. Barozzi. Bifurcations of natural convection flows from an enclosed cylindrical heat source. *Frontiers in Heat and Mass Transfer*, 2:023003, 2011.

6.D. Angeli, A. Pagano, M.A. Corticelli, and G.S. Barozzi. Routes to chaos in confined thermal convection arising from a cylindrical heat source. *Chaotic Modeling and Simulation*, 1:61–68, 2011.

7.D. Angeli, P. Levoni, and G. S. Barozzi. Numerical predictions for stable buoyant regimes within a square cavity containing a heated horizontal cylinder. *International Journal of Heat and Mass Transfer*, 51:553–565, 2008.

Chaotic Modeling and Simulation (CMSIM) 2: 297–304, 2013

Analysis of the Triple Pendulum as a Hyperchaotic System

André E Botha[1] and Guoyuan Qi[2]

[1] Department of Physics, University of South Africa, P.O. Box 392, Pretoria 0003, South Africa
(E-mail: bothaae@unisa.ac.za)

[2] F'SATI and Department of Electrical Engineering, Tshwane University of Technology, Private Bag X680, Pretoria 0001, South Africa
(E-mail: qig@tut.ac.za)

Abstract. An analysis is made of the hyperchaotic behaviour of a triple plane pendulum. It is shown that there are only eight physically distinct equilibrium configurations for the pendulum and that the types of eigen solutions obtained, for the Jacobian matrix evaluated at each equilibrium configuration, are independent of the system parameters. A new method for extracting the periodic orbits of the system is also developed. This method makes use of least-squares minimisation and could possibly be applied to other non-linear dynamic systems. As an example of its use, four periodic orbits, two of which are numerically unstable, are found. Time series plots and Poincaré maps are constructed to investigate the periodic to hyperchaotic transition that occurs for each unstable orbit.

Keywords: Triple pendulum; hyperchaos; fixed points; periodic orbits.

1 Introduction

The present work is motivated by recent interest in studying pendulum systems for possible exploitation in various technological applications. There have been a number of experimental and theoretical investigations aimed at understanding the stability of human gait (manner of stepping) through the use of inverted pendulum models [1,2]. Experimental investigations of either simple or coupled electro-mechanically driven pendulums have been undertaken with the view of developing more precise conditions for the onset of chaos in such systems [3,4]. Also, a triple pendulum suspension system has been developed to seismically isolate optical components on the GEO 600 interferometric gravitational wave detector [5]. The latter development has allowed the detector to achieve a seismic noise sensitivity level which is well below the level from thermal noise.

Coupled pendulums with obstacles have been used to model real mechanical systems that exhibit nonlinear phenomena such as resonances, jumps between different system states, various continuous and discontinuous bifurcations, symmetry breaking and crisis bifurcations, pools of attractions, oscillatory-rotational

Received: 23 March 2012 / Accepted: 24 September 2012

ISSN 2241-0503

attractors, etc. [6–9]. In Ref. [9], for example, it has been shown that a triple pendulum model can provide insight into the real, highly-complicated dynamics of a piston connecting-rod crankshaft system.

An experimental triple pendulum has been constructed by Awrejcewicz *et al.* [10]. This pendulum has been analysed numerically and experimentally, and good agreement has been obtained between the mathematical model and the real system. In the present work, higher order effects that pertain to specific experimental systems, like [10], are neglected. For example, we have not included finer details of the frictional forces that act on the joints of the pendulum, or asymmetries in its driving mechanism. One of the motivating factors for neglecting such higher order effects is the correspondence that exists between the equations for a damped simple pendulum, driven by a constant torque, and the well-known phenomenological model of a superconducting Josephson junction [4,11]. It is thought that our somewhat simplified model of the triple pendulum could, with minor modifications, serve as a useful mechanical analogy for a series system of three resistively coupled Josephson junctions.

This paper is organised as follows. In Section 2, the basic model and equations are described. The system is linearised at its equilibria in Section 3. In Section 4 a new method is developed for finding the periodic orbits of the system, based on least-squares minimisation. Four examples of found periodic orbits are discussed, including their time series and Poincaré maps. In two of the examples interesting periodic-hyperchaotic transitions are observed. Section 5 concludes with a discussion of the main advantages and possible disadvantages of the new method.

2 Description of model and equations

The current work is a continuation of our previous work [12], in which a three-dimensional animation of a model triple plane pendulum was created by using the *Visual* module in the *Python* programming language [14]. As shown in Fig. 1, the model consists of a series of absolutely rigid bars which form the three links of the pendulum (shown in red, green and blue). Additional point-like masses are attached to the bottom of each link (shown as yellow cylindrical disks).

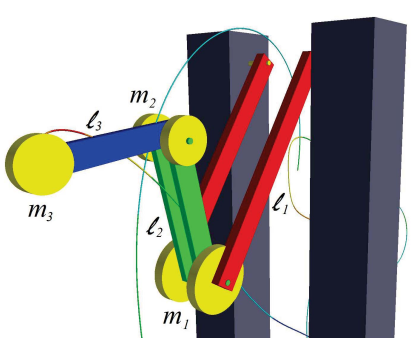

Fig. 1. Visualisation of the triple plane pendulum. The pendulum is made of rigid bars (two of length ℓ_1, two of length ℓ_2 and one of length ℓ_3) to which point-like masses may be attached (two of mass $\frac{m_1}{2}$, two of mass $\frac{m_2}{2}$ and one of mass m_3). The pendulum is assumed to be under the influence of gravity ($g = 9.81\,\mathrm{ms}^{-2}$) and in vacuum. Also shown is the trajectory followed by the centre of m_3.

The equations for the pendulum have been derived in a very general form which allows each link in the pendulum to have an arbitrary moment of inertia [8]. In the present work we consider the equations for a pendulum consisting of three point masses, i.e. we neglect the moments of inertia of the three links shown in Fig. 1. The equations for this special case are given in Appendix A of Ref. [12] in the form,

$$\frac{\mathrm{d}\mathbf{x}}{\mathrm{dt}} = \mathbf{f}\left(\mathbf{x}, \alpha, t\right) \ . \tag{1}$$

In Eq. (1), $\alpha \equiv (m_1, m_2, m_3, \ell_1, \ell_2, \ell_3, c_1, c_2, c_3)$, represents the system parameters, where c_{1-3} model the viscous damping in each joint. The vector $\mathbf{x} \equiv (\theta_1, \theta_2, \theta_3, \dot{\theta}_1, \dot{\theta}_2, \dot{\theta}_3)$, where θ_{1-3} are the angles made between the vertical and each of the three links.

3 Linearisation at the equilibria

The spatial distribution and local dynamical characteristics of the equilibria of a system greatly influence its nonlinear dynamics. Since the un-damped pendulum is conservative, having only time independent constraints, its equilibria are defined by the vanishing of the generalised forces Q_i [13], i.e. by,

$$Q_i = \frac{\partial V}{\partial x_i} = 0 \ \ (\text{for } i = 1, 2, 3) \ , \tag{2}$$

where $V\left(x_1, x_2, x_3\right) = \left(m_1 + m_2 + m_3\right) g\ell_1 \cos x_1 + \left(m_2 + m_3\right) g\ell_2 \cos x_2 + m_3 g\ell_3 \cos x_3$ is the potential energy. The solutions to Eq. (2) produce eight physically distinct equilibria, as shown in Fig. 2.

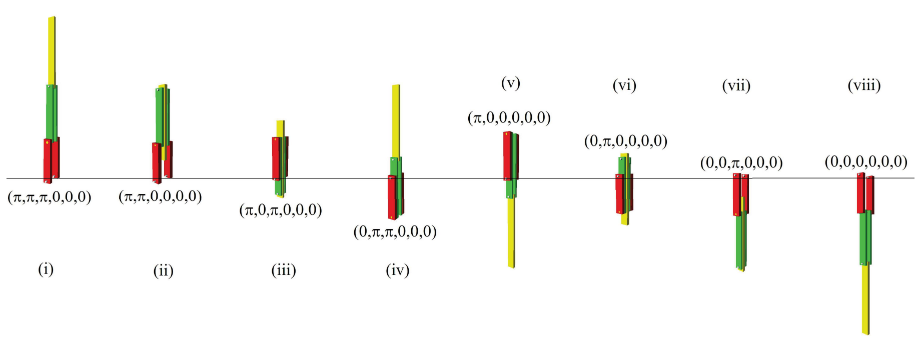

Fig. 2. The eight physically distinct equilibrium configurations of the pendulum. Configurations (i) to (vii) are unstable. Configuration (viii) is stable.

To characterize the linearised dynamics of the system near each equilibrium, we calculate the Jacobian matrix of the system and determine its eigenvalues at the equilibria. The Jacobian matrix, evaluated at any of the equilibria, has the form

$$\mathbf{J} = \begin{pmatrix} 0 & 0 & 0 & 1 & 0 & 0 \\ 0 & 0 & 0 & 0 & 1 & 0 \\ 0 & 0 & 0 & 0 & 0 & 1 \\ \pm J_1 & \pm J_2 & 0 & 0 & 0 & 0 \\ \pm J_3 & \pm J_4 & \pm J_5 & 0 & 0 & 0 \\ 0 & \pm J_6 & \pm J_7 & 0 & 0 & 0 \end{pmatrix} , \tag{3}$$

where $J_1 = g\,(m_1 + m_2 + m_3)\,/\,(\ell_1 m_1)$, $J_2 = g\,(m_2 + m_3)\,/\,(\ell_1 m_1)$, $J_3 = g\,(m_1 + m_2 + m_3)\,/\,(\ell_2 m_1)$, $J_4 = g\,(m_1 + m_2)\,(m_2 + m_3)\,/\,(\ell_2 m_1 m_2)$, $J_5 = g m_3/\,(\ell_2 m_2)$, $J_6 = g\,(m_2 + m_3)\,/\,(\ell_3 m_2)$ and $J_7 = g\,(m_2 + m_3)\,/\,(\ell_3 m_2)$. To evaluate $\mathbf{J}$ at any particular equilibrium, the signs preceding J_{1-7} in Eq. (3) must be chosen according to the convention given in Table 1.

Equilibrium config.	J_1	J_2	J_3	J_4	J_5	J_6	J_7
(i) $(\pi,\pi,\pi,0,0,0)$	+	-	-	+	-	-	+
(ii) $(\pi,\pi,0,0,0,0)$	+	-	-	+	-	+	-
(iii) $(\pi,0,\pi,0,0,0)$	+	-	+	-	+	-	+
(iv) $(\pi,0,0,0,0,0)$	+	-	+	-	+	+	-
(v) $(0,\pi,\pi,0,0,0)$	-	+	-	+	-	-	+
(vi) $(0,\pi,0,0,0,0)$	-	+	-	+	-	+	-
(vii) $(0,0,\pi,0,0,0)$	-	+	+	-	+	-	+
(viii) $(0,0,0,0,0,0)$	-	+	+	-	+	+	-

Table 1. The choice of signs preceding J_{1-7} in Eq. (3) for each of the eight possible equilibrium configurations listed in the left hand column. These combinations of signs should also be used in the definitions of b, c and d in Eq. (4).

The eigenvalues η of the Jacobian matrix were determined by solving the characteristic equation $\det(\mathbf{J} - \eta\mathbf{1}) = 0$, where $\mathbf{1}$ is the 6×6 identity matrix. By choosing all the signs in Eq. (3) to be positive, we found the characteristic equation,

$$0 = a\eta^6 + b\eta^4 + c\eta^2 + d \;, \tag{4}$$

where $a = 1$, $b = J_1J_4J_7 - J_1J_5J_6 - J_2J_3J_7$, $c = J_1J_4 - J_2J_3 - J_1J_7 - J_4J_7 + J_5J_6$ and $d = J_7 - J_1 - J_4$. In the expressions for b, c and d the correct combination of signs, for a particular equilibrium, must once again be chosen from Table 1. For example, for the second equilibrium, row (ii) in Table 1, one obtains $d = (-)\,J_7 - (+)\,J_1 - (+)\,J_4$.

Since Eq. (4) is a cubic polynomial in η^2, its solutions could be written algebraically [15]. The discriminant of each eigen solution was then used to prove that the type of solution associated with a particular equilibrium configuration is independent of the system parameters. These results are presented in Table 2. To present the complete analysis of the fixed points associated with each equilibrium in Table 2 is beyond the scope of the present article. Briefly, our analysis reveals that (i) to (vii) may be associated with various types of saddle points (depending on the parameter values) and that (viii) will always remain a nonlinear centre.

Table 2. The various types of eigenvalues obtained by solving Eq. (4) at each of the eight possible equilibrium configurations.

Equilibrium config.	Stability	Eigenvalues of $\mathbf{J}$
(i) $(\pi, \pi, \pi, 0, 0, 0)$	unstable	all real
(ii) $(\pi, \pi, 0, 0, 0, 0)$	unstable	4 real, 2 imaginary
(iii) $(\pi, 0, \pi, 0, 0, 0)$	unstable	4 real, 2 imaginary
(iv) $(\pi, 0, 0, 0, 0, 0)$	unstable	2 real, 4 imaginary
(v) $(0, \pi, \pi, 0, 0, 0)$	unstable	4 real, 2 imaginary
(vi) $(0, \pi, 0, 0, 0, 0)$	unstable	2 real, 4 imaginary
(vii) $(0, 0, \pi, 0, 0, 0)$	unstable	2 real, 4 imaginary
(viii) $(0, 0, 0, 0, 0, 0)$	stable	all imaginary

4 New method for locating periodic orbits

Knowledge of the periodic orbits and their stability is an important aspect of understanding chaotic systems and therefore a great deal of research has already gone into developing more efficient methods for discovering the periodic orbits and periods of non-linear dynamic systems. See, for example, Refs. [16–18], and references therein. In this section we will develop a new method for finding the periodic orbits by making use of the Levenberg-Marquardt algorithm for least-squares estimation of nonlinear parameters [19].

Assume that the system has a periodic orbit with principle period T. As pointed out by Li and Xu [17], it is convenient to use T as one of the optimisation parameters. We therefore re-write Eq. (1) in terms of a dimensionless time parameter τ, by setting $t = T\tau$. This substitution produces the equivalent equation,

$$\frac{\mathrm{d}\mathbf{x}}{\mathrm{d}\tau} = T\mathbf{f}\left(\mathbf{x}, \alpha, T\tau\right) \ . \tag{5}$$

Since τ is measured in units of T, Eq. (5) has the advantage that it can be integrated over exactly one period, by letting τ run from zero to one.

In order to search for periodic orbits we define the residual (error vector),

$$\mathbf{R} = \left(\mathbf{x}\left(1\right) - \mathbf{x}\left(0\right), \mathbf{x}\left(1 + \varDelta\tau\right) - \mathbf{x}\left(\varDelta\tau\right), \ldots, \mathbf{x}\left(1 + n\varDelta\tau\right) - \mathbf{x}\left(n\varDelta\tau\right)\right), \tag{6}$$

where $\varDelta\tau$ is the integration step size. In Eq. (6), n is an integer which must be chosen large enough to ensure that $\mathbf{R}$ has a greater number of components than the number of quantities which are to be optimised simultaneously. This choice is required by the Levenberg-Marquardt algorithm, which is used to locate the global minimum in $\mathbf{R}$ (note that $\mathbf{R} = \mathbf{0}$ for periodic orbits). In the case of the un-damped pendulum, for example, if all possible quantities are to be optimised simultaneously, i.e. six initial conditions, plus six parameters, plus the period (13 quantities); then one must choose $n \geq 2$. The smallest possible choice for this case is $n = 2$, which produces a residual with $6(n + 1) = 18$ components (see Eq. 6).

The definition of $\mathbf{R}$ requires the system to be integrated from $\tau = 0$ to $\tau = 1 + n\varDelta\tau$. In the present work we have used a fourth-order Runge-Kutta integration scheme with $n = 3$ and $\varDelta\tau = 1/N$, where $N = 2000$. We have implemented the method in the *Python* programming language [14]. The module *Scipy.optimize* contains the function *leastsq*, which makes use of a modified Levenberg-Marquardt algorithm [20].

When applied to the triple pendulum, the method produces a surprisingly large number of (numerically) stable and unstable periodic orbits. Many of the found orbits at first appear to be qualitatively similar (when viewed on a screen), but are in fact quantitatively different, when studied numerically. In Fig. 3 we have plotted four examples of different periodic orbits that were found. Figure 3 (a) shows a stable symmetric orbit of period $T = 3.0363595\,\mathrm{s}$.

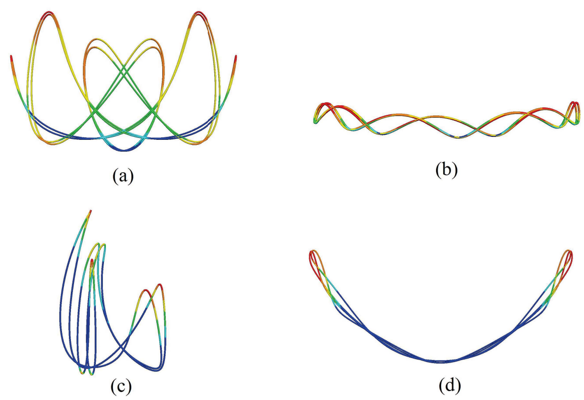

Fig. 3. Four different periodic orbits followed by the centre of m_3, i.e. here $Y = -\ell_1 \cos x_1 - \ell_2 \cos x_2 - \ell_3 \cos x_3$ is plotted against $X = \ell_1 \sin x_1 + \ell_2 \sin x_2 + \ell_3 \sin x_3$, for the first 10 s. (a) Symmetric and stable. (b) Broken-symmetric and stable. (c) Broken-symmetric and unstable. (d) Symmetric and unstable. The colour of each orbit represents the speed of m_3 in the range zero (red) to $2\,\mathrm{ms}^{-1}$ (blue).

One point on the orbit is $(-0.20813379, -0.47019033, 0.80253405, -4.0363589, 4.42470966, 8.3046730)$, with the parameters $m_{1-3} = 0.1\,\mathrm{kg}$, $\ell_1 = 0.15\,\mathrm{m}$ and $\ell_{2-3} = 0.1\,\mathrm{m}$. Figure 3 (b) shows a stable broken-symmetric orbit of period $T = 2.78866884\,\mathrm{s}$. One point on the orbit is $(-0.22395671, 0.47832902, 0.22100014, -1.47138911, 1.29229544, -0.27559337)$, with the parameters $m_1 = 0.1\,\mathrm{kg}$, $m_2 = 0.2\,\mathrm{kg}$, $m_3 = 0.1\,\mathrm{kg}$, $\ell_1 = 0.15\,\mathrm{m}$, $\ell_2 = 0.2\,\mathrm{m}$ and $\ell_3 = 0.3\,\mathrm{m}$. The Lyapunov exponents for the orbits shown in Figs. 3 (a) and (b) confirm that the orbits are periodic.

Figure 3 (c) shows an unstable broken-symmetric orbit of period $T = 3.23387189\,\mathrm{s}$. One point on the orbit is $(-0.78539816, 0.79865905, 0.72867705, 0.74762606, 2.56473963, -2.05903234)$, with the parameters $m_1 = 0.35\,\mathrm{kg}$, $m_2 = 0.2\,\mathrm{kg}$, $m_3 = 0.3\,\mathrm{kg}$, $\ell_1 = 0.3\,\mathrm{m}$, $\ell_2 = 0.2\,\mathrm{m}$ and $\ell_3 = 0.25\,\mathrm{m}$. The Lyapunov exponents, sampled every 0.0005 s for 2000 s, confirm that this orbit is hyperchaotic, with $\lambda_1 = 0.90$, $\lambda_2 = 0.19$ and $\lambda_3 = 0.002$. Figure 3 (d) shows an unstable symmetric orbit of period $T = 3.44620156\,\mathrm{s}$. One point on the orbit is $(1.30564176, 1.87626915, 1.13990186, 0.75140557, 1.65979939, -2.31442362)$, with the parameters $m_1 = 0.35\,\mathrm{kg}$, $m_2 = 0.2\,\mathrm{kg}$, $m_3 = 0.3\,\mathrm{kg}$, $\ell_1 = 0.3\,\mathrm{m}$, $\ell_2 = 0.2\,\mathrm{m}$ and $\ell_3 = 0.25\,\mathrm{m}$. The Lyapunov exponents, sampled every 0.0005 s for 2000 s, confirm that the orbit is also hyperchaotic, with $\lambda_1 = 2.95$, $\lambda_2 = 1.10$ and $\lambda_3 = 0.004$.

To investigate the rapid transition that occurs from periodic to hyperchaotic the time series and Poincaré maps of each orbit have been studied. Figure 4(a) shows the time series of x_6 for each of the four orbits.

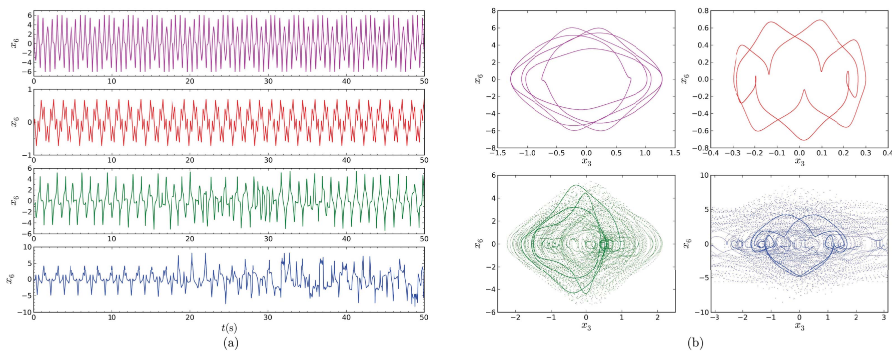

Fig. 4. (a) Time series of x_6 for the orbits discussed in connection with Figs. 3 (a) magenta (top), (b) red, (c) green and (d) blue (bottom). (b) The corresponding Poincaré maps. Parameter values and initial conditions are as for Fig. 3.

The corresponding Poincaré maps, shown in Fig. 4 (b), were constructed by sampling the trajectories every 0.001 s, for 100 s. For this relatively short time interval the periodic parts of the two unstable orbits are still clearly visible within the surrounding (so-called) stochastic layer that is thought to replace the region of destroyed separatrices [21].

5 Discussion and conclusion

The equations for a triple plane pendulum, consisting of three point masses connected by massless links, have been analysed. It was shown that there are only eight physically distinct equilibrium configurations for the pendulum and that the type of eigen solutions obtained for the linearised system at each equilibrium is independent of the system parameter values. A new method for extracting the periodic orbits of the system was also developed. The new method exploits the high-efficiency of the modified Levenberg-Marquardt algorithm. It is simple to implement and does not require the computation of the Jacobian matrix. In addition, the minimisation algorithm may easily be constrained in order to restrict the search to specific regions of the phase space; for example, to a constant energy surface. One possible disadvantage of the method is that it does not discriminate between unstable and stable periodic orbits. However, this aspect of the method may in fact be an important advantage, since it enables the method to be used for studying the coexistence of both regions of stable dynamics and hyperchoas within the phase space.

Acknowledgments

This work is based upon research supported by the National Research Foundation of South Africa (Nos. IFR2011033100063 and IFR2009090800049) and the Eskom–Trust/Tertiary Education Support Programme of South Africa.

References

1. K. G. Eltohamy and C. Kuo, Int. J. of Systems Science **30**, 505 (1999).
2. T. Furata *et al.*, Robotics Autonomous Systems **37**, 81 (2001).
3. A. S. de Paula, M. A. Savi, and F. H. I. Pereira-Pinto, Journal of Sound and Vibration **294**, 585 (2006).
4. M. Gitterman, *The Chaotic Pendulum* (World Scientific, Singapore, 2010).
5. M. V. Plissi *et al.*, Review of Scientific Instruments **71**, 2539 (2000).
6. G. Kudra, Ph.D. thesis, Technical University of Lódź, 2002.
7. J. Awrejcewicz and C. H. Lamarque, in *World Scientific Series on Nonlinear Science*, Vol. 45 of *Series A*, ed. L. Chua (World Scientific, Singapore, 2003).
8. J. Awrejcewicz, G. Kudra, and C. H. Lamarque, Int. J. of Bifurcation and Chaos **14**, 4191 (2004).
9. J. Awrejcewicz and G. Kudra, Nonlinear Analysis **63**, 909 (2005).
10. J. Awrejcewicz *et al.*, Int. J. of Bifurcation and Chaos **18**, 2883 (2008).
11. S. H. Strogatz, *Nonlinear Dynamics and Chaos* (Addison-Wesley, Reading, 1994).
12. A. E. Botha and G. Qi, in *Proceedings of the 56th Annual Conference of the South African Institute of Physics*, edited by I. Basson and A. E. Botha (University of South Africa, Pretoria, 2011), p. 123, ISBN: 978-1-86888-688-3. Available online at www.saip.org.za.
13. H. Goldstein, *Classical Mechanics*, 2nd ed. (Addison-Wesley, Reading, 1980), p. 243.
14. W. J. Chun, *Core Python Programming* (Prentice Hall, New Jersey, 2007).
15. W. Press, S. Teukolsky, W. Vetterling, and B. Flannery, *Numerical Recipes*, 3rd ed. (Cambridge University Press, New York, 2007), p. 228.
16. T. Zhou, J. X. Xu, and C. L. Chen, J. Sound and Vibration **245**, 239 (2001).
17. D. Li and J. Xu, Engineering with Computers **20**, 316 (2005).
18. D. Li and S. Yang, Chinese Journal of Applied Mechanics **28**, 349 (2011).
19. D. Marquardt, SIAM Journal of Applied Mathematics **11**, 431 (1963).
20. H. P. Langtangen, *Python Scripting for Computational Science* (Springer Verlag, Berlin, 2004), p. 161. Also see www.scipy.org.
21. G. M. Zaslavsky, *The Physics of Chaos in Hamiltonian Systems*, 2nd ed. (Imperial College Press, Singapore, 2007), p. 2.

Synergistic approach to amphibian aircraft nonlinear adaptive regulator design: Harmonic disturbance observers

Prof. Kolesnikov A.A.[*], PhD. Nguyen Phuong[**]

[*] Tagangog Technological University, Southern Federal University, Russia
E-mail: anatoly.kolesnikov@gmail.com
[**] University of Technical Education, Hochiminh City, Vietnam
E-mail: phuongn@fit.hcmute.edu.vn

Abstract: Aircraft amphibian (SA), as a control object, has an extremely complex structure consisting of a set of subsystems including exchange processes of force, energy, matter and information. This control object operates in the complex environments as atmosphere as well as adjoining surface of water and air.
The problem is to design a regulator that to control the flight modes with impact on the surrounding environment. Requirement to designed regulator is quick responsibility to adapt to the impact of chaotic disturbances of environments. In this report we consider a method synthesis nonlinear control system of aircraft amphibian motion with state observers of harmonic disturbances based on synergetic approach in modern control theory
Keywords: Synergistic, system's synthesis, regulator design, chaotic disturbances, aircraft amphibian, nonlinear dynamic modeling.

1. Introduction

The solution of the various control tasks based on using of a control object state vector. In real conditions of full state vector measurement for one reason or another is not feasible. For this purpose, the control system introduces a subsystem of state estimation - a state observer.
For linear systems, it is distinguished full-order state observers (Kalman Observer), which have a dimension of the state vector as same as that of the control object, reduced order observers (Luenbergera Observer) and observers of increased order (adaptive observers) [1, 2]
Proposed in this article, the nonlinear observer can be referring to the reduced order observers. Even more challenging is a problem of estimating the unmeasured external disturbances. The basic idea of perturbation estimation is as follows: To construct a model of external influences, which is in the form of a homogeneous differential equation system with known coefficients and unknown initial conditions. The model is combined with the perturbation model and with this received enhanced system observer is constructed. Obtained with it estimates include the estimates of object state variables, and evaluation of external influences.

Received: 9 May 2012 / Accepted: 28 September 2012

ISSN 2241-0503

The asymptotic observer design methods are applicable for a wide class of nonlinear systems proposed in [3, 4, 5]. In this work, a new version of an amphibian control methods and problems, which are solved by the dynamic synergistic regulators to such observers, is described. These observers have carried out a unmeasured harmonic external disturbance evaluation effecting on the amphibian. The nonlinear external perturbation observers (NEPO) consist of a monitoring contour and a control circuit that operates in parallel.

2. The Problem Statement

Suppose that the control object's behavior and an external disturbances effecting on it could be described by the differential equations system:

$$\dot{x} = g(x, z, u);$$
$$\dot{z} = h(x, z, u).$$

Where n vector x и m vector z – components of state vector; u – a control vector; $g(.)$ и $h(.)$ – continuous nonlinear functions. Vector x is assumed observable, and vector z – unobservable.

Then the observer synthesis problem can be formulated as follows. Need to synthesize NEPO with form:

$$\dot{w}(t) = R(x, w);$$
$$\hat{z}(t) = K(x, w),$$

where w – observer state vector; $\hat{z}$ – unmeasured external disturbances evaluation vector.

In this case, NEPO must provide:

- a closed system asymptotic stability;
- stabilization of the pitch angle, altitude and flight speed;
- assessment of unobserved external perturbations;
- compensation of external disturbances.

The NEPO synthesis procedure is divided into three stages:

a) Synthesis of control laws u_i to ensure implementation of the required technological problem (in this case assume that all control object state variables are observable);
b) Synthesis of an observer for the unobservable state variables and unmeasured disturbances.
c) Replacement of unobservable variables in the synthesized controls by their evaluations.

3. The synergistic procedure of the control laws for the longitudinal motion with harmonic disturbances

a). Synergistic synthesis procedure of control laws u_i

Common model of SA's space movement is present by 12th order differential equations system through Euler angles. In SA's movement on water or in taking off, it's rational to consider longitudinal motion model:

$$\begin{cases} \dot{x}_1(t) = b_1 x_3 x_2 - g\sin x_5 + a_1\left(P_x - F_{ax} - F_{hx}\right) + M_1(t); \\ \dot{x}_2(t) = b_2 x_2 x_3 - g\cos x_5 + a_2\left(P_y + F_{ay} + F_{hy}\right) + M_2(t); \\ \dot{x}_3(t) = a_3\left(M_z^a + M_z^h\right) + M_3(t); \\ \dot{x}_4(t) = x_1 \sin x_5 + x_2 \cos x_5; \\ \dot{x}_5(t) = x_3; \\ \dot{x}_6 = x_1 \cos x_5 - x_2 \sin x_5; \end{cases} \qquad (1)$$

Where: x_1, x_2 – the projections of velocity vector V_x, V_y on corresponded the intertwined coordinate system axes; x_3 – longitudinal angular velocity μ_z; x_4, x_6 – projections coordinate SA's center of gravity y_c, x_c on corresponded axes Oy and Ox; x_4 – pitching angle g; m – SA's weight; $m_x = (1+a_1)m,\ m_y = (1+a_2)m$ – SA's «attached» weights; F_{ax}, F_{ay} – projections total vector of aerodynamic forces on corresponded intertwined coordinate system axes Ox and Oy; F_{hx}, F_{hy} – projections total vector of hydrodynamic and hydrostatic forces on corresponded intertwined coordinate system axes Ox and Oy; Oy; M_z^a, M_z^h – longitudinal aerodynamic moment and longitudinal moment formed by hydrodynamic and hydrostatic forces; $M_i(t)$ – disturbances;

$$a_1 = m_x^{-1};\ a_2 = m_y^{-1};\ a_3 = I_z^{-1};\ b_1\frac{m_y}{m_x};\ b_2 = -\frac{m_x}{m_y}.$$

In control the SA's longitudinal motion elevator, flaps and engine thrust control lever are the active control organs. Technical solutions that provide basing and operation of the aircraft on the water surface, effectively determine its shape - the seaplane aerodynamic scheme. Consequently, controls in the model (2) will be the engine thrust, depending on the deviation of the engine thrust control lever; the total aerodynamic forces and the total longitudinal moment, depending on changes in the flaps and elevator deflection.

For control the SA's longitudinal motion there are some strategies: controlling individual channels or all channels simultaneously. Of course that the vector strategy requires a more complex algorithmic structure of the regulator, but it allows more flexible three-channel control of SA.

The problem of controlling the longitudinal motion is finding the control vector. $u = \left\lfloor F_x\left(¢_{р.у.}, ¢_{р.в.}, ¢_з\right);\ F_y\left(¢_{р.у.}, ¢_{р.в.}, ¢_з\right);\ M_z\left(¢_{р.у.}, ¢_{р.в.}, ¢_з\right) \right\rfloor$ as a coordinate function of the system states, which provides SA's longitudinal short-period movement (2) at a given speed V_0, height H_0 and pitching angle γ_0, i.e. the following invariants:

$$x_1 = V_0;\ x_4 = H_0;\ x_5 = \gamma_0 \qquad (2)$$

Rewriting the mathematic model of the control object following:

$$\begin{cases} \dot{x}_1(t) = b_1 x_3 x_2 - g \sin x_5 + a_1 u_1; \\ \dot{x}_2(t) = -b_2 x_1 x_3 - g \cos x_5 + a_2 u_2\ ; \\ \dot{x}_3(t) = a_3 u_3; \\ \dot{x}_4(t) = x_1 \sin x_5 + x_2 \cos x_5; \\ \dot{x}_5(t) = x_3; \\ \dot{x}_6(t) = x_1 \cos x_5 - x_2 \sin x_5; \end{cases} \qquad (3)$$

where $u_1 = P_x - F_{xa} - F_{x\text{г}}$, $u_2 = P_y + F_{ya} + F_{y\text{г}}$, $u_3 = M_{za} + M_{z\text{г}}$ – are control acts.

For model (3), the goal is implementation of desired invariants (2), we formulate the first set of macro-variables ψ_1, ψ_2, ψ_3,

$$\begin{aligned} &\psi_1 = x_1 - V_0; \\ &\psi_2 = x_2 - \varphi_1(x_4, x_5, z_1, z_2, z_3); \\ &\psi_3 = x_3 - \varphi_2(x_4, x_5, z_1, z_2, z_3), \end{aligned} \qquad (4)$$

which must satisfy the solution of following functional equations:

$$T_i \dot{\psi}_i(t) + \psi_i = 0, \quad T_i > 0, \quad i = 1\ldots3,; \qquad (5)$$

At the intersection of invariant manifolds, $\psi_i = 0, i = 1,\ldots,3$, there is a dynamic “phase space compression”, and the dynamics of closed-loop system will be described by decomposed model:

$$\begin{cases} \dot{x}_4(t) = V_0 \sin x_5 + \varphi_1 \cos x_5; \\ \dot{x}_5(t) = \varphi_2; \\ \dot{x}_6(t) = V_0 \cos x_5 - \varphi_1 \sin x_5; \end{cases} \qquad (6)$$

Now to introduce a second set of macro variables

$$\psi_4 = x_4 - H_0;\ \psi_5 = x_5 - \gamma_0. \qquad (7)$$

The set of macro variables introduced by (7) must satisfy solutions of functional equation systems:

$$T_i \dot{\psi}_i(t) + \psi_i = 0, \quad T_i > 0, \quad i = 4,5. \qquad (8)$$

And to solve jointly equations from (6) to (8) for determining “inner” controls φ_1, φ_2 in form of functions depending on state variables:

$$\ddot{\ }_1 = -\frac{T_4 V_0 \sin x_5 + x_4 - H_0}{T_4 \cos x_5};\ \ddot{\ }_2 = \frac{-x_5 + \mathsf{g}_0}{T_5}. \tag{9}$$

Further external control vectors u_i is found by solving simultaneously functional equation systems (4) and equation model (1):

$$u_1 = \frac{1}{a_1}\left(g \sin x_5 + \frac{-x_1 + V_0}{T_1} - z_1\right);$$

$$u_2 = Ax_1 + Bx_2 + Cx_3 + Dx_4 - \frac{1}{a_2} z_2 + E; \tag{10}$$

$$u_3 = -\frac{1}{T_3 T_5 a_3}\left((T_3 + T_5)x_3 + x_5 - \mathsf{g}_0\right) - \frac{z_3}{a_3}.$$

Where indicated: $A = -\frac{\sin x_5}{T_4 a_2 \cos x_5}$; $B = -\frac{T_2 + T_4}{a_2 T_2 T_4}$;

$$C = -\frac{x_4 \sin x_5}{a_2 T_4 \cos^2 x_5} + \frac{H_0 \sin x_5 - T_4 V_0}{a_2 T_4 \cos^2 x_5};$$

$$D = \frac{-1}{a_2 T_2 T_4 \cos x_5};\ E = \frac{H_0 - T_4 V_0 \sin x_5}{a_2 T_2 T_4 \cos x_5} + \frac{g \cos x_5}{a_2}.$$

Whereas synthesized control laws, u_1, u_2, u_3, of object (1), provide implementation required technological problems, it is necessary to move to description of the observer synthesis procedure.

b) The observer synthesis procedure

According to the method of Analytical Design of Aggregated Regulators, in synergistic synthesis procedure of observers it should be used following an extended system model (11) [3, 4]:

$$\begin{cases} \dot{x}_1(t) = -g \sin x_5 + a_1 u_1 + z_1; \\ \dot{x}_2(t) = -g \cos x_5 + a_2 u_2 + z_2; \\ \dot{x}_3(t) = a_3 u_3 + z_3; \\ \dot{x}_4(t) = x_1 \sin x_5 + x_2 \cos x_5; \\ \dot{x}_5(t) = x_3; \\ \dot{x}_6(t) = x_1 \cos x_5 - x_2 \sin x_5; \\ \dot{z}_1(t) = s_1;\ \dot{s}_1(t) = -\pm_1^2 z_1; \\ \dot{z}_2(t) = s_2;\ \dot{s}_2(t) = -\pm_2^2 z_2; \\ \dot{z}_3(t) = s_3;\ \dot{s}_3(t) = -\pm_3^2 z_3; \end{cases} \tag{11}$$

Where $\pm_i$ – harmonic disturbance angular frequencies, z_1, z_2, z_3 – the projections of indignant linear, longitudinal and angular accelerations respectively.
The last six equations in system (11) is dynamic model of harmonic disturbances, and $z_i, s_i, \; i = \overline{1..3}$ are state variables.

The state variable observer design is based on the synergistic approach principles in the control theory, videlicet on the ADAR method, which is described in works [3, 4]. In particular case, when $\dim \cdot (t) = 1$, the expression

$$\dot{\cdot}(t) = L(y)\cdot \qquad (12)$$

Could be present in following form:

$$\dot{\cdot}_i(t) + L_i \cdot_i = 0, \quad L_i > 0. \qquad (13)$$

To conduct the synthesis of the observers for the object (1), let $y = [x_i], \; i = 1,...,5$, $v = \lfloor z_j, s_j \rfloor, \; j = 1,2,3$. To determine the assessments of the state variables z_1, s_1, choosing forms of $\cdot_1, \cdot_2$:

$$\begin{aligned} \cdot_1 &= {}_{11}(z_1 - \hat{z}_1) + {}_{12}(s_1 - \hat{s}_1), \\ \cdot_2 &= {}_{21}(z_1 - \hat{z}_1) + {}_{22}(s_1 - \hat{s}_1). \end{aligned} \qquad (14)$$

Where ${}_{ij} \neq 0$ – constants, ${}_{11}\,{}_{22} - {}_{12}\,{}_{21} \neq 0$. In this the valuations $\hat{z}_1, \hat{s}_1$ of the state variables z_1, s_1 could be formed by

$$\begin{aligned} \hat{z}_1 &= f_1(x_1) + w_1, \\ \hat{s}_1 &= f_2(x_1) + w_2. \end{aligned} \qquad (15)$$

where $f_1(x_1), \; f_2(x_1)$ – unknown functions. Then to put (14) into the equation in formed (13):

$$\begin{aligned} \dot{\cdot}_1(t) + L_1 \cdot_1 &= 0, \; L_1 > 0; \\ \dot{\cdot}_2(t) + L_2 \cdot_2 &= 0, \; L_2 > 0, \end{aligned} \qquad (16)$$

while subject to the equations (15), receiving

$$\begin{aligned} &{}_{11}\left(\frac{dz_1}{dt} - \frac{\partial f_1(x_1)}{x_1}\frac{dx_1}{dt} - \frac{d(w_1)}{dt}\right) + {}_{12}\left(\frac{ds_1}{dt} - \frac{\partial f_2(x_1)}{x_1}\frac{dx_1}{dt} - \frac{d(w_2)}{dt}\right) + \\ &+ L_1[\,{}_{11}(z_1 - f_2(x_1) - w_1) + {}_{12}(s_1 - f_2(x_1) - w_2)] = 0, \\ &{}_{21}\left(\frac{dz_1}{dt} - \frac{\partial f_1(x_1)}{x_1}\frac{dx_1}{dt} - \frac{d(w_1)}{dt}\right) + {}_{22}\left(\frac{ds_1}{dt} - \frac{\partial f_2(x_1)}{x_1}\frac{dx_1}{dt} - \frac{d(w_2)}{dt}\right) + \\ &+ L_2[\,{}_{21}(z_1 - f_1(x_1) - w_1) + {}_{22}(s_1 - f_2(x_1) - w_2)] = 0. \end{aligned} \qquad (17)$$

With the equations (17) subject to the object equations (11), receiving:

$$
\begin{aligned}
&{}_{11}\left(s_1 - \frac{\partial f_1(x_1)}{x_1}\left(-g\sin x_5 + a_1u_1 + z_1\right) - \frac{dw_1}{dt}\right) + \\
&{}_{12}\left(-\pm_1{}^2 z_1 - \frac{\partial f_2(x_1)}{x_1}\left(-g\sin x_5 + a_1u_1 + z_1\right) - \frac{dw_2}{dt}\right) \\
&+ L_1\left[\ {}_{11}\left(z_1 - f_1(x_1) - w_1\right) + \ {}_{12}\left(s_1 - f_2(x_1) - w_2\right)\right] = 0; \\
&{}_{21}\left(s_1 - \frac{\partial f_1(x_1)}{x_1}\left(-g\sin x_5 + a_1u_1 + z_1\right) - \frac{dw_1}{dt}\right) + \\
&{}_{22}\left(-\pm_1{}^2 z_1 - \frac{\partial f_2(x_1)}{x_1}\left(-g\sin x_5 + a_1u_1 + z_1\right) - \frac{dw_2}{dt}{}_1\right) \\
&+ L_2\left[\ {}_{21}\left(z_1 - f_1(x_1) - w_1\right) + \ {}_{22}\left(s_1 - f_2(x_1) - w_2\right)\right] = 0.
\end{aligned}
\tag{18}
$$

In the equations of the observer (18) must not be present at unobserved coordinators z_1, s_1. In order to exclude them out of system, choosing

$$
\begin{aligned}
&f_1(x_1) = \frac{{}^2{}_{12}\ {}^2{}_{21} - \ {}^2{}_{22}\ {}^2{}_{11}}{{}_{12}\ {}_{22}\left({}_{11}\ {}_{22} - \ {}_{12}\ {}_{21}\right)} x_1, \\
&f_2(x_1) = \left(\frac{{}_{21}\ {}_{22}\ {}^2{}_{11} - \ {}_{11}\ {}_{12}\ {}^2{}_{21}}{{}_{12}\ {}_{22}\left({}_{11}\ {}_{22} - \ {}_{12}\ {}_{21}\right)} - \pm_1^2\right) x_1,
\end{aligned}
\tag{19}
$$

$$
L_1 = -\frac{{}_{11}}{{}_{12}} > 0,\ \ L_2 = -\frac{{}_{21}}{{}_{22}} > 0
$$

Subject to (19), to solve the system of equations (18), finding

$$
\begin{aligned}
&\dot{w}_1 = -\left[\left(\frac{{}_{11}}{{}_{12}}\right)^2 + \pm_1^2 + \frac{{}_{21}\ {}_{11}}{{}_{22}\ {}_{12}} + \left(\frac{{}_{21}}{{}_{22}}\right)^2\right] x_1 + \\
&\quad + \left(\frac{{}_{11}}{{}_{12}} + \frac{{}_{21}}{{}_{22}}\right)\left(w_1 + a_1u_1 - g\sin x_5\right) + w_2; \\
&\dot{w}_2 = \left(\frac{{}_{21}\ {}^2{}_{11}}{{}_{22}\ {}^2{}_{12}} + \frac{{}_{11}\ {}^2{}_{21}}{{}_{12}\ {}^2{}_{22}}\right) x_1 + \left(\frac{{}_{11}\ {}_{21}}{{}_{22}\ {}_{12}}\right)\left(g\sin x_5 - a_1u_1 - w_1\right) + \\
&\quad + \pm_1^2\left(a_1u_1 - g\sin x_5\right).
\end{aligned}
\tag{20}
$$

And the valuations $\hat{z}_1, \hat{s}_1$ of the state variables z_1, s_1 are

$$\hat{z}_1 = \frac{{}^{2}_{12}\;{}^{2}_{21} - {}^{2}_{22}\;{}^{2}_{11}}{{}_{12}\;{}_{22}\left({}_{11}\;{}_{22} - {}_{12}\;{}_{21}\right)} x_1 + w_1,$$
$$\hat{s}_1 = \left(\frac{{}_{21}\;{}_{22}\;{}^{2}_{11} - {}_{11}\;{}_{12}\;{}^{2}_{21}}{{}_{12}\;{}_{22}\left({}_{11}\;{}_{22} - {}_{12}\;{}_{21}\right)} - \pm^{2}_{1} \right) x_1 + w_2. \tag{21}$$

Similarly, to define the estimations $\hat{z}_2$, $\hat{s}_2$, $\hat{z}_2$, $\hat{s}_2$ of the state variables z_2, s_2, z_2, s_2, choosing following the macro variables

$$\begin{aligned} \cdot_3 &= {}_{33}\left(z_2 - \hat{z}_2\right) + {}_{34}\left(s_2 - \hat{s}_2\right); \\ \cdot_4 &= {}_{43}\left(z_2 - \hat{z}_2\right) + {}_{44}\left(s_2 - \hat{s}_2\right); \\ \cdot_5 &= {}_{55}\left(z_3 - \hat{z}_3\right) + {}_{56}\left(s_3 - \hat{s}_3\right); \\ \cdot_6 &= {}_{65}\left(z_3 - \hat{z}_3\right) + {}_{66}\left(s_3 - \hat{s}_3\right), \end{aligned} \quad \text{where} \quad \begin{aligned} &{}_{33}\;{}_{44} - {}_{34}\;{}_{43} \neq 0; \\ &{}_{55}\;{}_{66} - {}_{56}\;{}_{65} \neq 0;. \\ &{}_{ij} \neq 0. \end{aligned} \tag{22}$$

The assessments of state variables z_2, s_2, z_2, s_2 can be defined

$$\hat{z}_2 = f_3(x_2) + w_3, \quad \hat{s}_2 = f_4(x_2) + w_4,$$
$$\hat{z}_3 = f_5(x_3) + w_5, \quad \hat{s}_3 = f_6(x_3) + w_6, \tag{23}$$

The macro variables (22) must be satisfy functional equations

$$\dot{\cdot}_i(t) + L_i \cdot_i = 0, \; L_i > 0, \; i = 3,...,6. \tag{24}$$

With received equations formed by putting (22) in to (16) object to model (11), we need to choose functions $f_3(x_2)$, $f_4(x_2)$, $f_5(x_3)$, $f_6(x_3)$, L_i, $i = 3,...,6$ so that the expressions of the observers must not consist in itself the unobserved state variables. Choosing

$$f_3(x_2) = \frac{{}^{2}_{34}\;{}^{2}_{43} - {}^{2}_{44}\;{}^{2}_{33}}{{}_{34}\;{}_{44}\left({}_{33}\;{}_{44} - {}_{34}\;{}_{43}\right)} x_2;$$
$$f_4(x_2) = \left(\frac{{}_{43}\;{}_{44}\;{}^{2}_{33} - {}_{33}\;{}_{34}\;{}^{2}_{43}}{{}_{34}\;{}_{44}\left({}_{33}\;{}_{44} - {}_{34}\;{}_{43}\right)} - \pm^{2}_{2} \right) x_2; \tag{25}$$

$$L_3 = -\frac{{}_{33}}{{}_{34}} > 0, \; L_4 = -\frac{{}_{43}}{{}_{44}} > 0$$

$$f_5(x_3) = \frac{{}^{2}_{56}\;{}^{2}_{65} - {}^{2}_{66}\;{}^{2}_{55}}{{}_{56}\;{}_{66}\left({}_{55}\;{}_{66} - {}_{56}\;{}_{65}\right)} x_3;$$
$$f_6(x_3) = \left(\frac{{}_{65}\;{}_{66}\;{}^{2}_{55} - {}_{55}\;{}_{56}\;{}^{2}_{65}}{{}_{56}\;{}_{66}\left({}_{55}\;{}_{66} - {}_{56}\;{}_{65}\right)} - \pm^{2}_{3} \right) x_3. \tag{26}$$

$$L_5 = -\frac{{}_{55}}{{}_{56}} > 0, \; L_6 = -\frac{{}_{65}}{{}_{66}} > 0$$

Consequently the equations of the observer is formed

$$\dot{w}_3(t) = -\left[\left(\frac{{}_{33}}{{}_{34}}\right)^2 + \pm_2^2 + \frac{{}_{43}\;{}_{33}}{{}_{44}\;{}_{34}} + \left(\frac{{}_{43}}{{}_{44}}\right)^2\right]x_2 +$$

$$+\left(\frac{{}_{33}}{{}_{34}} + \frac{{}_{43}}{{}_{44}}\right)(w_3 + a_2u_2 - g\cos x_5) + w_4;$$

$$\dot{w}_4(t) = \left(\frac{{}_{43}\;{}_{33}^2}{{}_{44}\;{}_{34}^2} + \frac{{}_{33}\;{}_{43}^2}{{}_{34}\;{}_{44}^2}\right)x_2 + \left(\frac{{}_{33}\;{}_{43}}{{}_{44}\;{}_{34}}\right)(g\cos x_5 - a_2u_2 - w_3) + \qquad (27)$$

$$+\pm_2^2(a_2u_2 - g\cos x_5).$$

$$\dot{w}_5(t) = -\left[\left(\frac{{}_{55}}{{}_{56}}\right)^2 + \pm_3^2 + \frac{{}_{65}\;{}_{55}}{{}_{66}\;{}_{56}} + \left(\frac{{}_{65}}{{}_{66}}\right)^2\right]x_3 + \left(\frac{{}_{55}}{{}_{56}} + \frac{{}_{65}}{{}_{66}}\right)(w_5 + a_3u_3) + w_6;$$

$$\dot{w}_6(t) = \left(\frac{{}_{65}\;{}_{55}^2}{{}_{66}\;{}_{56}^2} + \frac{{}_{55}\;{}_{65}^2}{{}_{56}\;{}_{66}^2}\right)x_3 + \left(\frac{{}_{55}\;{}_{65}}{{}_{66}\;{}_{56}}\right)(-a_3u_3 - w_5) + \pm_3^2 a_3u_3.$$

And expressions of state variable evaluations z_2, z_3, s_2, s_3 is described

$$\hat{z}_2 = \frac{{}^2_{34}\;{}^2_{43} - {}^2_{44}\;{}^2_{33}}{{}_{34}\;{}_{44}({}_{33}\;{}_{44} - {}_{34}\;{}_{43})}x_2 + w_3,$$

$$\hat{s}_2 = \left(\frac{{}_{43}\;{}_{44}\;{}^2_{33} - {}_{33}\;{}_{34}\;{}^2_{43}}{{}_{34}\;{}_{44}({}_{33}\;{}_{44} - {}_{34}\;{}_{43})} - \pm_2^2\right)x_2 + w_4; \qquad (28)$$

$$\hat{z}_3 = \frac{{}^2_{56}\;{}^2_{65} - {}^2_{66}\;{}^2_{55}}{{}_{56}\;{}_{66}({}_{55}\;{}_{66} - {}_{56}\;{}_{65})}x_3 + w_5,$$

$$\hat{s}_3 = \left(\frac{{}_{65}\;{}_{66}\;{}^2_{55} - {}_{55}\;{}_{56}\;{}^2_{65}}{{}_{56}\;{}_{66}({}_{55}\;{}_{66} - {}_{56}\;{}_{65})} - \pm_3^2\right)x_3 + w_6;$$

Thus, combining equations (20) and (27), we obtain a nonlinear state observer for the external harmonic wave disturbances. Note that the unobserved variable z_1, z_2, z_3 in the synthesized controls (10) should be replaced by its estimates $\hat{z}_1, \hat{z}_2, \hat{z}_3$ (15) and (28).

4. Simulation

The results of computer simulation of closed-loop system (11) with the synthesized NEPO are shown in figure 1 to figure 17.

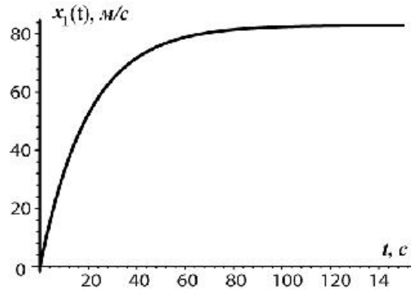

Fig. 1 Transient process relatively horizontal speed V_x

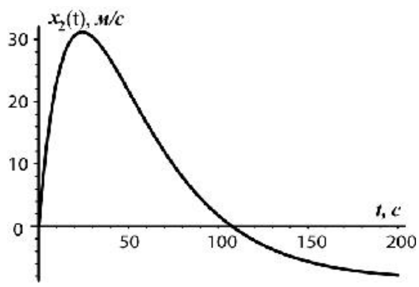

Fig. 2 Transient process relatively vertical speed V_y

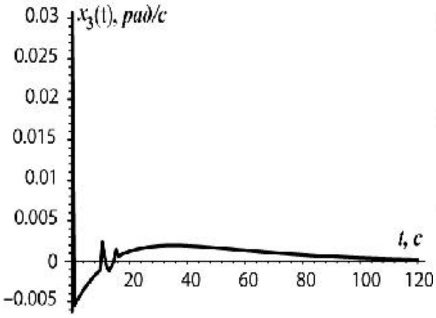

Fig. 3 Transient process relatively angular speed μ_z

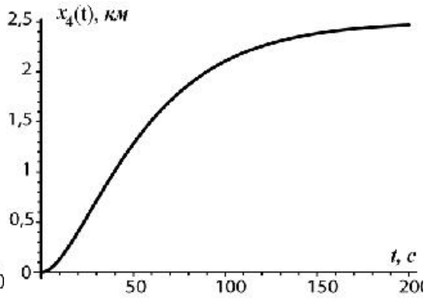

Fig. 4 Transient process relatively flight height H

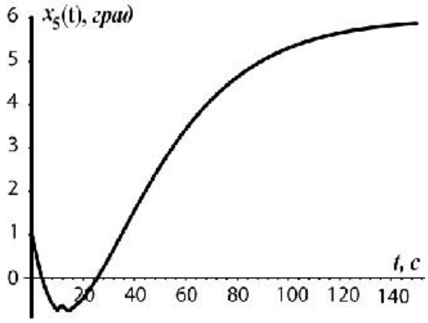

Fig. 5 Transient process relatively pitch angular speed g

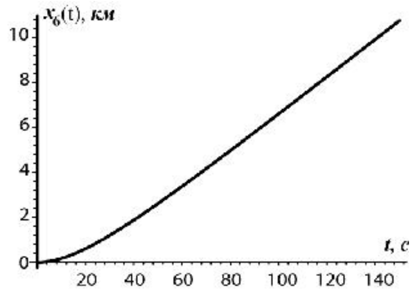

Fig. 6 Transient process relatively flight distance X

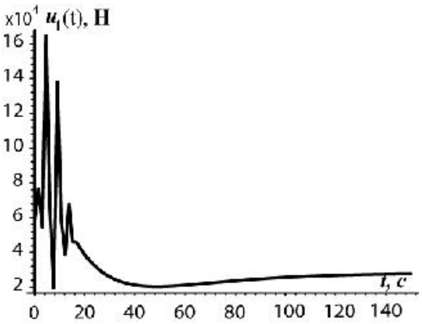

Fig. 7 Transient process relatively control u_1

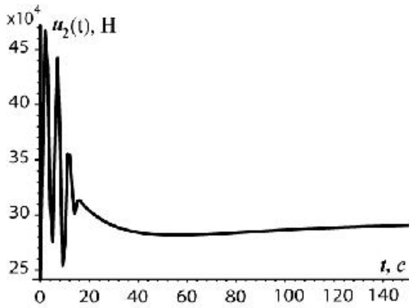

Fig. 8 Transient process relatively control u_2

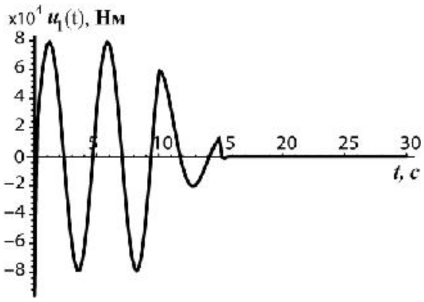

Fig. 9 Transient process relatively control u_3

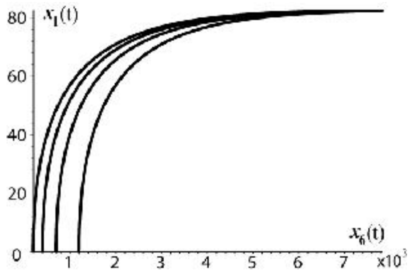

Fig. 10 Projection of system phase trajectory on surface $x_1(t) \& x_6(t)$

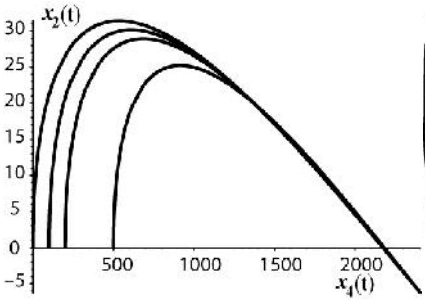

Fig. 11 Projection of system phase trajectory on surface $x_2(t) \& x_4(t)$

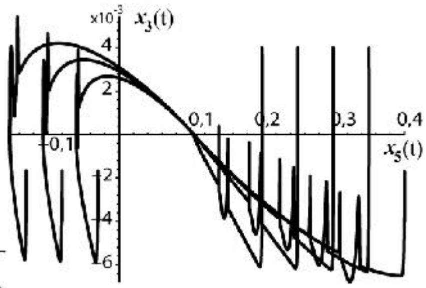

Fig. 12 Projection of system phase trajectory on surface $x_3(t) \& x_5(t)$

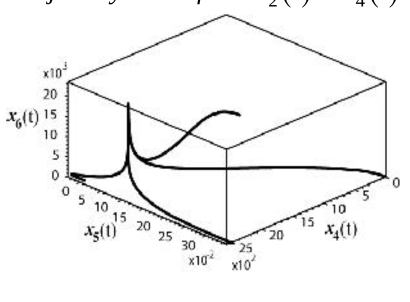

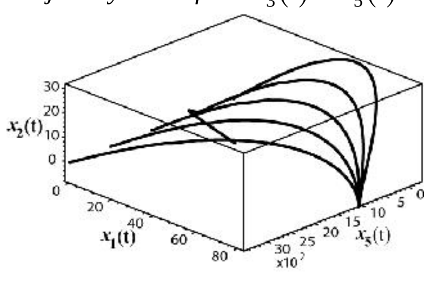

Fig. 13 Phase portrait in space $x_4(t), x_5(t), x_6(t)$

Fig. 14 Phase portrait in space $x_5(t),\ x_1(t),\ x_2(t)$

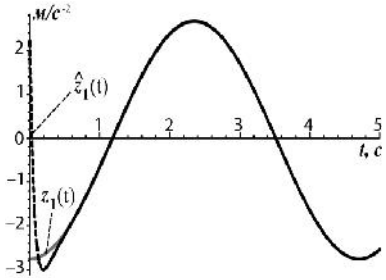

Fig. 15 Transient process relatively disturbance $z_1(t)$ *and its estimation*

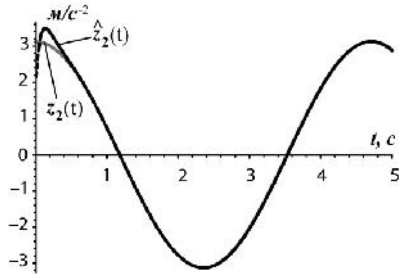

Fig. 16 Transient process relatively $z_2(t)$ *and its estimation*

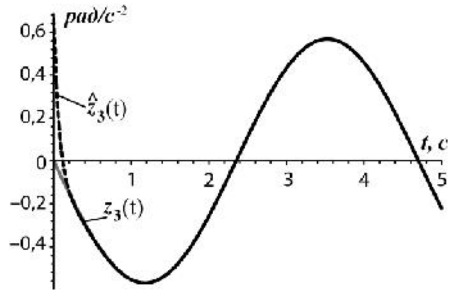

Fig. 17 Transient process relatively $z_3(t)$ *and its evaluation*

5. Conclusion

This work is described the synergistic approach to problem of synthesis of effective correlated control laws of longitudinal motion SA under sea wave conditions, particularly in taking off process from water surface.

In conducting the simulation showed that the SA's longitudinal motion control objectives are achieved and using synthesized control laws can significantly improve motion performance: decreasing pitch angle oscillation, angular rate fluctuations and SA's gravity center oscillation. The observers estimate the unobserved disturbances with high measurement accuracy (fig.15-fig.17).

Thus, using synergetic control theory enable to create new classes of SA's motion control systems.

References

1. *Андриевский Б.Р., Фрадков АЛ.* Избранные главы теории автоматического управления с примерами на языке MATLAB. С.-Петербург: Наука, 1999.
2. *Фомин В.Н., Фрадков А.Л., Якубович В.А.* Адаптивное управление динамическими объектами. – М.: Наука, 1981.
3. *Колесников А.А.* Синергетическая теория управления. Таганрог: ТРТУ, М.: Энергоатомиздат, 1994. 344 с.

4. Современная прикладная теория управления: Синергетический подход к теории управления / под ред. А.А. Колесникова. – Таганрог: Изд-во ТРТУ, 2000. – Ч II.
5. *Колесников А.А., Веселов Г.Е., Кузьменко А.А.* Новые технологии проектирования современных систем управления процессами генерации электроэнергии. – М.: 2009. 323 с.

CMSIM

(This page internationally left blank)

Chaotic Modeling and Simulation (CMSIM) 2: 319-322, 2013

THE PECULIARITIES OF THE CELLS METABOLISM DUE TO THE FLOW OF LIQUID THROW CELL MEMBRANE

O.I. Krivosheina, I.V. Zapuskalov,Y.I Khoroshikh, O.B.Zapuskalova
Siberian State Medical University, Tomsk, Russia
E-mail: oikr@yandex.ru

Abstract: A device is designed for *in vitro* modeling of the directed flow of a nutrient medium similar to the fluid flow in the eyeball. The primary culture of human fibroblasts was cultivated in the permanent directed flow of the medium for 24 and 48 h. Under dynamic conditions, an increase in the intracellular fermentative activity of cells of the fibroblastic population and the acceleration of the process of their differentiation into mature forms were observed.

Keywords: culture of human fibroblasts, the fluid flow, the intracellular fermentative activity, the process of the differentiation/

Implementation of morphofunctional capabilities of cells intermediating the initiation, development, and outcome of any pathological process depends significantly on the modulating influence of microenvironment factors. In the eyeball, the microenvironment consists of the interacting system of anatomico-physiological features and extrastromal regulation components. Anatomico-physiological features are determined by the presence of the directed flow of the intraocular fluid and by the fibrillar structure of the vitreous body. Extrastromal components are represented by cellular elements migrating into the vitreal cavity (cells of the retinal pigment epithelium, monocytes/macrophages, lymphocytes, etc.) and by humoral factors (cytokines, growth factors). Of particular interest, in our opinion, is the directed flow of fluid in the eyeball induced by the pressure gradient.

The aim of this work was to study the influence of the directed fluid flow on the morphofunctional state of human fibroblasts.

A device has been designed for the *in vitro* modeling of the flow of a nutrient medium similar to the fluid flow in the eyeball. The device is a closed system with a chamber equipped with a semipermeable filter. The system was first filled with the nutrient medium with the aid of a vessel. The nutrient medium contained 200.0 ml of the DMEM nutrient medium in the Iscove modification and the 4% gentamicin solution (0.02 ml gentamicin per 10.0 ml of

Received: 26 June 2012 / Accepted: 8 October 2012

ISSN 2241-0503

the nutrient medium). For the study, we used the fibroblast culture of human lung after 3 to 4 passages in a concentration of $5 \cdot 10^4$ cells/ml.

The cellular material came to the chamber through a valve hole. The chamber was connected to the vessel containing the nutrient medium through a roller pump equipped with a maintaining valve.

The roller pump generated the uniform directed flow of the nutrient medium with a rate of 2.1-2.4 mm^3/min. The primary culture was incubated in the permanent flow of the nutrient medium under the cultivation conditions kept unchanged for 24 and 48 h. For control purposes, fibroblasts were cultivated on a semipermeable filter placed in a Petri dish with the nutrient medium at the strict observance of temperature conditions (37° C), CO_2 content (5-7%), and the humidity level (100%).

The cellular material was examined by cytochemical methods.

At the flow cultivation of fibroblasts, the following results were obtained.

Twenty four hours after the beginning of the experiment, the cytochemical analysis revealed the moderate activity of α-naphtylacetatesterase (22.56+/-0.90) and alkaline phosphatase (10.23+/-1.05) in cultivated cells. The area of the cell surface averaged 238.94+/-5.36.

Forty eight hours later, the activity of the both ferments in the described cells increased compared to the initial indices and to cells cultivated under standard conditions ($p_Z<0.01$). In this case, the level of α-naphtylacetatesterase was 26.98+/-0.87, while that of alkaline phosphatase was 14.67+/-1.21. The area of cell surface of fibroblasts averaged 179.43+/-7.81 ($p_Z<0.001$).

When fibroblasts were cultivated under standard (stationary) conditions, in the entire series of experiments the cytochemical analysis revealed the low activity of α-naphtylacetatesterase in cells. This activity increased gradually during the cultivation ($p_Z<0.05$). No alkaline phosphatase was observed in cultivated cells. The area of cell surface was 307.19+/-6.02 24 h later and 211.66+/-5.29 ($p_Z<0.001$) 48 h later.

The utmost discovery of the 19th century – the discovery of a cell in a living organism – stimulated the intense study of various pathologies from the position of the cellular structure of organs and tissues. R. Virchow in his classical paper "Die cellular Pathologie in ihrer Begrundung auf physiologische und pathologische Gewebelehre", systematizing voluminous experimental data, for the first time presented a complex organism as a system of cell or a "cell nation."

However, during the whole era of optical microscopy in morphology, a cell was thought to be a so stable component of a tissue and organ structure that its functional and morphological changes observable in an optical microscope seemed to be not related to the dynamics of cellular structures. The idea of a cell as a versatile and unchangeable unit of tissues and organs dominated.

Only new methods of morphological investigations, first of all, electronic microscopy, changed radically the idea of a cell and dynamics of its changes. The cell culture technique, which allows cells to be studied in their living state, actual action, and interaction with the microenvironment, has helped significantly in the understanding of the integration and interpenetration of the structure and functions. Intracellular structures and biochemical processes occurring in them, as well as the permanent energy flow in a cell are in a deep and close relation with each other, and together they complete the integral pattern of the united structural-functional system, namely, a cell.

One of the main functions of the cell surface and the plasmatic membrane is the perception and transfer of external regulatory signals into a cell. Just this function is responsible, to a great extent, for the interaction between the function of the cell membrane, its permeability, and the activity of intracellular metabolism processes. Now a significant progress is achieved in the understanding of molecular mechanisms of information reception, processing, and transfer from the plasmalemma to intracellular organelles. It is established that modulating factors of the extracellular medium act as exogenous regulatory signals contacting with receptors of the cell surface. Under the conditions of our experiments, the permanent directed flow of the nutrient medium and the extracellular matrix can be such an exogenous signal for fibroblasts adhesed to the filter.

We can assume that after the interaction of the external signal with cell receptors, a cascade mechanism of certain intracellular processes is initiated. Thus, for example, changes occur in the structure of receptor-related membrane ferments, which catalyze the synthesis of endogenous regulatory molecules. As a result, their concentration changes, and the cell permeability changes too. Variations of the membrane potential also play an important role.

It should be emphasized that the plasmatic membrane not only serves a mechanic barrier, but also regulates the consecutive income of substances to a cell. Diffusion into tissue complies with Fick's law that reads as follows: as soon as differences in concentration of one or another substance appear in the medium, there is a flux of this substance leading to decrease in its concentration, which is proportionate to the concentration gradient.

This equation applies to describe movement of molecules as well as microparticles if their concentration is small.

Liposoluble low-molecular substances, first of all oxygen and carbon dioxide – also penetrate easily through endothelial cells.

All macromolecules, such as proteins, nucleic acids, polysaccharides, and lipoproteid complexes, come to a cell through the vesicle formation and joining process, that is, endocytosis. The higher is the speed of the directed fluid flow through a cell, the more intense is the endocytosis process, and, correspondingly, the greater amount of substances comes into the cell. This, in its turn, determines the degree of the metabolic activity of the cell, which is confirmed by the results of fibroblast cultivation under the flow conditions.

The speed of the movement of water molecules inside the cell is also caused by physical forces: gradients of the osmotic and hydraulic pressures on the both sides of a cell. The higher the gradient, the faster is the intracellular motion of water molecules and, correspondingly, transport vesicles, which transport nonliposoluble substances, moving from one compartment to other.

The directed movement of transport vesicles results in the reconstruction of cellular compartments and the cell surface, as well as the retention or destruction of intercellular units. One can assume that the content and components of the donor compartment would ultimately disappear in the process of transportation and the donor compartment (endoplasmic reticulum in this case) would decrease in size, while the size of the acceptor (Golgi complex) would, correspondingly, increase. However, this does not occur, because in the cell there homeostatic mechanisms, regulating and maintaining the composition of every organelle, for example, with the aid of the membrane return mechanism. As transport vesicles of the endoplasmic reticulum fuse with the acceptor membranes of the Golgi complex, certain proteins return from the Golgi back to the endoplasmic reticulum. This process is known as a retrograde transport. In contrast to it, at the anterograde transport, proteins continue to move along the secretory pathway, namely, intercisterna coated vesicles transport them through cisternae of the Golgi complex.

At the most part of the Golgi trans-network, proteins are sorted, and, leaving this compartment, they are distributed over primary lysosomes, constitutive vesicles, and secretory granules depending on their designation: in the plasma membrane, in the cell, or outside.

In addition, from indices of intracellular metabolism, it is possible to judge the state of cells and the direction and intensity of their activity. Thus, for example, every stage of differentiation is intimately connected with the activation of additional ferment systems and the formation of new biosynthesis mechanisms. The data of cytochemical investigations of fibroblasts cultivated under the flow conditions compared to indices under the stationary conditions indicate that the activity of both specific (alkaline phosphatase) and nonspecific (α-naphtylacetatesterase) ferment systems increases, which is indicative of the acceleration of the cell differentiation process. This is confirmed by the more significant (compared to the stationary case) decrease in the area of cell surface of fibroblasts cultivated under the flow conditions as a reflection of the degree of fibroblast mature.

Thus, at the cultivation of human fibroblasts *in vitro* under the conditions of the directed nutrient flow, the increased intracellular fermentative activity of fibroblasts is observed. Under the modulating influence of microenvironment factors (directed fluid flow, extracellular matrix), the process of cell differentiation into mature forms accelerates.

The data obtained extend the idea of the microenvironment influence on the morphofunctional state of cells of a fibroblast population and allow cellular mechanisms of development of fibrovascular proliferation in the eyeball to be studied from new positions.

Chaotic Modeling and Simulation (CMSIM) 2: 323-334 , 2013

Spatiotemporal Chaos due to Spiral Waves Core Expansion

H. Sabbagh

American University of Iraq
E-mail: leosabbagh@excite.com

Abstract: In the framework of the Fitzhugh Nagumo kinetics and the oscillatory recovery in excitable media, we present a new type of meandering of the spiral waves, which leads to spiral break up and spatiotemporal chaos. The tip of the spiral follows an outward spiral-like trajectory and the spiral core expands in time. This type of destabilization of simple rotation is attributed to the effects of curvature and the wave-fronts interactions in the case of oscillatory damped recovery to the rest state. This model offers a new route to and caricature for cardiac fibrillation.

Keywords: Spiral break up, spatiotemporal chaos.

1. Introduction

Rotating spiral waves are ubiquitous in excitable media. They have been observed in chemical reactive solutions [1, 2], in slime-mold aggregates [3] and most importantly in cardiac muscle [4].Such wave patterns have been studied using reaction-diffusion equations models. For some values of the system control parameters, they undergo simple rigid rotation around a circular core. However, as the control parameter is varied, the spiral tip deviates from circular trajectories [5-11]. This non-steady rotation is known as meandering and it has been observed essentially in chemical systems such as in the Belouzov-Zhabotinsky (BZ) reaction [12]. Experiments with this reaction have also demonstrated spiral breakup [13, 14]. This later is of interest in cardiology since it is the prelude to cardiac fibrillation, the commonest cause of sudden cardiac death [15, 16], and has been observed in models that show wave trains spatiotemporal instabilities [17-18]. It is characterized by spatiotemporally chaotic or irregular wave patterns in excitable media and remains a challenging problem in nonlinear science.

We present in this paper a new type of meandering leading to spiral breakup and offering a new route to spatiotemporal irregularity or chaos in excitable media. Spiral core expansion occurs here as the spiral free end or tip follows an outward motion along a path that looks itself like a spiral. This core expansion was previously expected by the theory of non-local effects [6, 9, 10], and was

Received: 5 April 2012 / Accepted: 7 October 2012

ISSN 2241-0503

attributed to effect of curvature on the velocity of propagation coupled to the effects of the interaction of successive wave-fronts due to refractoriness. The dependence of the normal velocity of propagation on curvature is given by $v = v_0 - kD$, where k is the local curvature, D is the diffusion coefficient and v_0 is the plane wave velocity of propagation [11]. Due to this velocity gradient, small wavelength perturbations on the segments away from the tip would decay, which would stabilize wave propagation away from the tip and maintains the rotational motion of the spiral. On the contrary, perturbations straightening a small segment containing the tip would reduce curvature, and consequently the normal velocity of wave propagation is enhanced as the gradient of the normal velocity becomes weaker. This means that the tip would have a less tendency to curl but it tends to advance further. Therefore, further straightening of this segment containing the tip is expected. Thus, the spiral tip undergoes an outward forward motion instead of simple rigid rotation. If the recovery is non-oscillatory but monotonic, this destabilizing effect of curvature would be counteracted by the repulsive wave-front interaction due to the refractory period imposed on the medium after the passage of the preceding wave. In that case, circular rigid rotation would be sustained.

This outward motion of the tip along a spiraling trajectory was predicted by Ehud Meron in his theory of non-local effects [6, 10]. He proposed an approximate spiral wave solution of the reaction diffusion system in the form of a superposition of solitary wave-fronts parallel to each other, and then derived an evolution equation using a singular perturbation approach. The numerical solution of this equation, for the case of an oscillatory recovering excitable medium, was a spiral wave whose core expands in time and whose tip moves itself along a spiraling path. However, no observation of this type of spiral wave meandering and core expansion was obtained by Meron in reaction diffusion systems.

2. The Model

Here, we present a new model showing for the first time this predicted core expansion. We use a modified Barkley's model [19, 20] given by:

$$\partial u/\partial t = \frac{1}{£} u(1-u)[u-((b+v)/a)] + \nabla^2 u \,,$$
$$\partial v/\partial t = u^3 - v \,, \qquad (1)$$

where u and v are the excitation and recovery variables respectively. The parameter b determines the excitation threshold. The inverse of $£$, characterizing the abruptness of excitation, determines the recovery time. In the standard Barkley's model where the local kinetics in the second equation is given by $(u-v)$, propagation cannot be maintained upon increasing $£$. Here propagation is maintained due to the delay in the production of v.

Numerical simulations were performed on square grids using the explicit Euler integration method with a 9-point neighborhood of the Laplacian and no-flux boundary conditions. The space and time steps are respectively dx = 0.51 and dt = 0.052.

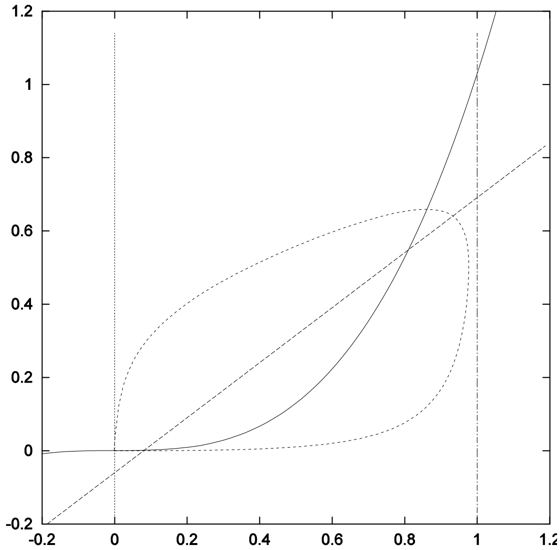

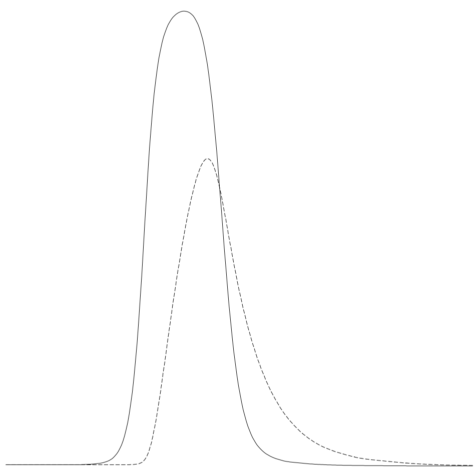

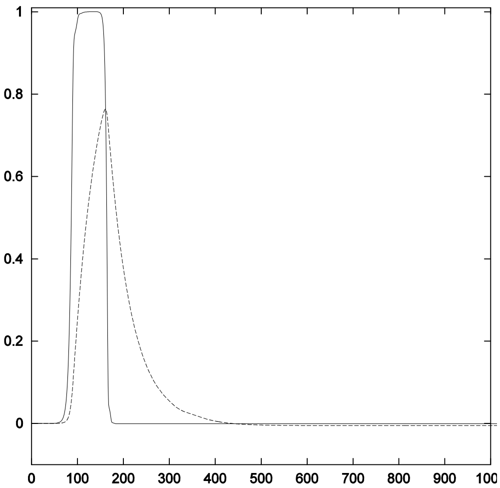

Fig. 1. (a) Phase diagram illustrating the dynamics of the PDE-system with u and v recorded at the point (40,40) in a grid size of 220. Parameters: a =0.75, b = 0.06, $£^{-1} = 13.5$. Shown are the nullclines: $v = u^3$, $u = u_{th}$, $u = 0$, and $u = 1$. (b) The time variation of u and v corresponding to one excursion along the phase diagram in (a).(c) The time variation of u and v in the standard model.

Fig. 1(a) illustrates the nullclines.The time signals of the two variables when the threshold of excitation is exceeded are shown in Fig. 1(b). In the standard Barkley's model where the local kinetics in the second equation of (1) is given by $(u - v)$, propagation cannot be maintained upon increasing £. Here propagation is maintained due to the delay in the production of v as shown in Fig. 1(b), compared to the production of v or the time at which v starts increasing in the standard model as shown in Fig. 1(c). Also the rate of recovery of the medium is made slower (in Fig. 1(b)) compared to rate of recovery in the standard model where u goes to zero more rapidly (in Fig. 1(c)).

A spiral wave was initiated using the coarse gradient cross-field method, that is by setting u = 0 in the left half of the medium and u = 1 in the right half; v = a/2 in the upper half and v = 0 in the lower half. The subsequent evolution of the system at different times is shown in snapshots in Fig. 2. The simple rigid rotation of the spiral is destabilized because of the relatively high value of £. The spiral tip defined as the intersection of the two isolines u = 0.5 and v = 0.5u – b, starts meandering, the spiral core expands as shown in Fig. 2, and the tip follows an outward motion along a spiraling path as shown in Fig. 3(a). The type of meandering is different for a different value of £ in Fig. 3(b). The meandering shown in Fig. 3(a) offers a demonstration that agrees with the

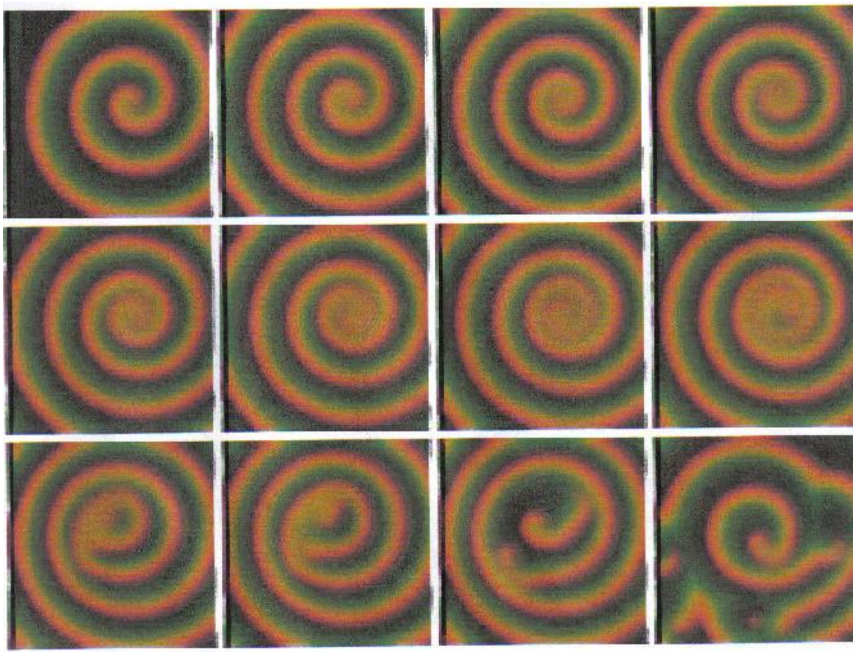

Fig. 2. Snapshots showing the core expansion with dt = 0.052, dx = 0.51, L = 48, grid size: 95. (Time intervals between snapshots are not equal).

prediction of the theory of non-local effects by Meron in the case of oscillatory recovery in excitable media. The type of recovery actually depends on the value of the control parameter £ . For low values of £ , perturbations near the spiral core are quenched by repulsive wave-fronts interactions in the monotonically recovering medium. If the value of £ is increased and for appropriate values for the other parameters, the tip undergoes this interesting outward motion along a path that looks like a spiral while the core grows in size due to oscillatory recovery to the resting state. The distance between the tip segment and the one ahead of it is determined by one of the maxima of the oscillatory tail. This corresponds to one of the minima of the excitation threshold.

In Fig. 3(a), the distance between the points denoting the tip positions increases as the tip moves outward implying that the tip motion is accelerated. In Fig.2, the spiral core expands until spiral breakup occurs. This happens because the spiral period changes as the spiral drifts and meanders, until at some point within the excitable medium, it reaches the minimum period needed for plane wave propagation. This change in the spiral period as the tip moves outward and forward is due to Doppler shift since the core is seen as the source of waves. This means that conduction would be blocked since the spiral rotates more rapidly than plane waves can propagate when the spiral period and the minimum period compatible with plane wave propagation merge for this critical value of

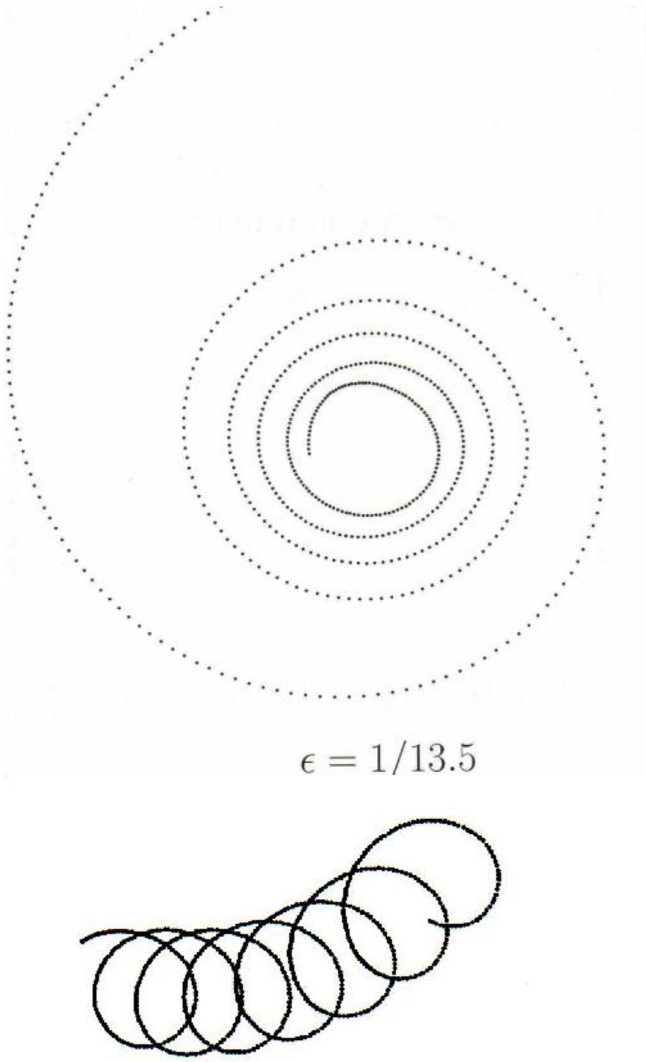

Fig. 3. Trajectory of the spiral tip defined as the intersection of the isolines u = v = 0.5, and following an outward spiral trajectory in (a) and meandering in (b). Parameters are the same as in Fig. 1 in (a), and in (b) $£^{-1} = 18.0$.

£ [22]. The spiral becomes unstable and breaks into newly born broken waves which will soon evolve into spirals waves since they have broken ends. This leads to spatiotemporal chaos or irregularity within the excitable medium as shown in Fig.4 where the time variations of the excitatory and the recovery

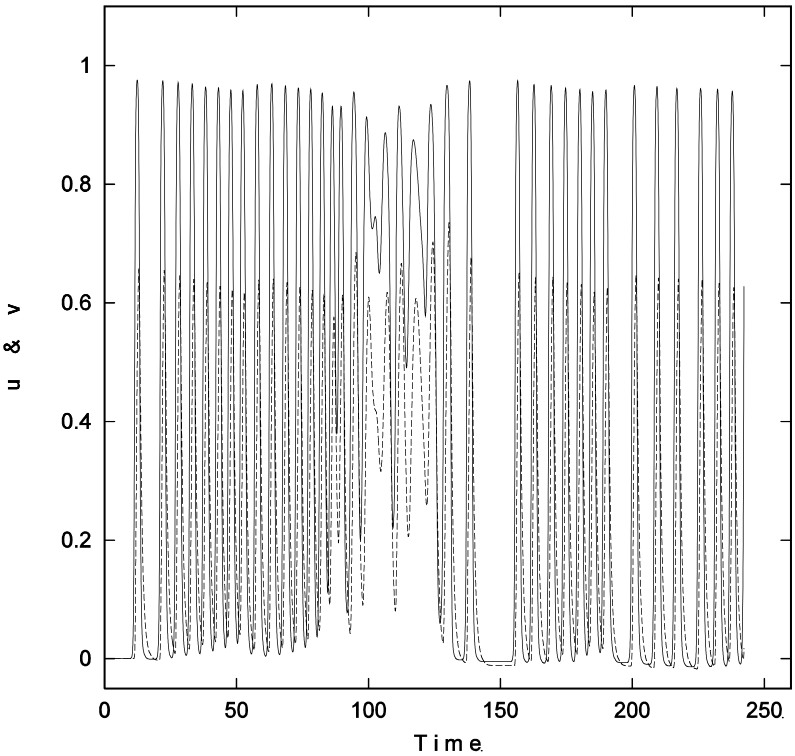

Fig. 4 Time variation of the excitatory and the recovery variable recorded in the medium at the location (10,10). The dotted one is the variation of v.

variables are recorded at point (10,10) in the excitable medium of size L = 100. This phenomenon can be attributed to an unstable focus by considering a traveling wave solution of (1), $u(z) = u(x+ct)$ where c is the wave speed. Substituting this solution into (1) reduces the reaction-diffusion equations to the following ODE system:

$$dw/dt = cw - (1/£)u(1-u)[u - ((b+v)/a)]$$

$$du/dt = w$$

$$dv/dt = (1/c)(u^3 - v)\,, \qquad (2)$$

Using parameter values a=0.75 and b=0.06, $£^{-1} = 13.5$, the numerical solution shown in Fig.5 approaches the resting state in an oscillatory manner. For those values of the parameter, the system can have complex eigenvalues implying that the fixed point (0,0,0) is an unstable focus for $c^2 - 4.32 < 0$. This condition is satisfied for some range of the spiral period as it can be seen in the dispersion

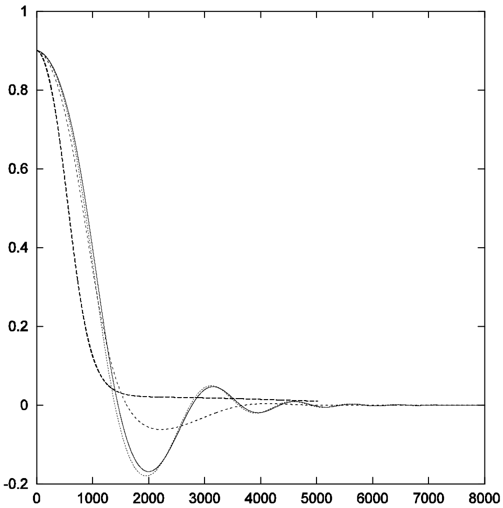

Fig. 5. Recovering solitary traveling solution u(z)=u(x+ct) of Eqs.(2), illustrating damped oscillatory ($£^{-1} = 13.5$, 14.5) and monotonic recovery ($£^{-1} = 20.0$, 50.0).

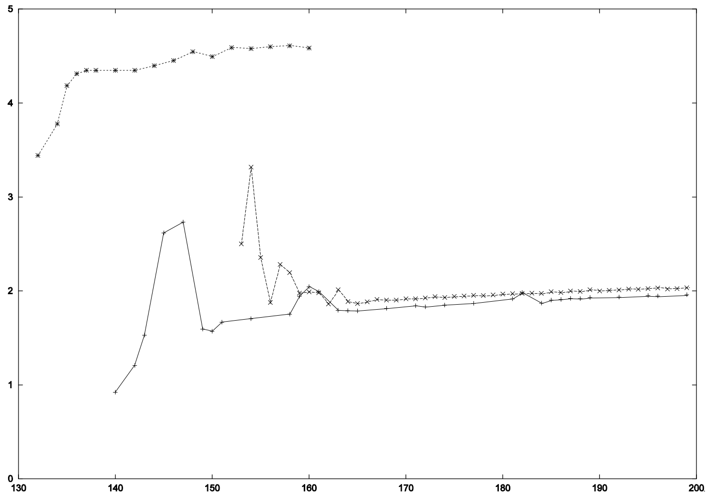

Fig. 6. Dispersion curve: Instantaneous wave speed as a function of period for $£^{-1} = 13.5$, 14.5, 50.0 respectively from bottom to top, computed by repetitively stimulating at one of the ends of an open line.

curve in Fig. 6. That justifies the oscillatory behavior of the numerical solution of (2). For other values of the parameter £ , the solution approaches the resting state (0,0,0) in a non-oscillatory manner if $£^{-1} = 50.0$ for which the spiral rotates rigidly around a circular core. If $£^{-1} = 20.0$, the recovery is also monotonic, but that does not necessarily imply rigid rotation. Actually, the spiral tip meanders following an epicycle-like orbit as shown in Fig. 3(b). On the other hand, if $£^{-1} = 13.5$ or $£^{-1} = 14.5$, the solution returns to the resting state in an oscillatory manner as seen in Fig. 5; the system undergoes a succession of super and subnormal periods until complete recovery is achieved. However, for $£^{-1} = 14.5$, unlike the case for $£^{-1} = 13.5$ (shown in Fig. 3(a) and Fig. 2) and despite the oscillatory type of recovery, core expansion does not occur and the tip does not follow an outward spiraling trajectory. It traces loops like those of an epicycle as the spiral wave rotates and drifts away. Actually, we found that the tip moves along a spiraling path in the range 13.0< $£^{-1}$ <13.8. For $£^{-1}$ >13.9, it meanders but not along a spiraling trajectory. Thus, we note the important conclusion that oscillatory recovery does not necessarily lead to core expansion and spiraling tip.

This oscillatory recovery can be further investigated by writing the solution of the reaction-diffusion system as a superposition of two solitary waves with a small perturbation term R which vanishes in the limit of infinite spacing between the two waves:

$$u(z) = u(z - z_1) + u(z - z_2) + R \qquad (3),$$

where $z_1 = x_1 - ct$ and $z_2 = x_2 - ct$, x_1 and x_2 denote the waves positions. For large $|z_1|$ and $|z_2|$, the tail of the wave determines the manner in which the medium recovers to the resting state is: When the recovery is damped oscillatory, the tail of the wave $u(z) \propto e^{¦ z} \cos(¬z + ·)$; when it is monotonic, $u(z) \propto e^{¦ z}$. In both cases, the leading edge of the wave is assumed to be of the form $u(z) \propto e^{-« z}$. Equations for x_1 and x_2 are derived using the solvability conditions which remove singularities from R [21]:

$$\frac{¢x_1}{¢t} = c + a_R e^{-«(x_1 - x_2)} \qquad (4)$$

$$\frac{¢x_2}{¢t} = c + a_L e^{-¦(x_1 - x_2)} \cos(¬(x_1 - x_2) + ·) \qquad (5),$$

where c is the propagation speed of a solitary wave. The second term on the right hand side of (4) represents the effect of the second wave on the propagation of the first one. It is usually negligible in excitable media. The second term on the right hand side of (5) represents the effect exerted on the second wave by the refractory wake of the first one. Using (4) and (5), the spacing between the two waves $a = x_1 - x_2$ obeys the equation:

$$\frac{d\alpha}{dt} = a_L e^{-\lambda\alpha}\cos(\nu\alpha + \phi) \qquad (6).$$

If $\nu \neq 0$, the excitable medium recovers in an oscillatory way. Then, according to (6) an infinite number of steady state solutions exist. This means that the distance between the wave-fronts takes one of possible fixed values.

Those oscillations in the way of recovery to the resting state would imply oscillations in the dispersion. This is shown here by considering the times when wave-fronts pass through a given location x. The solution of (5) is then approximated by widely spaced impulses:

$$u(x,t_i) = \sum_k u_k(t_i(x)) + R, \qquad (7)$$

where $t_i(x)$ is the instant at which the ith impulse is at x, and R is a small perturbation term which vanishes in the limit of infinite spacing between the waves. Using (7) in (1), we get

$$dt_i/dx = (1/c_0) + a' e^{\lambda(t_i - t_{i-1})}\cos[v(t_i - t_{i-1}) + \phi] + b' e^{-\eta(t_{i+1} - t_i)}$$

(8)

where η is the rate at which the wave-fronts tail off. The second term on the right hand side of (8) represents the effect exerted on the ith impulse by the refractory wake of the preceding impulse. The last term represents the effect of the succeeding impulse and is negligible in excitable media. The coefficients a' and b' require the evaluation of certain integrals which are not shown here. Let $t_i(x) = (x/c) + (i-1)T$, where T is the period of a constant speed wave-train. Then we get to leading order,

$$c = c_0 - c_0^2 a' e^{-\lambda T}\cos[\nu T + \phi] \qquad (9)$$

For $\nu \neq 0$ in (9), damped oscillations occur in the dispersion curve. For monotonic recovery ($\nu = 0$, $a>0$), the wave speed is a monotonic increasing function of wave spacing. If $\nu = 0$ and $a<0$, the recovery is said to be non-monotonic and could exhibit one supernormal period [10, 19]. In Fig. 6, there are damped oscillations in dispersion curve of the system (1) for $\varepsilon^{-1} = 13.5$ and $\varepsilon^{-1} = 14.5$. The first supernormal period during which the excitability is higher than that of the rest state is very pronounced. However, for $\varepsilon^{-1} = 50.0$, as expected, the monotonically recovering system is characterized by a dispersion curve with monotonic increase in the propagation velocity until the limit set by the solitary wave velocity is reached.

3. Conclusions

This oscillatory behavior and the occurrence of supernormal periods in the dispersion curve were observed in wave train solutions of the one-dimensional FitzHugh-Nagumo model [23]. But, no core expansion has ever been reported before. Also, the observation of expanding cores and spiraling tips here answers the query of Meron [6, 9, 10] and Winfree [24, 25] about the possible observation of core expansion and oscillations in the dispersion curve. Using FitzHugh-Nagumo kinetics with parameters chosen such that the equilibrium point is nearly a center, Winfree showed that the medium can then support two stable rotors of different periods. The dispersion curve exhibited a damped oscillatory behavior. However, core expansion was not observed, and meandering along a spiraling path was not obtained.

This occurrence of 'supernormal' periods of excitability during which the threshold of excitation is diminished was reported in electrophysiological measurements in stimulated cardiac muscle [26]. The current that was needed to re-excite the Purkinje fibers was reduced. We could attribute it to the faster recovery of the threshold potential compared to the slower recovery of the action potential that we have seen here. We have also verified that than a smaller additional depolarization is needed to reach the threshold potential and it was brought about by a weaker depolarizing current.

Our results would imply that core expansion could be one possible route to spiral breakup.

References

1. Kapral R and Showalter K(eds) *Chemical Waves and Patterns* (Dordrecht: Kluwer), 1994
2. Imbihl, R. and Ertl, G., *Chem. Rev.* **95,** 697 (1995)
3. Murray, J. *Mathematical Biology* (Berlin: Springer), 1989
4. Chaos Special Issue on Dynamics in Cardiac Tissue 2002 *Chaos* **12** 3
5. A. T. Winfree, When Time Breaks Down (Princeton Univ. Press, New Jersey, 1987)
6. E. Meron in: A.V. Holden et al. (Eds.), Nonlinear Wave Processes in Excitable Media, Plenum, 1991, pp. 145-153.
7. V. S. Zykov, Biophysics 31 (5) (1986) 940
8. V. S. Zykov, Biophysics 32 (2) (1987) 365
9. E. Meron, Phys. Rev. Lett. 63 (1989) 684
10. E. Meron, Physica D 49 (1991) 98
11. J. J. Tyson and J.P. Keener, Physica D 32 (1988) 327
12. V. S. Zykov, O. Steinbock and S.C. Muller, *Chaos* **4 (3)**, 509-518 (1994)
13. Nagy-Ungvarai, Zs. And Muller, S.C., *Int. J. Bifurc. Chaos* 4: 1257-1264 (1994)
14. Markus, M. and Stavridis, K., *Int. J. Bifurc. Chaos* 4: 1233-1243 (1994)
15. Panfilov, A. V. and Hogeweg, P., *Science* 270: 1223-1224 (1995)
16. Winfree, A. T., *Science* 266: 1003-1006 (1994)
17. Karma, A., *Chaos* 4: 461-472 (1994)
18. Courtemanche, M., Glass, L. and Kenner, J. P., *Phys. Rev. Lett.* 70: 2182-2185 (1993)
19. D. Barkley, Physica D 49 (1991) 61.
20. D. Barkley, M. Kness, L.S. Tuckerman, Phys. Rev. A 42 (1990) 2489.
21. C. Elphick, E. Meron, J. Rinzel, and E. A. Spiegel, J. Theor. Biol. 146 (1990) 249.
22. H. Sabbagh, Chaos Solitons & Fractals 11 (2000) 2141.
23. J. Rinzel, K. Maginu in: C. Vidal, A. Pacault (Eds.) Nonequilibrium Dynamics in Chemical Systems, Springer- Verlag, 1984, pp. 107-113.

24. A.T. Winfree, Physica D 49 (1991) 125.
25. A.T. Winfree, Phys. Lett. A 149 (1990) 203.
26. J.F. Spear, E.N. Moore, Circ. Res. 35 (1974) 782.

Chaotic Modeling and Simulation (CMSIM) 2: 335-348, 2013

Nanoindentation for Measuring Individual Phase Mechanical Properties of Sn-Ag-Cu Lead-Free Solders Incorporating Pileup Effects

Muhammad Sadiq, [1,2,3,5], Jean-Sebastien Lecomte, [4], Mohammed Cherkaoui, [1,2,3]

[1] George W. Woodruff School of Mechanical Engineering, Georgia Institute of Technology, 801 Ferst Drive NW, Atlanta, GA 30332, USA
[2] University of Lorraine, LEM3 UMR CNRS 7239, île du Saulcy, Metz 57045 France
[3] UMI 2958-Georgia Tech-CNRS Georgia Tech Lorraine, Metz 57070, France
[4] ENSAM-Arts et Métiers ParisTech, LEM3 UMR CNRS 7239, 4 rue Augustin Fresnel, Metz 57078 France
[5] msadiq3@gatech.edu

Abstract: Sn-Ag-Cu (SAC) alloys are considered as the best replacements of Sn-Pb alloys which are banned due to the toxic nature of Pb. But, SAC alloys have a coarse microstructure that consists of β-Sn rich and eutectic phases. Nanoindentation is a useful technique to evaluate the mechanical properties at very small length scale. In this work, CSM nanoindentation setup is used to determine the individual phase mechanical properties like Young's modulus and hardness at high temperatures. It is demonstrated that these properties are a function of temperature for both β-Sn rich and eutectic phases. Loadings starting from 500 µN upto 5000 µN are used with 500 µN steps and average values are presented for Young's modulus and hardness. The loading rates applied are twice that of the loadings. High temperatures results in a higher creep deformation and therefore, to avoid it, different dwell times are used at peak loads. The special pileup effect, which is more significant at elevated temperatures, is determined and incorporated into the results. A better agreement is found with the previous studies.

Keywords: SAC alloys, Nanoindentation, Young's modulus, Hardness, Pileup effects

1. Introduction

Good set of entire mechanical, electrical, chemical and thermal properties are the key elements before classifying any solder to be good for current solder joints. All of these properties were well set for Sn-Pb solder until no restrictions were taken by RoHS and Environmental Protection Agency (EPA), which identified Pb as toxic to both environment and health. This is because Pb and Pb-containing compounds, as cited by EPA, is one of the top 17 chemicals posing the greatest threat to human beings and the environment [1]. Moreover,

Received: 14 April 2012 / Accepted: 28 September 2012

ISSN 2241-0503

current consumer demands and strict governmental legislations [2-4] are pushing the electronics industry towards lead-free solders.

Many lead-free solder alloys are studied by different researchers with wide range of applications. In Abtew's report [2], almost 70 lead-free solders are proposed to replace their lead based counterparts. Most of the newly defined lead-free solders are binary and tertiary alloys [5], out of which, SAC tertiary alloys are considered as the best substitutes [6]. As like many other alloy systems, SAC has also certain limitation due to their coarse microstructure. Iron (Fe), cobalt (Co) and nickel (Ni) are used as potential additives to overcome these limitations [7]. In some studies, indium (In), bismuth (Bi), copper (Cu) and silver (Ag) are used as alloying elements [5]. Before classifying SAC as good substitute, extensive knowledge and understanding of the mechanical behaviour of this emerging generation of lead-free solders is required to satisfy the demands of structural reliability.

Electronic devices once subjected to severe conditions during service exposes solder joints to elevated temperatures. This causes significant evolution of the microstructure of SAC alloys. SAC alloys consists of β-Sn, eutectic Sn phases and Ag-Sn and Cu-Sn InterMetallic Compounds (IMCs). These IMCs are generally hard and brittle in nature which dictates the entire mechanical properties of the solder joints. Exposures to high temperatures causes thermal coarsening due to which the size of these IMCs grow and further deteriorate the solder joints and hence alters the structural reliability of the whole assembly. Rare-earth elements, known as the vitamins of metals, are used in different studies to control this thermal coarsening with significant results [8-11]. All these elements refine the grain size leading to a fine microstructure which ultimately improves the mechanical properties of SAC lead-free solders including yield stress and tensile strength [10-11].

The fast introduction of lead-free solders without deep knowledge of their behaviour has caused many problems in the current electronics industry. Therefore, good understanding of SAC alloys is required to explore the mechanical properties and enhance the solder joint reliability. The main focus of this work is to measure the individual phase properties like Young's modulus and hardness of SAC alloys for eutectic Sn and β-Sn phases. Many researchers have already attempted to determine the mechanical properties of Sn-Ag and SAC alloys [12-13]. The indenter causes piling up inside the soft Sn-matrix which has been neglected in many studies which makes the results unreliable. In this study, the piling up effect is considered for both phases and evaluated using semi-ellipse method and incorporated into results. Both results, before modification and after modification are provided for comparison.

2. Experimental

Solder alloy used in this study is Sn3.0Ag0.5Cu with 96.5 wt % of Sn, 3 wt % of Ag and 0.5 wt % of Cu. Since sample preparation for any kind of experimental study is crucial. Therefore a casting die is used to make the samples using "cast by melt" process with many advantages. This die gives almost final shape to the samples with minimum of final machining required.

Almost voids-free surface is achieved which is very important for the nanoindentation testing. During casting the microstructure of the testing samples is controlled using specified cooling rate which is about 3°C/s. A temperature of 260°C was kept in the oven and the die was heated for about 45 minutes before putting the molten metal into it. The 200g ingots were put in a crucible and then placed in the oven at 260°C for about 25 minutes. Water at a temperature of 15°C was used for quenching; the cooling rate of the specimens was measured with a K-type thermocouple. Only a small part of the die was dipped in the water to get a slow cooling rate of about 3°C/s, which is close to the actual soldering process. The dog-bone shape specimen is shown in Figure 1 with a thickness of 2mm.

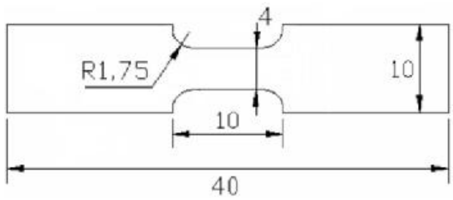

Fig. 1. Dog-bone specimen (all dimensions in mm)

Specimens were mechanical polished with silicon discs and 1 micron diamond paste. Chemical etching was performed for a few seconds using a 5% hydrochloric acid and 95% ethanol solution in order to distinguish between different phases. Figure 2 shows an SEM micrograph and Optical microscope (OM) micrograph taken before the nanoindentation. An Oxford EDS system placed in the SEM enabled to realize elemental mappings for every specimen.

Nanoindentation tests were carried out by using a nanoindenter XP equipped with a Berkovich-84 diamond indenter. The resolutions of the loading and displacement systems are 50 nN and 0.01 nm, respectively. Both of the standard deviation errors of the measured hardness and reduced modulus values for the standard are well less than 1%. The hardness value and reduced modulus values were also extracted from the unloading part of load–depth curves by using Oliver and Pharr method [14].

An acquisition frequency was 10 Hz and poison ratio, assumed, was 0.33. The load applied were 100 µN to 5000 µN with steps of 500 µN. The loading and unloading rates (mN/min) were two times that of load applied (mN). An approach speed of 3000 µN/min was used. As the lead free solders exhibit severe creep deformation, even at room temperature [15], the dwell time at the peak load is defined as 60 seconds in order to completely relieve the creep deformation and also avoid the famous “bulge” or “nose” effect during unloading [16].

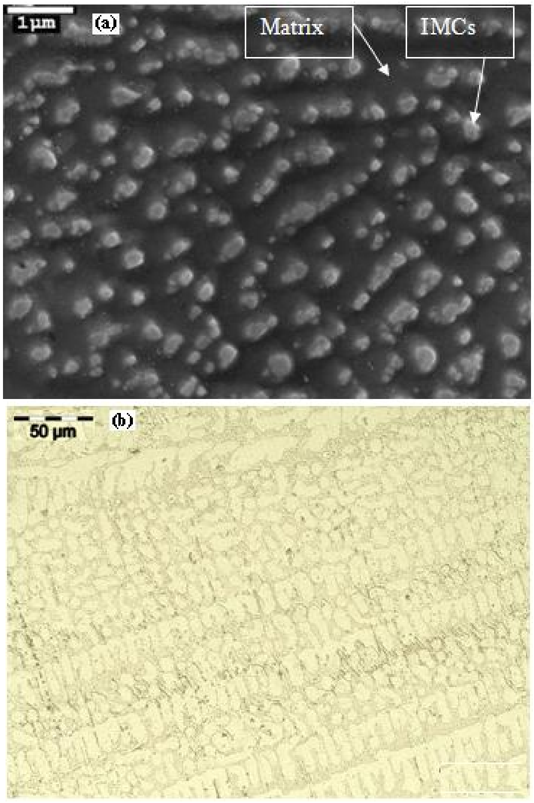

Fig. 2. (a) SEM and (b) Optical Microscope micrographs before nanoindentation

The selection of position to indent was controlled under a high-resolution Optical Microscope (OM), by which various phases can be distinguished. OM was also applied after the indentation to confirm the indenter location and avoid the grain boundary effects. For each specimen, 9 points (3X3 arrays) were tested. Both phases, eutectic and β-Sn, were selectively indented by the visual matrix method. Same tested zones were studied after the indentation testing with Atomic Force Microscope (AFM).

Afterwards, Scanning Electron Microscope (SEM) and Energy Dispersive Spectroscopy (EDS) were used to confirm the chemical composition of each phase. Further, because the Young's modules and hardness for each phase is different, curves for eutectic phase and β-Sn phase can be distinguished from the test array.

3. Results and discussion

This is well known in the nanoindentation testing that the typical load-depth curve has significant importance for extracting the overall results. Most importantly, the slope of the unloading portion of the curve is used in almost all calculations. As discussed earlier, SAC alloys are famous for their low creep resistance and hence quite vulnerable to creep, due to which the pile-up effects happens which causes the "bulge effect" in both β-Sn and eutectic-Sn phases. It is important to avoid this "bulge effect" as it may alter the credibility of final results. Different loads were tested to avoid this effect but it still exists as shown in Figure 3.

Moreover, in order to investigate the creep effects on the mechanical properties, different holding times were used. In comparison to Sn matrix, the IMCs are expected to be resistant to the creep effect. In some cases, there is some bulge effect, but it can be concluded that this is because of the Sn matrix in which these particles are finally embedded.

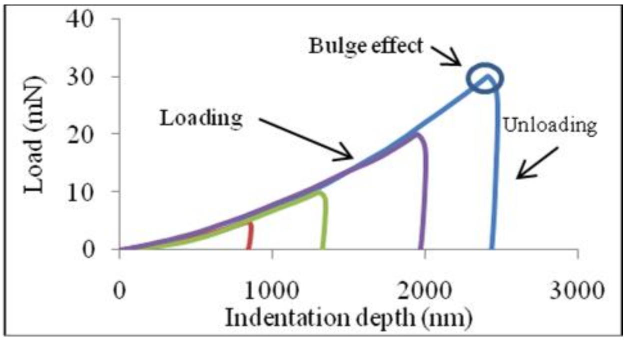

Fig. 3. Load-displacement curves with no holding time

Both β-Sn and eutectic Sn phases were subjected to indentation testing. The load-time history for the entire testing is shown in Figure 4.At a peak load of 5000μN, a 60 seconds dwell time was used to avoid the bulge effect. Solder joints are exposed to high temperatures during service. This causes thermal coarsening of IMCs, due to which, their size grows as the diffusion rate of Ag and Cu into Sn increases at elevated temperatures. It is of utmost importance to understand and explore the individual phase mechanical properties up to a homologues temperature of at least $0.4T_m$, where T_m is the melting point of SAC alloy.

The Load-Depth curves for individual phases at 20°C, 45°C and 85°C are given in Figures 5-7 respectively. In this case, the bulge effect is negligible. Quite useful information can be extracted from these curves. It is important to visualize that the elastic deformation in both phases is quite small which makes the unloading curve almost straight (vertical). Moreover, as also described by the other researchers, indentation depth in eutectic phase is significantly smaller than the β-Sn phase [15]. This effect was also confirmed when the hardness of both phases were compared, eutectic phase being harder than β-Sn phase. This could be the effect of diffusion of Ag and Cu in Sn in the eutectic zone. For confirmation of the testing zone, the tested specimens were taken under the AFM. High resolution images were collected as provided in Figure 8 for the testing performed over eutectic zone in SAC alloy. Different size of indentation represents different loadings applied during testing.

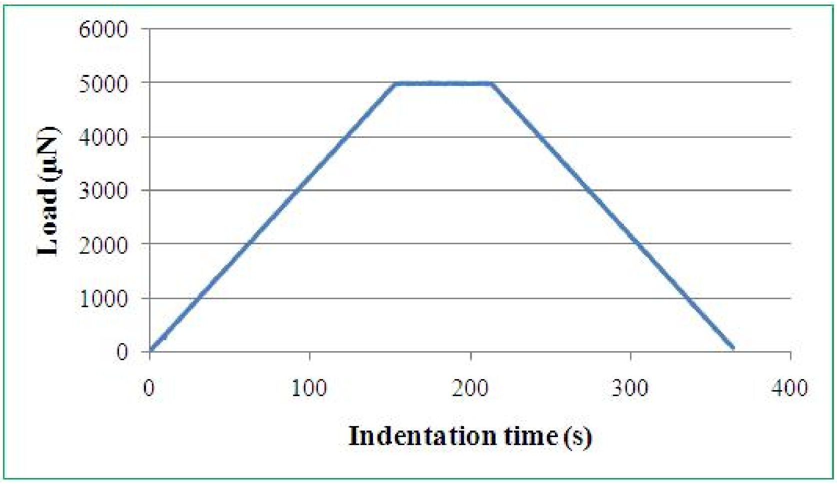

Fig. 4. Load-time history during indentation testing with 60 seconds dwell time

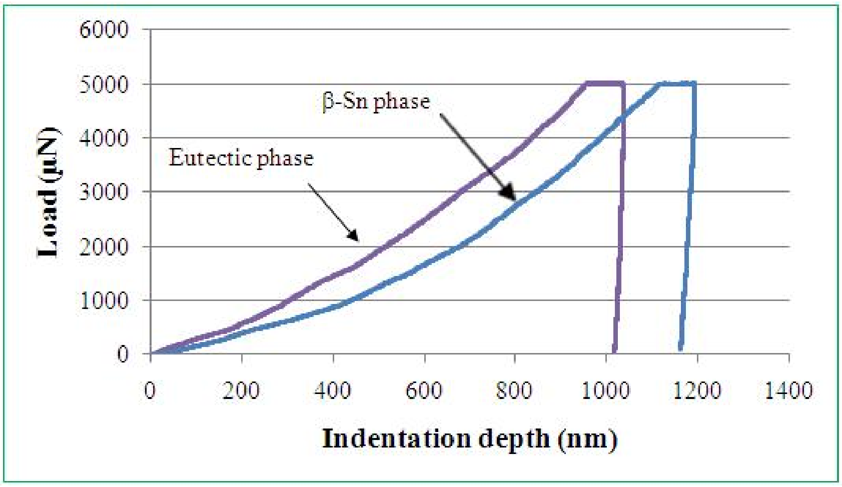

Fig. 5. Load-displacement curves for Eutectic and β-Sn phases at 20°C

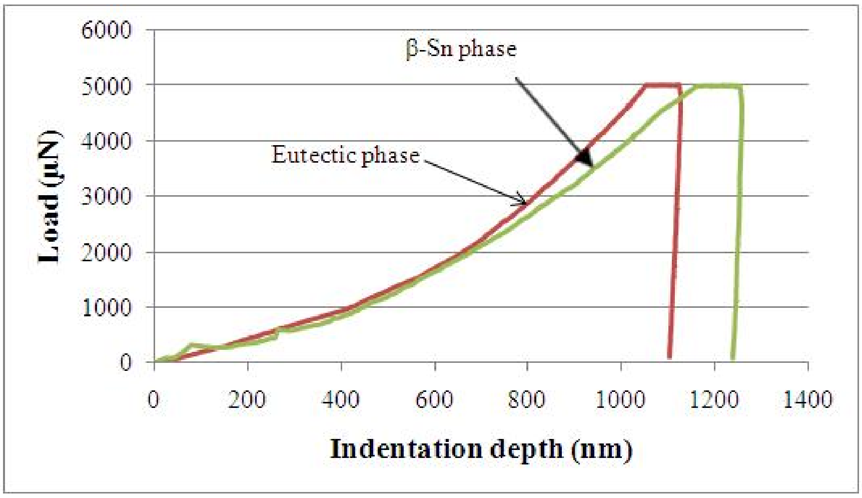

Fig. 6. Load-displacement curves for Eutectic and β-Sn phases at 45°C

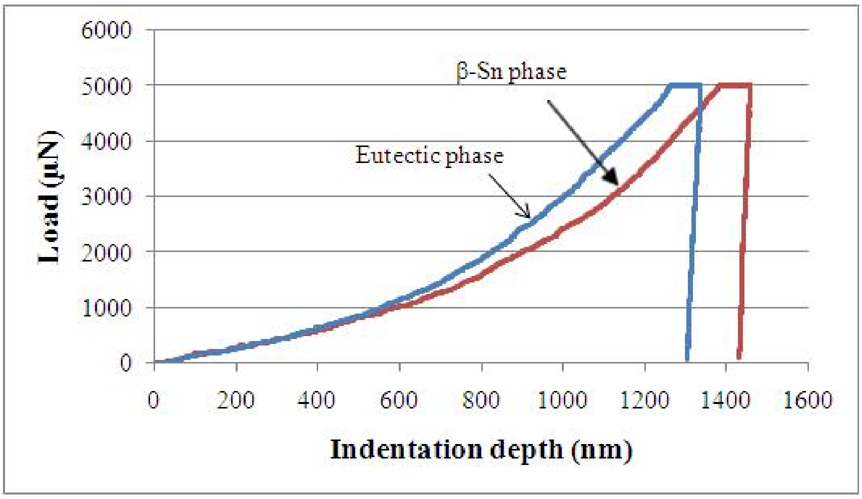

Fig. 7. Load-displacement curves for Eutectic and β-Sn phases at 85°C

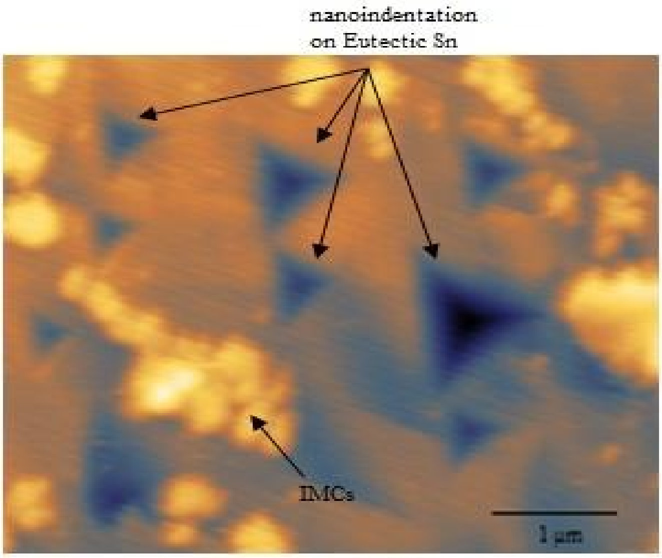

Fig. 8. AFM image after nanoindentation over eutectic zone

3. Oliver and Pharr Model

Oliver and Pharr Model (OPM) is extensively used for the solder alloys [14]. Both Young's modulus and hardness are easily extracted using OPM after calculating the reduced modulus E_r as described in equation (1),

$$\frac{1}{E_r} = \frac{\sqrt{\pi}}{2} . \frac{S}{\sqrt{A_{op}}} \text{...........(1)}$$

where S is the contact stiffness calculated from the slope of the unloading portion of the curve, β is a constant related to the geometry of the indenter, and A_{op} is the oliver-pharr area projected during indentation. At the same time, the reduced Young's modulus could be formulated as,

$$\frac{1}{E_r} = \frac{1-v^2}{E} + \frac{1-v_i{}^2}{E_i} \text{.........(2)}$$

where E and υ are the Young's modulus and Poisson's ratio of the tested material and E_i, $υ_i$ are the Young's modulus and Poisson's ratio for the diamond tip. The values of E_i and $υ_i$ used in this study were 1141 GPa and 0.07, respectively as used in most of the studies [8] and the Poisson's ratio of each phase, i.e., β-Sn and eutectic Sn phase was approximated to be 0.33 which was consistent with the previous studies [8]. Hardness (H) of the material, on the other hand, can be determined by (3) where F_{max} is the peak indentation load and A_{op} is the projected contact area

$$H = \frac{F_{max}}{Aop} \text{........(3)}$$

$$A_{op} = 24.5h_c^{\,2} + \sum_{i=1}^{8} C_i h_c^{\frac{1}{2i}} .....(4)$$

Table I. Constant “C” values for berkovich-BK indenter tip

C_0	C_1	C_2	C_3	C_4	C_5
24.5	10.31	-16.03	24.45	-7.32	5.12

where C is the constant depending on the indenter type and shape and are given in Table I for Berkovich-BK indenter tip. h_c is the contact depth which is smaller than the theoretical depth due to the sinking effect of the specimen under indenter.

Both Young’s modulus and hardness are determined and provided for eutectic and β-Sn phases in Table II. These are the results before pile-up effects. Almost no change was investigated with varying loading and loading rates. This is consistent with other studies [15].

Table II. Individual phases Young’s modulus and hardness before pileup effects

Phase	Young’s modulus (Gpa)	Hardness (Gpa)
Eutectic-Sn	60±3	0.35±0.04
β-Sn	54±4	0.30±0.045

4. Pileup area calculations

Assuming that the projected contact area, A_c, determined at contact depth, hc, traces an equilateral triangle of side b, then for a perfect Berkovich tip,

$$A_c = 24.56h_c^{\,2} \,..........(5)$$

There are semi-elliptical portions at each side of the triangle as shown in Figure 9. The area of each semi-elliptical pile-up projected contact area is $\frac{\pi b}{4} a_i$ and the total pile-up contact area is, therefore,

$$A_{pu} = \frac{\text{®} b}{4} \sum a_i ....(6)$$

where the summation is over three semi-elliptical projected pile-up lobes and a_i being the measurement of piling up width on three surface (sides) of the equilateral triangles [2]. The AFM images are analyzed in image-plus to trace the surface profiles and are given in Figure 10. Knowing then the contact area from the Oliver–Pharr method, the total or true contact area for an indent can be obtained as:

$$A = 24.5h_c^{\,2} + \sum_{i=1}^{8} C_i h_c^{\frac{1}{2i}} + \frac{\text{®} b}{4} \sum a_i .....(7)$$

Incorporating this new pileup area into the original OPM as presented in equations (1) and (3) becomes,

$$\frac{1}{E_r} = \frac{\sqrt{\text{®}}}{2} \cdot \frac{S}{\sqrt{A_{op} + A_{pu}}} ....(8)$$

$$H = \frac{F_{\max}}{A_{op} + A_{pu}} ......(9)$$

The hardness and indentation modulus measured for eutectic and β-Sn phases are shown in Table III after incorporating the pileup effects. These results are in a better agreement with the previous studies [12]. This collection of data allows for comparison of mechanical properties of different phases, where all of the samples were prepared and tested in the same manner.

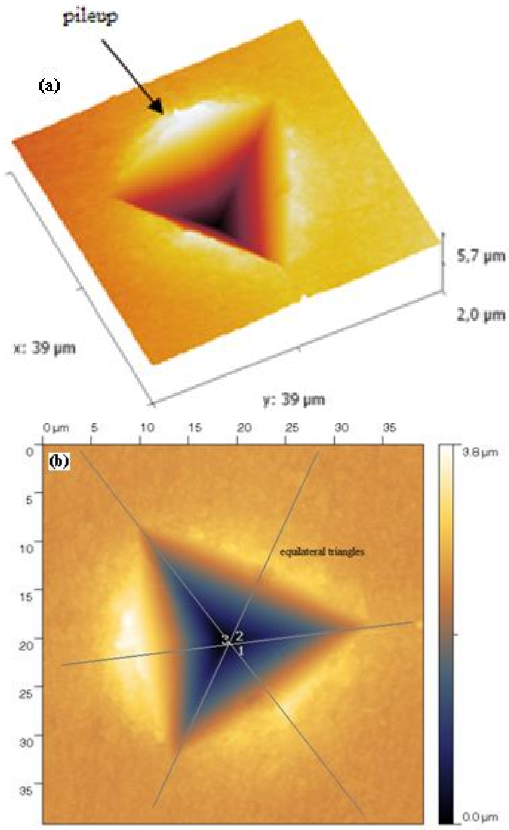

Fig. 9. (a) Pileup schematic and (b) equilateral triangles after testing

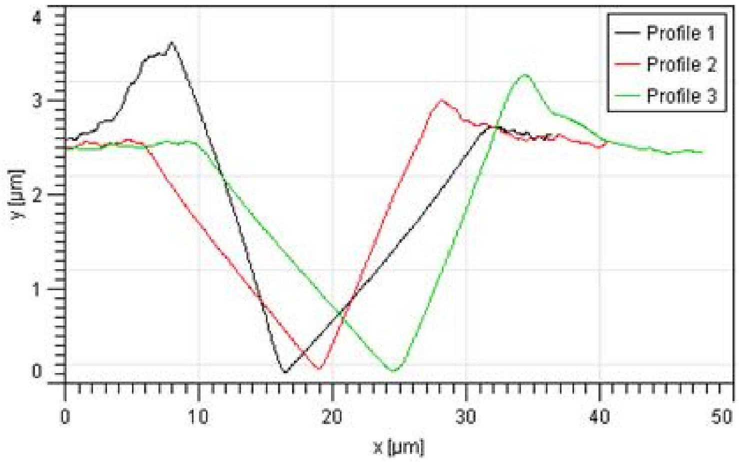

Fig. 10. Pileup profiles for equilateral triangles

Table III. Young's modulus and hardness after pileup effects

Phase	Young's modulus (Gpa)	Hardness (Gpa)
Eutectic phase	49±2	0.25±0.05
β-Sn phase	45±3	0.20±0.06

Both Young's modulus and hardness were also determined along the indentation depth with experiencing only small variations which is also consistent with [12]. The average values for the Young's modulus for eutectic phase, along the indentation depth, are determined to be 51 GPa whereas for β-Sn it is 48 GPa. Similarly, the average values for hardness, along the depth, for eutectic phase are determined to be 0.26 GPa whereas for β-Sn it is 0.22 GPa. The average values are taken from 100 nm to 500 nm depth. These values are taken after considering the pileup effects.
Similarly, summarized results for β-Sn and eutectic phases for Young's modulus and hardness at elevated temperatures are given in Tables IV-V respectively.

Table IV. Mechanical properties for β-Sn phase at different temperatures

Temperature (° C)	Young's modulus (GPa)	Hardness (GPa)
45	37.42 ±2.1	0.10 ±0.03
65	36.21 ±3.2	0.095 ± 0.025
85	34.85 ±3.5	0.087 ± 0.027

Table V. Mechanical properties for Eutectic phase at different temperatures

Temperature (°C)	**Young's modulus (GPa)**	**Hardness (GPa)**
45	42.83 ±2.7	0.19 ±0.040
65	43.72 ±2.2	0.17 ± 0.025
85	51.85 ±4.5	0.11 ± 0.027

Like the other phases of SAC alloys, the nanoindentation setup is also used for IMCs. These IMCs are hard and brittle as compare to the other phases in the same specimens. The EDS elemental mapping is used to verify the compositions of these IMCs before implementing the nanoindentation.

The AFM micrograph is given in Figure 11 in which the indentation is carried out on IMCs. These images are collected just after the indentation process. The results for Young's modulus and hardness for both Ag_3Sn and Cu_6Sn_5 IMCs are provided in Table VI, with good comparison to the previous studies [17]. This is important to mention that the pileup effect is very small for these particles which is consistent with previous studies and therefore is neglected for IMCs.

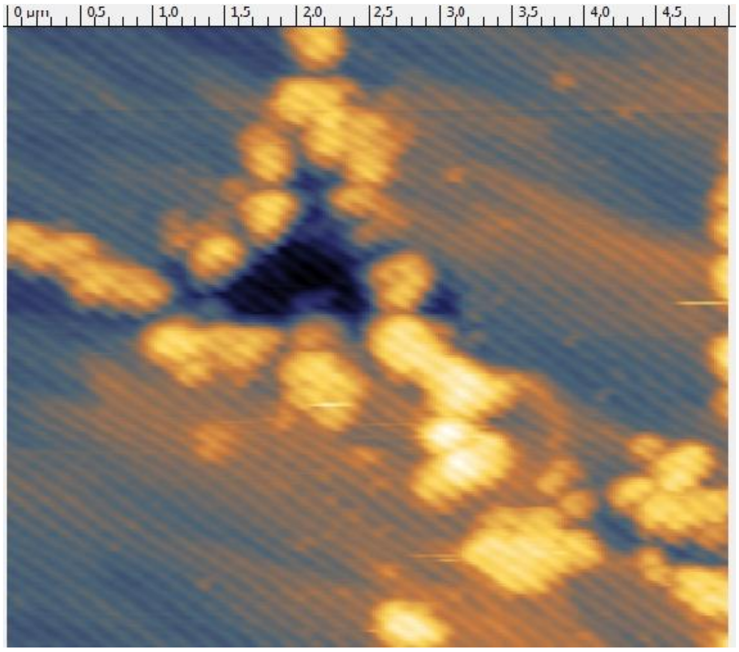

Fig. 11. AFM image for nanoindentation over IMCs

Table VI. Mechanical properties for IMCs

IMCs	Young's Modulus (GPa)	Hardness (GPa)
Ag_3Sn	74 ± 3	3.32 ± 0.2
Cu_6Sn_5	91 ± 5	5.8 ± 0.6

5. Conclusions

A detailed study was carried out to explore the individual phase mechanical properties using nanoindentation for the SAC alloy which is considered as potential substitute for SnPb solder. Varying loads and loading rates were used to avoid the typical "bulge effects" and hence make the results more reliable. Piling effect, already ignored by many researchers, is calculated and incorporated into the Oliver-Pharr model. Image-Plus software is used to treat the indentation images taken with AFM after testing and hence plot the individual surface profiles to better explain the material behaviour. It is concluded that this pileup area play a major role in calculating the real results particularly for the soft Sn phase which has more pileup than the eutectic phase. Young's modulus and hardness were also determined along the indentation depth and almost no change was observed which is consistent with previous studies. Different temperatures are used and the load-depth curves are plotted for individual phases. It is noticed that both Young's modulus and hardness reduces with increasing temperatures for both phases.

References

1. E.P. Wood, K.L. Nimmo, "In search of new lead-free electronic solders" *J. Elect. Mat.* Vol. 23 No. 8 (1994) 709–713
2. Y. Sun et al. "Nanoindentation for measuring individual phase mechanical properties of lead free solder alloy" *J. Mat. Sci: Mater Electron* 19: (2008) 514–521
3. K.N. Tu, A.M. Gusak, M. Li, "Physics and materials challenges for lead-free solders" *J. Appl. Phys.* Vol. 93 No. 3, (2003) 1335-1353
4. M. Abtew, G. Selvaduray, "Lead-free solders in microelectronics" *Mater. Sci. Eng.* Vo. 27 No. 5 (2000) 95-141
5. D. Q. Yu, J. Zhao, L. Wang, "Improvement on the microstructure stability, mechanical and wetting properties of Sn-Ag-Cu lead-free solder with the addition of rare earth elements" *J. alloys and compounds* Vol. 376 No. 1-2 (2004) 170-175
6. M. A. Rist, W. J. Plumbridge, S. Cooper, "Creep-constitutive behavior of Sn-3.8Ag-0.7Cu solder using an internal stress approach" *J. Elect. Mat.* Vol. 35, No. 5 (2006) 1050-1058
7. I. E. Anderson et al. "Alloying effects in near-eutectic Sn-Ag-Cu solder alloys for improved microstructural stability" *J. Elect. Mat.* Vol. 30 No. 9, 2001, 1050-1059
8. Anon, "Rare-Earth solders Make Better Bounds", *Photonics Spectra*, Vol. 36, No. 5 (2002), 139
9. M. Pei and J. Qu, "Effect of Lanthanum Doping on the Microstructure of Tin-Silver Solder Alloys" *J. Elect. Mat.* Vol. 37 No. 3 (2008) 331-338

10. X. Ma, Y. Qian, F. Yoshida, "Effect of La on the Cu-Sn intermetallic compound (IMC) growth and solder joint reliability" *J. alloys and compounds,* Vol. 334 No. 1-2 (2002), 224-227

11. C. M. L. Wu, Y. W. Wong, "Rare-earth additions to lead-free electronic solders" *J. Mater Sci. Mater Electron* Vol. 18 No. 1-3 (2007) 77–91

12. X. Deng, et al., "Deformation behavior of (Cu, Ag)-Sn intermetallics by nanoindentation" *Acta Mater.* Vol. 52 No. 14, (2004) 4291-4303

13. H. Rhee, J.P. Lucas, K.N. Subramanian, "Micromechanical characterization of thermomechanically fatigued lead-free solder joints" *J. Mater. Sci. Mater. Electron.* Vol. 13 No. 8 (2002), 477-484

14. W.C. Oliver, G.M. Pharr, "An improved technique for determining hardness and elastic modulus using load and displacement sensing indentation experiments" *J. Mater. Res.* Vol. 7 No. 6 (1992) 1564–1583

15. Gao F., Takemoto T., "Mechanical properties evolution of Sn-3.5Ag based lead-free solders by nanoindentation" , *Materials Letters* Vol. 60 No. 19 (2006) 2315–2318

16. *Y.T. Cheng, C.M. Cheng,* "Scaling, dimensional analysis, and indentation measurements" *Mater. Sci. Eng. R Rep.* 44 (2004) 91-149

17. R. R. Chromik, R. P. Vinci, S. L. Allen and M. R. Notis "Nanoindentation measurements on Cu–Sn and Ag–Sn intermetallics formed in Pb-free solder joints" *Journal of Materials Research* 18 (2003), 2251-2261

Synchronization of semiconductor lasers with complex dynamics within a multi-nodal network

Michail Bourmpos, Apostolos Argyris and Dimitris Syvridis

National and Kapodistrian University of Athens, Panepistimiopolis, Ilisia, 15784, Greece
E-mail: mmpour@di.uoa.gr , argiris@di.uoa.gr , dsyvridi@di.uoa.gr

Abstract: Semiconductor lasers are non-linear devices that exhibit stable, periodic, complex or chaotic dynamics, and in coupled configurations - under strict conditions - can be efficiently synchronized. Applications in communications using such devices for increased security usually employ a twofold system, the emitter and the receiver. In this investigation we examine the potential of this synchronization property to extend to communication networks with as many as 50 or 100 users (nodes) that are coupled to each other through a central node, in a star network topology.
Keywords: Chaos synchronization, mutual coupling, network synchronization, semiconductor lasers.

1. Introduction

Over the past decades a lot of effort has been put into exploiting chaotic dynamics of signals in areas like communications [1-3], control systems [4], artificial intelligence [5] and more. Chaotic signals emitted from semiconductor lasers (SLs) have been frequently used in security applications for data encryption [6], random number generation [7] etc. A usual configuration that the above types of applications employ consists of two elements - the emitter and the receiver - whose outputs are efficiently synchronized. More complex configurations have been adopted in recent works, where the idea of building a network of coupled SLs emitting synchronized chaotic signals has been proposed [8]. More specifically, Fischer et al [9] have demonstrated isochronal synchronization between two SLs relayed through a third SL, even in cases of large coupling time delays. Zamora-Munt et al [10] have shown operation in synchrony of 50 to 100 distant lasers, coupled through a central SL in a star network topology. In the above work, couplings between distant lasers and the central one are symmetric and the time delays (distances) from the central to the star lasers are assumed equal. The optical injection effect is based on moderate coupling strengths while little attention has been paid on the complexity and the spectral distribution of the signals.
In our work we use a large population -50 to 100- distant lasers which proves to be a sufficient number for good synchrony of the optical signals emitted, as discussed in [10]. Strong optical injection and asymmetric mutual couplings are adopted, enabling the increase on the effect that lasers have to each other through mutual coupling, while preserving the level of output optical power in

Received: 12 June 2012 / Accepted: 17 October 2012

ISSN 2241-0503

logic values (up to a few mW). Although intrinsic laser characteristics are selected to be identical in our simulations, different laser operational frequencies were assumed in terms of detuning values from a reference frequency ω_0.

2. Network Architecture and Rate Equations

We first consider a star network topology with N=50 semiconductor lasers, which from now on we will refer to as 'star lasers', relayed through a central similar semiconductor laser, called 'hub laser'.

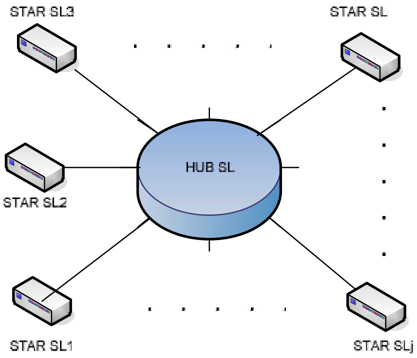

Figure 1. Star network architecture of N 'star' lasers, relayed through mutual couplings with a central 'hub' laser

A rate equation mathematical model is used to describe the operation and dynamics of the above system of devices. This model is based on the Lang Kobayashi rate equation model [11], originating from the representation used in [9] and including frequency detuning terms as in [10]. The complex optical fields and carrier numbers for the star and hub lasers can be calculated from:

$$\frac{dE_j(t)}{dt} = i\Delta\omega_j E_j(t) + \frac{1}{2}(1+ia)\left(G_j(t) - \frac{1}{t_{ph}}\right)E_j(t) + k_H E_H(t-\tau_H) + \sqrt{D}\xi_j(t)$$

$$\frac{dN_j(t)}{dt} = \frac{I_j}{e} - \frac{N_j(t)}{t_s} - G_j(t)\left|E_j(t)\right|^2$$

$$\frac{dE_H(t)}{dt} = i\Delta\omega_H E_H(t) + \frac{1}{2}(1+ia)\left(G_H(t) - \frac{1}{t_{ph}}\right)E_H(t) + \beta \cdot \sum_{j=1}^{N} k_j E_j + \sqrt{D}\xi_H(t)$$

$$\frac{dN_H(t)}{dt} = \frac{I_H}{e} - \frac{N_H(t)}{t_s} - G_H(t)\left|E_H(t)\right|^2$$

$$G_{j,H}(t) = \frac{g_n\left(N_{j,H}(t) - N_0\right)}{1 + s\left|E_{j,H}(t)\right|^2}$$

All laser have identical intrinsic parameters, with values as follows:

TABLE 1
INTRINSIC LASER PARAMETERS

α	linewidth enhancement factor	5
t_{ph}	photon lifetime	2*psec*
ω_0	reference laser frequency	$2\cdot\pi\cdot\lambda_0$
λ_0	reference laser wavelength	1550*nm*
D	noise strength	10^{-5} *nsec*$^{-1}$
e	electronic charge	$1.602\cdot10^{-19}$ C
t_s	carrier lifetime	1.54*nsec*
g_n	gain coefficient	$1.2\cdot10^{-5}$ *nsec*$^{-1}$
N_0	carrier density at transparency	$1.25\cdot10^{8}$
s	gain saturation coefficient	$5\cdot10^{-7}$

$\xi_j(t)$ and $\xi_H(t)$ are uncorrelated complex Gaussian white noises for the star and hub lasers respectively. The star lasers are biased at I_j=25mA, while the hub laser is biased at I_H=9mA, well below the solitary lasing threshold (I_{th}=17.4mA). Each laser is detuned with respect to the reference laser frequency ω_0, at variable values $\Delta\omega_j$ (star lasers) and $\Delta\omega_H$ (hub laser). Especially for the hub laser detuning, we can assume $\Delta\omega_H$ =0 without loss of generality. Delay times (τ_j=τ_H=5ns) and coupling strengths k_j=k_H=k are identical. Coupling asymmetry is achieved through the asymmetry coupling coefficient β. While each star laser receives a single injection field from the hub (k_H), the hub laser receives the sum of injection fields (k_j) of the N star lasers, which could be rather large. To counteract for this large value, β receives values smaller than 1, decreasing the overall injected optical field into the hub, keeping it within a realistic range of values.

3. Simulations and Numerical Results

Simulations were performed for the set of rate equations presented, using the 4th order Runge-Kutta method, with a time-step of 0.8psec. Optical power is deducted from the complex optical field using the appropriate conversion [12]. First we have evaluated the behavior of N=50 star lasers with detuning values ±1GHz around the reference frequency, following a Gaussian distribution, for different values of coupling strength and coupling asymmetry coefficient. Star lasers are ordered based on their detuning, so the 1st laser has the most negative detuning, while the 50th has the largest positive one. Based on these simulations, a mapping of mean and minimum zero-lag cross-correlation between the 50 star lasers was built. As we can see in figure 2, two different yellow-white areas of high correlation exist, one for low and one for high values of the product of coupling strength and coupling asymmetry coefficient ($k\cdot\beta$).

Moving along the diagonal from lower left to upper right corner of figure 2(i) - that is from lower to higher values of the product $k\cdot\beta$ - we encounter the following areas: first a small area in black, where correlation is low, the star lasers operate in CW mode with noise and the hub is not receiving enough coupling in order to emit in lasing mode.

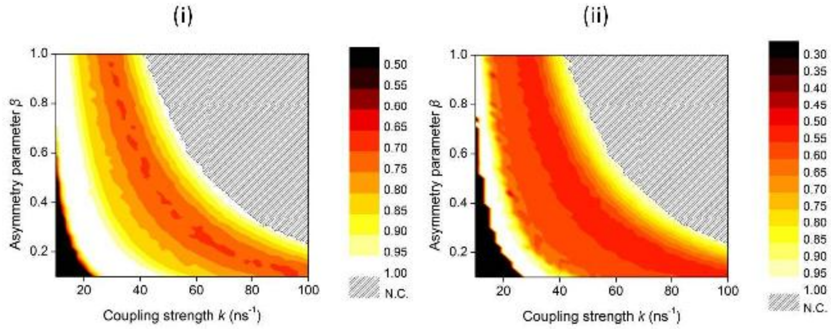

Figure 2. Mean (i) and minimum (ii) zero-lag correlation for 50 lasers with ±1GHz detuning values

Then we come across a white area, where $k \cdot \beta$ product has small values; the star lasers are characterized with periodic dynamics and the hub laser emits just above threshold. A further increase of $k \cdot \beta$ leads to star laser emission with chaotic dynamics (yellow-orange area). The hub laser now emits in the order of few hundreds µW but the mean correlation experiences significant decrease. As the product $k \cdot \beta$ increases optical injection becomes large enough to drive the star lasers into emitting signals of high correlation (small yellow-white stripe). The complexity of these signals slightly decreases and the hub laser now emits in the order of several mW. Finally the hatched area is an uncharted region where optical injection and emitted optical powers are unrealistically large and the rate equation model does not converge.

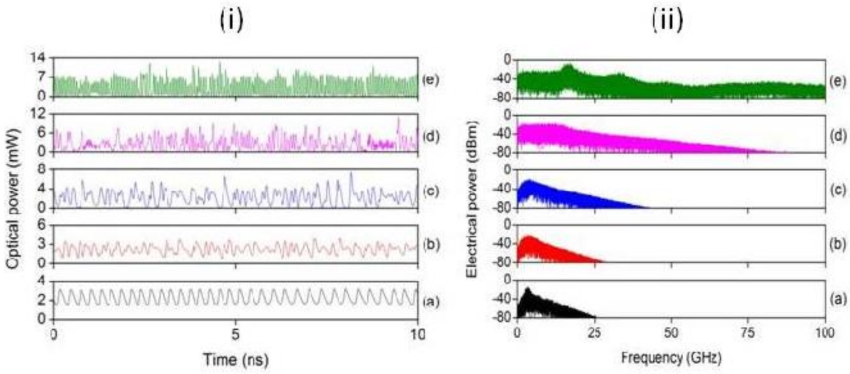

Figure 3 Time traces (i) and spectra (ii) of a single laser for network of 50 lasers with ±1GHz detuning values, coupling strengths $k_j = k_H = 60\text{nsec}^{-1}$ and coupling asymmetry coefficients (a) β=0.15, (b) β=0.2, (c) β=0.4, (d) β=0.8 and (e) β=1.

Time traces and spectra of the different cases we have just described are shown in figure 3(ii), for a fixed coupling strength value of k=60nsec^{-1}. It is evident that for larger values of the product $k\cdot\beta$ we have faster oscillations attributed to bandwidth enhancement, as has been commonly reported in cases of strong optical injection [13-14].

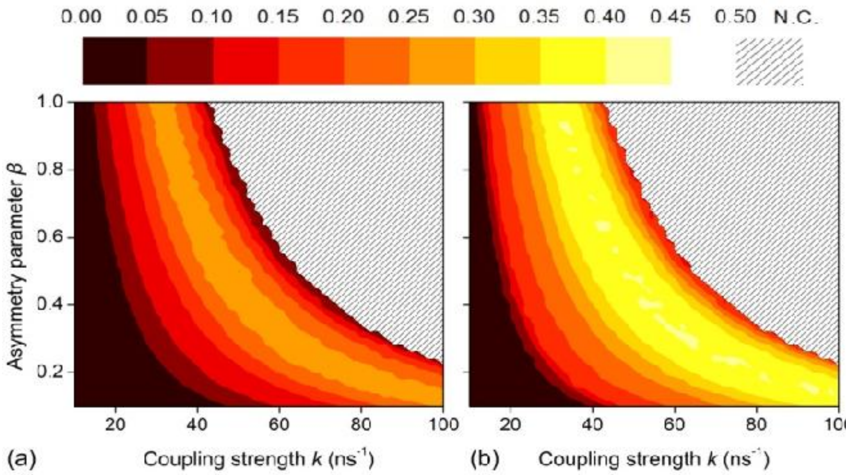

Figure 4. Mean (a) and maximum (b) synchronization error for 50 lasers with ±1GHz detuning values

Another useful parameter we have estimated to evaluate the star lasers output waveforms is the zero-lag synchronization error. Synchronization error is normalized in the mean value of the *i*th and *j*th laser, averaged in the duration T_{av} and is thus expressed in the form:

$$\varepsilon_{ij} = \left\langle \frac{\left|P_i(t) - P_j(t)\right|}{0.5 \cdot \left(P_i(t) + P_j(t)\right)} \right\rangle \tag{6}$$

As expected, small values of synchronization error between the ith and jth laser are achieved in the same areas where good zero-lag cross-correlation exists (figure 4 vs figure 2). Based on figure 4 we can identify (k,β) pairs where the maximum synchronization error, which indicates the worst behavior in our network, is minimal. One such pair is k=60nsec^{-1}, β=0.5. For this case of parameters we depict the zero-lag correlation between the ith and jth laser (figure 5i). The worst case of synchronization - in which we encounter the minimum correlation - occurs for the pair of lasers with the far most frequency detuning, that is between lasers 1 and 50. We can also observe that lasers with similar detuning values have good correlations with respect to each other, even when possessing large absolute detuning values.

The superimposed time traces of the 50 star lasers for the above pair of parameters are shown in figure 5(ii). We can observe highly synchronized signals at zero lag for the biggest part of the time window depicted.

However we can identify small periods of time where synchronization may be lost.

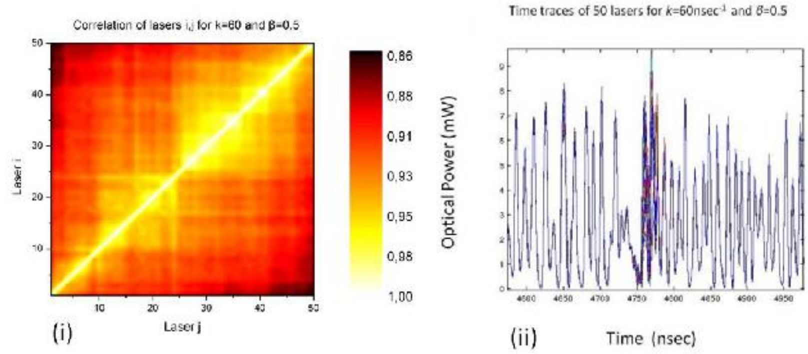

Figure 5. (i) Zero-lag correlation between 50 lasers with ±1GHz detuning values, coupling strengths k_j=k_H=60nsec^{-1} and coupling asymmetry coefficient β=0.5.
(ii) Time traces of 50 superimposed star laser outputs ±1GHz detuning values, for he parameter pair k=60nsec^{-1} , β=0.5

The star lasers rapidly synchronize again after a few ns. This phenomenon is repeated in the complete time series and is mainly responsible for the synchronization error calculated, since the synchronization error in the rest of the time window is almost zero.

By increasing the frequency detuning range of the star lasers from ±1GHz to ±10GHz, the system necessitates much larger values of the product $k \cdot \beta$ in order to force the hub laser into lasing emission (figure 6i). As a result, the first area examined, where the star lasers emit in CW mode, is enlarged. The area of non-convergence remains almost the same, while areas of complex dynamics and large cross-correlation values are minimized.

To counteract the increase in the detuning values we attempt to increase the number of star lasers in the network from N=50 to N=100. It is apparent in figure 6ii that inserting more lasers in the network leads to more optical power injected in the hub laser, which now emits for smaller values of the product $k \cdot \beta$. However, small increase in the areas of good cross-correlation is observed.

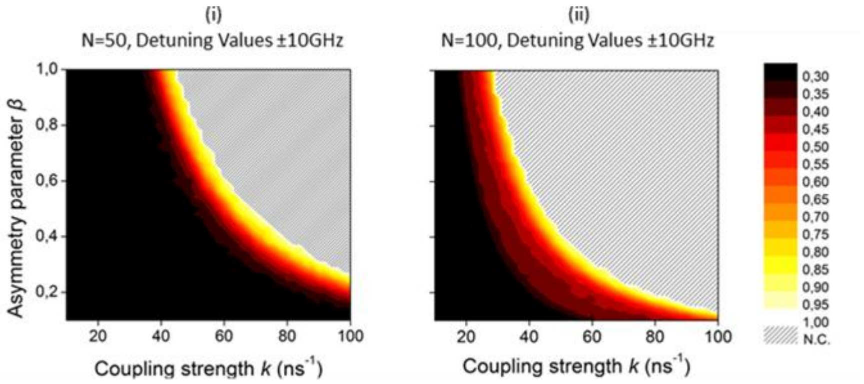

Figure 6. Mean zero-lag correlation for (i) N=50 and (ii) N=100 lasers with ±10GHz detuning values

Another attempt to counteract the increase in detuning values is to lower the pump current of the star lasers to I=18mA near the lasing threshold. This reduces the effect the star lasers dynamics have in the network. In figure 7 we can observe significant increase of the areas of good cross-correlation.

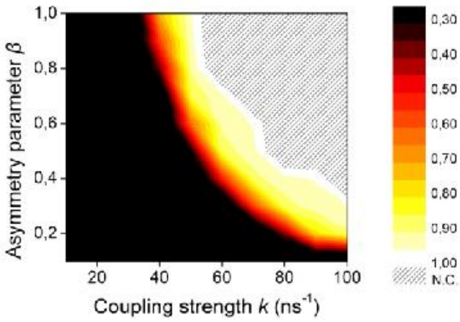

Figure 7. Mean zero-lag correlation for N=50 and pump current I=18mA for the star lasers

Finally, a small analysis was carried out on the type of synchronization occurring in the network and the role the hub laser plays on it. Figure 8 clearly shows that the hub lasers dynamics lag behind the dynamics of the star lasers by exactly the time delay between star and hub lasers, that is $\tau_j = \tau_H$=5ns. As a deduction we can say that the hub laser holds a passive role in the network, operating solely as a relay between the star lasers. The internal parameters of the star lasers, the time delay, coupling strength, asymmetry and driving current seem to be solely responsible for the dynamics of the system.

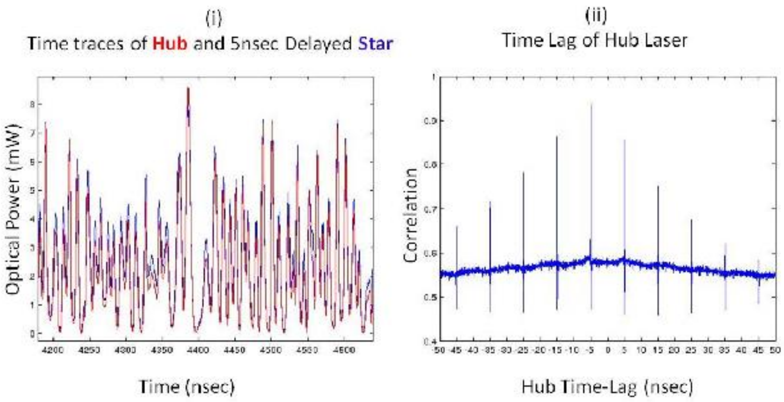

Figure 8. (i) Time traces of hub(red) and one random star (blue) delayed by

5nsec lasers, (ii) Cross-correlation time lag of hub and one random star laser

4. Conclusions

A star network topology with multiple nodes consisting of typical semiconductor lasers has been presented and investigated. Two general areas of good synchronization have been identified, each one with different characteristics in terms of dynamics. The first one, for small values of total optical injection ($k{\cdot}\beta$ product), produces optical signals of simpler dynamics, while the second one, for large values of $k{\cdot}\beta$, produces signals with high complexity dynamics. An increase in the number of nodes in the network has proved to enlarge these areas and provide synchronization improvement.

References

[1] L.M. Pecora and T.L. Caroll, "Synchronization in chaotic systems," *Phys. Rev. Lett.*, vol. 64, 821-824, 1990.

[2] P. Colet and R. Roy, "Digital communication with synchronized chaotic lasers," *Opt. Lett.*, vol. 19, pp. 2056–2058, 1994.

[3] A. Argyris, D. Syvridis , L. Larger, V. Annovazzi-Lodi, P. Colet, I. Fischer, J. García-Ojalvo, C.R. Mirasso, L. Pesquera and K.A. Shore, "Chaos-based communications at high bit rates using commercial fiber-optic links," *Nature*, vol. 438, n. 7066, pp. 343-346, 2005.

[4] A.L. Fradkov, R.J. Evans and B.R. Andrievsky, "Control of chaos: methods and applications in mechanics," *Phil. Trans. R. Soc. A*, vol. 364, 2279-2307, 2006.

[5] C. R. Mirasso, P. Colet, and P. Garcia-Fernandez, "Synchronization of chaotic semiconductor lasers: Application to encoded communications," *IEEE Photon. Technol. Lett.*, vol. 8, pp. 299–301, 1996.

[6] V. Annovazzi-Lodi, S. Donati, and A. Scire, "Synchronization of chaotic injected laser systems and its application to optical cryptography," *IEEE J. Quantum Electron.*, vol. 32, pp. 953–959, 1996.

[7] A. Uchida, K. Amano, M. Inoue, K. Hirano, S. Naito, H. Someya, I. Oowada, T. Kurashige, M. Shiki, S. Yoshimori, K. Yoshimura, and P. Davis, "Fast physical random bit generation with chaotic semiconductor lasers", Nature Photon. 2, 728–732 (2008).

[8] R. Vicente, I. Fischer, and C. R. Mirasso, "Synchronization properties of three-coupled semiconductor lasers," *Phys. Rev. E*, vol. 78, 066202, 2008.

[9] I. Fischer, R. Vicente, J.M. Buldú, M. Peil, C.R. Mirasso, M.C. Torrent and J. García-Ojalvo, "Zero-Lag Long-Range Synchronization via Dynamical Relaying," *Phys. Rev. Lett.*, vol. 97, 123902, 2006.

[10] J. Zamora-Munt, C. Masoller, J. Garcia-Ojalvo and R. Roy "Crowd synchrony and quorum sensing in delay-coupled lasers," *Phys. Rev. Lett.*, vol. 105, 264101, 2010.

[11] R. Lang and K. Kobayashi, "External optical feedback effects on semiconductor injection laser properties," *IEEE J. Quantum Electron.*, vol. 16, pp. 347-355, 1980.

[12] K. Petermann, *Laser Diode Modulation And Noise*, New Ed. Kluwer Academic Publishers Group (Netherlands), 1991.

[13] T.B. Simpson and J.M. Liu and A. Gavrielides, "Bandwidth enhancement and broadband noise reduction in injection-locked semiconductor lasers," *IEEE Photon. Technol. Lett.*, vol. 7, pp. 709-711, 1995.

[14] A. Murakami, K. Kawashima and K. Atsuki, "Cavity resonance shift and bandwidth enhancement in semiconductor lasers with strong light injection," *IEEE Quantum Electron.*, vol.39, pp. 1196-1204, 2003.